PHYSICAL REVIEW E **95**, 013304 (2017)

Prediction of the moments in advection-diffusion lattice Boltzmann method. I. Truncation dispersion, skewness, and kurtosis

Irina Ginzburg[*]

Irstea, Antony Regional Centre, HBAN, 1 rue Pierre-Gilles de Gennes CS 10030, 92761 Antony Cedex, France

(Received 1 April 2016; revised manuscript received 9 September 2016; published 17 January 2017)

The effect of the heterogeneity in the soil structure or the nonuniformity of the velocity field on the modeled resident time distribution (RTD) and breakthrough curves is quantified by their moments. While the first moment provides the effective velocity, the second moment is related to the longitudinal dispersion coefficient (k_T) in the developed Taylor regime; the third and fourth moments are characterized by their normalized values skewness (Sk) and kurtosis (Ku), respectively. The purpose of this investigation is to examine the role of the truncation corrections of the numerical scheme in k_T, Sk, and Ku because of their interference with the second moment, in the form of the numerical dispersion, and in the higher-order moments, by their definition. Our symbolic procedure is based on the recently proposed extended method of moments (EMM). Originally, the EMM restores any-order physical moments of the RTD or averaged distributions assuming that the solute concentration obeys the advection-diffusion equation in multidimensional steady-state velocity field, in streamwise-periodic heterogeneous structure. In our work, the EMM is generalized to the fourth-order-accurate apparent mass-conservation equation in two- and three-dimensional duct flows. The method looks for the solution of the transport equation as the product of a long harmonic wave and a spatially periodic oscillating component; the moments of the given numerical scheme are derived from a chain of the steady-state fourth-order equations at a single cell. This mathematical technique is exemplified for the truncation terms of the two-relaxation-time lattice Boltzmann scheme, using plug and parabolic flow in straight channel and cylindrical capillary with the d2Q9 and d3Q15 discrete velocity sets as simple but illustrative examples. The derived symbolic dependencies can be readily extended for advection by another, Newtonian or non-Newtonian, flow profile in any-shape open-tabular conduits. It is established that the truncation errors in the three transport coefficients k_T, Sk, and Ku decay with the second-order accuracy. While the physical values of the three transport coefficients are set by Péclet number, their truncation corrections additionally depend on the two adjustable relaxation rates and the two adjustable equilibrium weight families which independently determine the convective and diffusion discretization stencils. We identify flow- and dimension-independent optimal strategies for adjustable parameters and confront them to stability requirements. Through specific choices of two relaxation rates and weights, we expect our results be directly applicable to forward-time central differences and leap-frog central-convective Du Fort–Frankel–diffusion schemes. In straight channel, a quasi-exact validation of the truncation predictions through the numerical moments becomes possible thanks to the specular-forward no-flux boundary rule. In the staircase description of a cylindrical capillary, we account for the spurious boundary-layer diffusion and dispersion because of the tangential constraint of the bounce-back no-flux boundary rule.

DOI: 10.1103/PhysRevE.95.013304

I. INTRODUCTION

Description of the physical phenomena in laboratory or field experiments may necessitate fine characterization of a data set, going beyond its mean and variance. The examples cover a very broad spectrum of problems. In our concern they are the statistical measures of soil bimodality [1] and the related "abnormal" propagators curves for molecular displacement [2,3]. Their second-order central moment ($\mu_2^\star$) determines the Taylor-Aris [4,5] longitudinal dispersion, through correction $k_T D_0$ to molecular diffusion coefficient D_0 in duct flows: $D_0(1+k_T)=\frac{\mu_2^\star}{2t}$. The deviation from the normal distribution is characterized [6] by the third- ($\mu_3^\star$) and fourth-order ($\mu_4^\star$) central moments, typically through skewness $\mathrm{Sk}=\frac{\mu_3^\star}{(\mu_2^\star)^{3/2}}$ and (excess) kurtosis $\mathrm{Ku}=\frac{\mu_4^\star}{(\mu_2^\star)^2}-3$. Whereas the skewness measures the degree of the asymmetry [its negative (positive) values indicate that data are left (right) skewed relative the normal profile], the positive (negative) kurtosis indicates how their relative peakiness (flatness) at the center is balanced by long (short) tails at periphery. In fact, while the Gaussian distribution presents the asymptotic solution for long enough time, the mean concentration or residential time distribution (RTD) [7] may deviate from it for short time and in finite-length systems where the high-order effects gain in relevance. The nuclear magnetic resonance (NMR) may allow the measurements of skewness [2,3,8] but estimate of the kurtosis remains difficult due to the experimental error [8]. At the same time, although analytical [9–12] and numerical approaches [13,14] are intensively used to quantify the Taylor-Aris dispersivity, the higher-order non-Gaussian moments are hardly addressed.

The recently developed *extended method of moments* (EMM) [15] consists of the mathematical algorithm which allows to quantify any-order moment in given periodic velocity field and soil structure, for entire Péclet range (Pe), by sequentially solving linear steady-state advection-diffusion equations with specific sources inside a single cell. At the second order, the EMM is equivalent to Brenner's method [9] for effective dispersion in spatially periodic velocity field; this methodology has been implemented numerically [13] and

---

[*] irina.ginzburg@irstea.fr

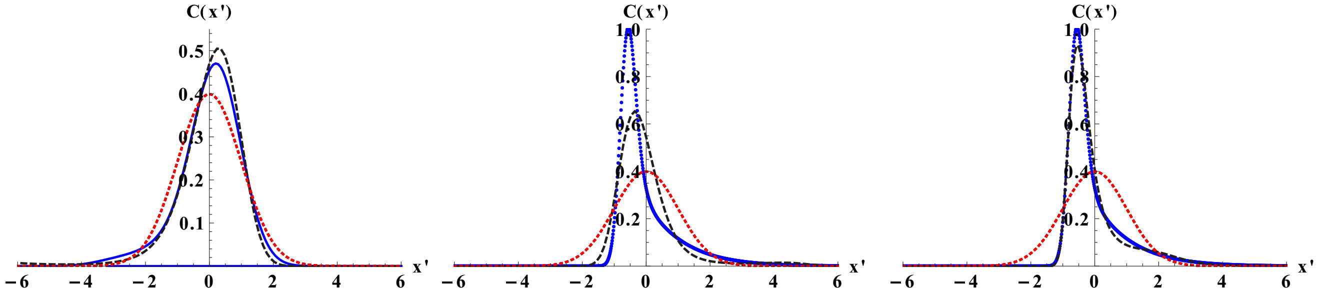

FIG. 1. The first diagram illustrates the three centered average concentration profiles in bimodal channel (composed of open layer and porous layer of porosity $\phi = 10^{-1}$) produced by (i) the averaged ADE (red, dotted line), (ii) the d2Q5 TRT scheme (blue, solid line), and (iii) the reconstruction from the predicted by the EMM values (black, dashed line): $k_T = 0.94$, $\mathrm{Sk}_\star = -0.84\sqrt{\mathrm{Pe}}$, and $\mathrm{Ku}_\star = 1.49\mathrm{Pe}$ for Pe = 13.6. The second diagram displays similar comparison for the Darcy flow in stratified periodic soil of porosity contrast 50 where $k_T = 19.57$, $\mathrm{Sk}_\star = 2.37\sqrt{\mathrm{Pe}}$, and $\mathrm{Ku}_\star = 7.82\mathrm{Pe}$ for Pe = 9.07. In the last diagram, the reconstruction procedure involves the four next moments and achieves the entire agreement between the TRT and EMM. These figures are borrowed [15]: Figs. 24(b), 14(a), and 15(a) there, respectively.

successfully applied in a series of synthetic porous structures. The work [15] shows that the two sets of moments, namely, spatial moments of average concentration evolving in time or temporal moments of resident time distribution [7] varying in space, are linked through simple recursive formulas, meaning that one can be obtained from another. The EMM assumes the fully developed Taylor regime, when k_T becomes time independent, while Sk and Ku decay either as $\mathrm{Sk}_\star t^{-1/2}$ and $\mathrm{Ku}_\star t^{-1}$ in time, or as $\mathrm{Sk}_\star x^{-1/2}$ and $\mathrm{Ku}_\star x^{-1}$ streamwise from the inlet, respectively. The corresponding distribution can be reconstructed from the predicted moments using the entropy-maximization procedure [16]. The velocity field may have the microscopic, mesoscopic, or macroscopic nature: the EMM is symbolically exemplified for dispersion in shallow channels of different cross section, power-law non-Newtonian fluid, Darcy and parabolic flows in double-porosity stratified soil and cylindrical capillary. The two principal advantages of the EMM over direct transient multidimensional solvers of the advection-diffusion equation (ADE) is that it reduces the problem of the effective moments to steady state and a single (streamwise-periodic) cell.

This work concerns with the direct simulations of the solute transport by the lattice Boltzmann method (LBM-ADE). Pioneered in early works [17–19], it has been applied in fractures and conduits [20–22], and more recently, in reconstructed rock samples [23–27]. The LBM-ADE is appealing for its intrinsic exact mass conservation supported by the Maxwell reflections at solid walls, and for its uniform update through the soil interfaces matching the physical continuity conditions implicitly (finer interface analysis or explicit interface conditions can be found in works [15,28–33]). The LBM is also favored for its advanced computational efficiency; however, the direct serial solution of the ADE remains a time-consuming task even for the most efficient numerical techniques. Specific adaptation for the explicit tracking of the tracer displacement [23] or Brownian motion of particles [27] adds further complication. However, the results are promising. From the numerical perspective, the experimental data for molecular propagator distributions in different porous structures ranging from homogeneous bead pack to bimodal Portland Carbonate [3] are matched by the LBM numerical solutions [23]. On the theoretical plan, the two approaches, the EMM and LBM-ADE, were validated one against the other by using the two-relaxation-times (TRT) scheme [15] which extends uniform soil TRT schemes [34,35] to heterogeneous soil. Figure 1 illustrates the two synthetic examples where the soil bimodality creates the well-pronounced "asymmetric" effects. The profiles reconstructed from the first four EMM moments and the direct TRT simulations mainly agree and predict deviations from the Gaussian distribution (two first diagrams); a better agreement is achieved by reconstructing with a higher number of the EMM moments (last diagram). These results confirm that the LBM-ADE is indeed able to capture the principal non-Gaussian effects.

This work aims to analyze the interference of the high-order moments with the truncation corrections in the LBM-ADE. The idea is to generalize the EMM from the second-order ADE to the fourth-order-accurate apparent transport equation of the numerical scheme. The EMM looks for the solution of the transport equation as the product of a long harmonic wave and a spatially periodic oscillating part. Its period is set by the periodicity of the porous cell, and it is much shorter than the length of the wave. Substitution of this ansatz into the transport equation and the expansion into Taylor series with respect to the (small) wavelength γ yields a chain of fourth-order steady-state transport equations at a single cell, with respect to the so-called "extended B-field" variable. The source term of the B-field equation depends on the nonuniformity of the velocity field; the solvability condition allows for determination of the temporal (RTD) moments. In duct flow, the EMM approach will reduce the problem to the fourth-order diffusion equation with sources, allowing for symbolic solutions for B-field variable and the temporal moments. Further, the aforementioned recursive formulas [15] connect the temporal and spatial moments of the averaged concentration. With their help, we will derive the apparent solutions for k_T, Sk, and Ku, and specify their dependency over all relevant adjustable parameters of the TRT scheme. The developed approach applies for any other numerical method providing its truncation corrections are known.

The truncation corrections have been partly derived in some of LBM-ADE schemes, as the multiple-relaxation times (MRT) models [34,36,37] or single-relaxation-times [38] Bhatnager-Gross-Krook (BGK) schemes [39,40]. Due to symmetry argument, the TRT scheme allows to develop truncation analysis in an elegant form [35,41], independent of the discrete-velocity set and equilibrium distribution. The truncation analysis [35,41] does not involve either the Chapman-Enskog, Fourier, or asymptotic analysis, rather it is based on the exact mass-conservation equation of the scheme, which is expressed in the form of the central discrete operators, directional in space. They are applied to any equilibrium and nonequilibrium components, interconnected via the exact recurrence equations [42] of the TRT scheme. In these equations, the discrete operators are developed into Taylor series sequentially providing solution for the nonequilibrium component. The second- and higher-order time derivatives are all replaced by spatial ones, recovered through the lower-order approximations. In this way, the truncation coefficients are established without specifying the equilibrium function and discrete-velocity set: they uniquely depend on the two relaxation eigenfunctions: Λ^- for antisymmetric (diffusion) mode and Λ^+ for symmetric (free) mode. So far, the third- and fourth-order-accurate TRT truncation corrections have been expressed in a generic form, suitable for isotropic and anisotropic equilibrium functions from one to three dimensions, either in homogeneous [35,41] or heterogeneous [15] soil. Further, the equilibrium distribution predicates the differential form of the fourth-order equation; the isotropy of its third-order (convective) term is related to the equilibrium velocity weight, while the isotropy of its fourth-order (diffusion) term is related to the equilibrium mass weight [35]. The two weight families can be selected independently: they play similar roles with the finite-difference, convective and diffusion, discretization stencils. Additionally, the equilibrium introduces diffusion-coefficient scale parameter, say c_e: $D_0 = c_e\Lambda^-$, where $\Lambda^- > 0$ and c_e is freely adjustable inside its mass-weight-dependent stability interval [35,43,44]. In transition, the truncation coefficients depend on the c_e and Λ^- separately.

At steady state, the truncation coefficients become polynomials of the product of two eigenfunctions; this control parameter is denoted $\Lambda = \Lambda^+\Lambda^-$. The two particular choices [34,35,41] $\Lambda = \frac{1}{12}$ and $\frac{1}{6}$ vanish, respectively, the third- and fourth-order spatial truncation components for any equilibrium. A special attention will be also put on $\Lambda = \frac{1}{4}$, the so-called OTRT (optimal TRT) subclass where the necessary stability bounds become (i) independent of Λ^- and Λ^+ and (ii) sufficient, either with the minimal models or with the specific full equilibrium weights [43,44]. The OTRT subclass also enables the direct finite-difference interpretation of exact mass-conservation equation of the TRT scheme and its stability conditions [35,43]. The optimal stability of the minimal schemes is well understood and confirmed numerically, e.g., in d2Q5 with the Poiseuille profile [41]. The most interesting combinations of the adjustable parameters, such as those which liberate the transport coefficient either from Λ or weight dependency, or those which eliminate numerical errors, will be explored in this work. Note that in the physical model [15], the k_T, Sk, and Ku are set by Pe and the geometry alone. We will examine the Pe dependency in the apparent coefficients and establish their asymptotic behavior with Pe and mesh resolution.

The d3Q7 OTRT scheme was recently applied in investigation [12] for three subsequent time-scale regimes (diffusion, advection, and dispersion) in shear thinning flow prescribed in the cylindrical capillary. The numerical and analytical (derived there) expressions for Taylor-dispersion coefficients in Herschel-Bulkley fluid were found in very good accordance in large Pe range, Pe $\in [50,800]$.

In fact, the second-order (Λ-independent) numerical diffusion of the scheme, which is presented for linear-velocity equilibrium even in plug flow, has been identified for a long time and different equilibrium and relaxation techniques were proposed for its elimination (see [41,45,46]). However, the Taylor-type longitudinal *numerical* dispersivity coefficient $\delta k_T^{(\mathrm{tr})}$, due to the transverse velocity gradient, was quantified only recently [41]. It sums with the physical Taylor value k_T in variance of the numerical distributions. The closed-form expression was derived [41] for $\delta k_T^{(\mathrm{tr})}$ with the help of the Taylor argument [4], by extending it to the third- and fourth-order truncation corrections. This result was specified [41] with the d2Q5 and d2Q9 TRT schemes for Poiseuille advection profile: it is quasi-exact once the discretization effect in the computation of two first moments is accounted for. It was shown that $\delta k_T^{(\mathrm{tr})}$ decays as the second-order correction to k_T. Within small Pe range, the $\delta k_T^{(\mathrm{tr})}$ noticeably depends on c_e and Λ^-. Since $\delta k_T^{(\mathrm{tr})}$ scales as Pe^2, its relative contribution to k_T is asymptotically constant and is set by equilibrium velocity weight and Λ, and it can be eliminated or reduced for a proper relation between them. The numerical dispersivity of the d3Q15 TRT scheme in cylindrical capillary will be first derived following the same methodology and compared with the channel solution [41]. In particular, the joined truncation and discretization estimate will produce numerical results [12] for dispersivity in Newtonian fluid very accurately. However, the "manual" exploration of the truncation corrections for skewness and kurtosis becomes complicated and the EMM approach will be called for help. The EMM-based approach will give the same result on the numerical longitudinal dispersion as the direct analysis of the truncation corrections following [41]. On the one hand, this agreement underlines the similarity between the Taylor analysis [4], Aris method of moments [5], and the EMM; on the other hand, it confirms the validity of the Taylor assumptions to higher-order equations.

The subtle point of the numerical validation lies in the accuracy of the boundary scheme used to enforce the zero-flux Neumann condition on the impermeable walls. While this issue is not expected to pose any difficulty in a straight channel thanks to specular-forward (nonlocal) mirror reflection [21,47,48], it is not the case in a cylindrical pipe, where we apply the bounce-back boundary rule (BB hereafter). Although the curved boundary is only staircase approximated with the bounce-back rule, because of the leading-order midgrid location of the solid surface [47,49], our main concern is about its restriction on the tangential flux at the solid wall [47]. It was only recently exactly quantified [50] in straight channel that this deficiency causes (i) a diminution of the imposed molecular diffusion coefficient D_0, in proportion to the *diagonal mass-weight value*, and (ii) a retardation of the imposed advective flux, in proportion to the *diagonal velocity-weight value*. The extension of the results [50] to the cylindrical capillary is performed in joined work [51]; the results [51] enable us to account for the boundary-layer diffusion and dispersion in the full weight space. Although it is found [51] that only the d3Q7 weight subclass of the d3Q15 is free from the spurious boundary effects in grid-aligned open-tubular conduits, we will need the hydrodynamic mass weight for the fourth-order isotropy in diffusion form, required by truncation analysis. We keep also in mind that the suitable diagonal velocity weights [43,44] have much larger stable velocity range than the coordinate stencil of the d3Q7 scheme.

The rest of the paper is organized as follows. Section II provides the principal elements of the EMM approach, specifies the TRT-ADE scheme, summarizes its stability, truncation results, and connections with the finite-difference schemes, then provides a qualitative description of the bounce-back effects. Section III develops the EMM approach for the fourth-order-accurate apparent transport equation of the TRT scheme in straight channel and produces the closed-form bulk estimate for k_T, Sk, and Ku in d2Q9 TRT scheme, for plug and parabolic flow. The numerical validation mostly applies the specular-forward reflection. Section IV performs a similar analysis for the d3Q15 scheme in the cylindrical capillary, where the numerical validation accounts for the spurious bounce-back effects of the bounce-back rule. The optimal parameter guidelines are discussed in Secs. III G and IV E for two- (2D) and three-dimensional (3D) results, respectively; the flow- and dimension-independent optimal strategies are then summarized in the concluding Sec. V. Appendix A presents the generic form [35,41] of the apparent fourth-order-accurate mass-conservation equation of the TRT scheme. Appendix B presents the detailed derivation of this result in the particular case of $\Lambda = \frac{1}{4}$, illustrating connections with the finite-difference schemes.

II. BACKGROUND

Section II A recalls and illustrates the working principles of the EMM, extended method of moments [15]; Sec. II B summarizes the TRT-ADE scheme [15,28,34,35], the two-relaxation-times numerical scheme for advection-diffusion equation, discusses its equilibrium and relaxation degrees of freedom, stability conditions, generic truncation form and connections with the finite-difference schemes; Sec. II C formulates the error estimate which will be applied for the apparent (truncation) moments of the TRT scheme and their numerical values with respect to the predicted physical moments; Sec. II D outlines how the possible boundary effects [50,51] will be accounted for. It should be said that although the truncation corrections are also known in heterogeneous TRT schemes [15], the EMM and the TRT algorithms are both restricted to the homogeneous transport of the solute in duct flow in this work because the effective location of the underlying interface continuity conditions may dominate over truncation accuracy [15,28,32]. In fact, while the strong non-Gaussian effects are only expected in highly heterogeneous systems, the k_T, Sk, and Ku differ from zero due to the nonuniformity of velocity field even in most basic systems, as the spatial spread of the Dirac plume by parabolic velocity profile. We use this illustrative example in a channel and in a cylindrical capillary, operated with the d2Q9 and d3Q15 schemes, respectively; the reference (physical) k_T solution [4,5] is well known, the Sk and Ku solutions are constructed by the EMM (we will restrict them from the bimodal system [15] to open flow, and transform the moments from the RTD to spatial dispersion).

A. Extended method of moments (EMM)

Consider modeling of the isotropic d-dimensional advection-diffusion equation in duct-type (open) flow, a particular case of the heterogeneous porous flow where the EMM is formulated [15]. The evolution of the solute concentration $C(\boldsymbol{r},t)$ in the prescribed steady-state velocity field $\boldsymbol{U}(\boldsymbol{r})$ is described by the second-order advection-diffusion equation (ADE)

$$\partial_t C + \nabla \cdot (\boldsymbol{U} C) = \nabla \cdot (D_0 \nabla C). \tag{1}$$

Assume $\boldsymbol{U}$ to be streamwise periodic over a single cell and the mean seepage velocity $\mathcal{U} = \langle \boldsymbol{U} \rangle$ be directed along the x axis, $\langle \ldots \rangle = S^{-1} \int_S ds$ denotes the average value over the open part in cross section $S(x)$. In the established Taylor-dispersion regime, the averaged concentration $\bar{C}(x,t) = \langle C \rangle$ is expected to propagate with velocity $\mathcal{U}$ and to diffuse with longitudinal dispersion coefficient D:

$$\partial_t \bar{C} + \partial_x \mathcal{U} \bar{C} = D \partial_x^2 \bar{C}, \quad D = D_0(1 + k_T). \tag{2}$$

The nondimensional dispersivity coefficient k_T determines the Taylor-dispersion correction [4] to molecular diffusion coefficient D_0; such a dispersion is induced by the transverse gradient in velocity field. Aris [5] demonstrates that D can be restored from the variance of the averaged distribution. Let $\mu_n(t) = \int_{-\infty}^{\infty} (x - x_0)^n \bar{C}(x,t) dx$ denote the nth raw moment of $\bar{C}$, while $\mu_n^\star(t)$ be its nth central moment: $\mu_n^\star(t) = \int_{-\infty}^{\infty} (x - x_0 - \mathcal{U} t)^n \bar{C}(x,t) dx$, for $n \geqslant 2$. Hereafter, we address the first four moments assuming the exact mass conservation with $\mu_0(t) \equiv 1$. The mean velocity $\mathcal{U}$, dispersion coefficient D, skewness Sk, and kurtosis Ku are set by the first four spatial moments:

$$\mathcal{U} = \frac{\mu_1}{t}, \quad D = \frac{\mu_2^\star}{2t}, \quad \mathrm{Sk}(t) = \frac{\mu_3^\star(t)}{\left[\mu_2^\star(t)\right]^{3/2}},$$
$$\mathrm{Ku}(t) = \frac{\mu_4^\star(t)}{[\mu_2^\star(t)]^2} - 3. \tag{3}$$

The EMM sequentially predicts the moments of the solute distributions obeying Eq. (1), without directly solving it. The method is based on the assumption that solution of Eq. (1) can be presented in a form of the product of the periodic oscillating part $\tilde{\mathcal{P}}(\omega,\gamma;\boldsymbol{r}/\epsilon)$ (in fast variables $\boldsymbol{r}/\epsilon$ with small parameter ϵ) with a slowly varying component:

$$C(\omega,\gamma;\boldsymbol{r},t) = \frac{1}{2\pi} \tilde{\mathcal{P}}(\omega,\gamma;\boldsymbol{r}/\epsilon) \exp[i(\gamma x - \omega t)]. \tag{4}$$

The small-valued wave number (spatial frequency) γ and the temporal frequency ω are unknowns to be found through their Taylor expansions:

$$\text{“}s\text{ expansion”}: \omega(\gamma) = -i \sum_{n=1}^{\infty} \omega^{(n)} (i\gamma)^n \quad \text{and}$$
$$\text{“}t\text{ expansion”}: \quad \gamma(\omega) = -i \sum_{n=1}^{\infty} \gamma^{(n)} (i\omega)^n. \tag{5}$$

By substituting one expansion into another, the coefficients of the two expansions (5) are inter-related [15]:

$$\omega^{(1)} = \frac{1}{\gamma^{(1)}}, \quad \omega^{(2)} = -\frac{\gamma^{(2)}}{{\gamma^{(1)}}^3}, \quad \omega^{(3)} = -\frac{-2{\gamma^{(2)}}^2 + \gamma^{(1)}\gamma^{(3)}}{{\gamma^{(1)}}^5},$$
$$\omega^{(4)} = -\frac{5{\gamma^{(2)}}^3 - 5\gamma^{(1)}\gamma^{(2)}\gamma^{(3)} + {\gamma^{(1)}}^2\gamma^{(4)}}{{\gamma^{(1)}}^7}, \ldots. \tag{6}$$

Therefore, if one set is found, the other one can be computed with Eq. (6). In order to relate $\{\gamma^{(n)}\}$ and $\{\omega^{(n)}\}$ with the moments, we note that, on the one hand, $\tilde{\mathcal{P}}(\omega(\gamma);\boldsymbol{r}/\epsilon)e^{-i\omega(\gamma)t}$ can be regarded as the space Fourier transform of the concentration for given γ:

$$\tilde{\mathcal{P}}(\omega(\gamma);\boldsymbol{r}/\epsilon)\exp\left[-i\omega(\gamma)t\right] = \int_{-\infty}^{\infty} C(\boldsymbol{r},t)\exp(-i\gamma x)dx. \tag{7}$$

On the other hand, $\tilde{\mathcal{P}}(\gamma(\omega);\boldsymbol{r}/\epsilon)e^{i\gamma(\omega)x}$ is the time Fourier transform of the concentration:

$$\tilde{\mathcal{P}}(\gamma(\omega);\boldsymbol{r}/\epsilon)\exp\left[i\gamma(\omega)x\right] = \int_{-\infty}^{\infty} C(\boldsymbol{r},t)\exp(i\omega t)dt. \tag{8}$$

It follows that whereas the set $\{\omega^{(n)}\}$ defines the spatial moments $\mu_n(t)$ for evolution of the Dirac delta function $C(\boldsymbol{r},t=0) = \delta(x - x_0)$, the set $\{\gamma^{(n)}\}$ determines the temporal moments $\mu_n(x) = \int_{-\infty}^{\infty}(t-t_0)^n P(x,t)dt$ of the resident time distribution $P(x,t)$ (RTD) for a suitable inlet boundary condition, such as the Heaviside step function $C(x=0,t) = H(t)$. We obtain

$$\mu_1(t) = \omega^{(1)}t, \quad \mu_2^{\star}(t) = -2\omega^{(2)}t, \quad \mu_3^{\star}(t) = 6\omega^{(3)}t,$$
$$\mu_4^{\star}(t) = 12t(-2\omega^{(4)} + {\omega^{(2)}}^2 t), \tag{9}$$

$$\mu_1(x) = \frac{x}{\gamma^{(1)}}, \quad \mu_2^{\star}(x) = 2\gamma^{(2)}x, \quad \mu_3^{\star}(x) = 6\gamma^{(3)}x,$$
$$\mu_4^{\star}(x) = 12x(2\gamma^{(4)} + {\gamma^{(2)}}^2 x). \tag{10}$$

Since one may restore $\{\omega^{(n)}\}$ from $\{\gamma^{(n)}\}$ with Eqs. (6), and vice versa, one may also restore the moments set from each other. In spatial dispersion, $\mathcal{U}$, D, Sk(t), and Ku(t) in Eq. (3) can be computed from $\omega^{(1)}$–$\omega^{(4)}$:

$$\mathcal{U} = \frac{1}{\gamma^{(1)}} = \omega^{(1)}, \quad D = \mathcal{U}^3\gamma^{(2)} = -\omega^{(2)},$$
$$\mathrm{Sk}(t) = \frac{3\omega^{(3)}t^{-1/2}}{\sqrt{2}|\omega^{(2)}|^{3/2}}, \quad \mathrm{Ku}(t) = -\frac{6\omega^{(4)}t^{-1}}{(\omega^{(2)})^2}. \tag{11}$$

As time increases, Sk(t) and Ku(t) tend to zero as $t^{-1/2}$ and t^{-1}, respectively.

In dimensionless (primed) variables, obtained with the characteristic length $\mathcal{L}$, velocity $\mathcal{U}$, and time $\mathcal{L}/\mathcal{U}$, solution of Eq. (1) is looked in the form

$$C(\boldsymbol{r}',t') = \frac{1}{2\pi}\tilde{\mathcal{P}}(\omega',\boldsymbol{r}')\exp[i(\gamma' x' - \omega' t')],$$
$$\gamma' = \mathcal{L}\gamma, \quad \omega' = \frac{\mathcal{L}}{\mathcal{U}}\omega. \tag{12}$$

By plugging ansatz (12) into Eq. (1), it reduces to *steady-state*ADE with the mass source for $\tilde{\mathcal{P}}(\omega',\boldsymbol{r}')$:

$$\nabla'\cdot(\tilde{\boldsymbol{U}}\tilde{\mathcal{P}}) - \mathrm{Pe}^{-1}\Delta'\tilde{\mathcal{P}} = i[\omega' - \gamma'\tilde{U}_x]\tilde{\mathcal{P}} + 2i\gamma'\mathrm{Pe}^{-1}\frac{\partial\tilde{\mathcal{P}}}{\partial x'}$$
$$- \mathrm{Pe}^{-1}{\gamma'}^2\tilde{\mathcal{P}},$$
$$\text{with} \quad \Delta' = \nabla'\cdot\nabla', \quad \nabla' = \mathcal{L}\nabla,$$
$$\tilde{\boldsymbol{U}} = \frac{\boldsymbol{U}}{\mathcal{U}}, \quad \mathrm{Pe} = \frac{\mathcal{U}\mathcal{L}}{D_0}. \tag{13}$$

The key point of the EMM is that the two functions $\tilde{\mathcal{P}}(\omega',\boldsymbol{r}')$ and $\gamma'(\omega')$ in Eq. (13) are expanded into series over ω' [cf. Eqs. (5)]:

$$\tilde{\mathcal{P}}(\omega',\boldsymbol{r}') = \sum_{n=0}^{\infty}\mathcal{B}^{(n)}(\boldsymbol{r}')(i\omega')^n, \quad \gamma'(\omega') = -i\sum_{n=1}^{\infty}\gamma'^{(n)}(i\omega')^n,$$
$$\gamma'^{(n)} = \frac{\mathcal{U}^n\gamma^{(n)}}{\mathcal{L}^{(n-1)}}, \quad \gamma_0'^{(1)} = 1. \tag{14}$$

The EMM formulates the mathematical algorithm by sequentially solving Eq. (13) with respect to the distribution $\{\mathcal{B}^{(n)}(\boldsymbol{r})\}$, called *extended B fields*, and the set of the coefficients $\{\gamma'^{(n)}\}$, under no-flux boundary condition imposed for $\{\mathcal{B}^{(n)}(\boldsymbol{r})\}$ at solid boundaries (the examples will be given below). In spatial dispersion, the set $\{\omega'^{(n)} = \frac{\omega^{(n)}}{\mathcal{U}\mathcal{L}^{(n-1)}}\}$ is restored with Eqs. (6) from the obtained solution $\{\gamma'^{(n)}\}$. This allows to compute the dimensionless time-independent coefficients k_T, Sk$_\star$, and Ku$_\star$:

$$k_T = \frac{D}{D_0} - 1 = \gamma'^{(2)}\frac{\mathcal{U}\mathcal{L}}{D_0} - 1 = -\omega'^{(2)}\frac{\mathcal{U}\mathcal{L}}{D_0} - 1,$$
$$\mathrm{Sk}_\star = \sqrt{\frac{\mathcal{U}t}{\mathcal{L}}}\mathrm{Sk}(t) = \frac{3\omega'^{(3)}}{\sqrt{2}|\omega'^{(2)}|^{3/2}},$$
$$\mathrm{Ku}_\star = \frac{\mathcal{U}t}{\mathcal{L}}\mathrm{Ku}(t) = -\frac{6\omega'^{(4)}}{(\omega'^{(2)})^2}. \tag{15}$$

TABLE I. This table gives dimensionless coefficients $\omega'^{(2)}$–$\omega'^{(4)}$ for spatial dispersion in the parabolic velocity profile imposed in cylindrical capillary ($\mathcal{L} = R$, $\mathrm{Pe} = \frac{2R\mathcal{U}}{D_0}$) and straight channel ($\mathcal{L} = H$, $\mathrm{Pe} = \frac{H\mathcal{U}}{D_0}$). The coefficients of the dispersivity k_T, skewness Sk$_\star$, and kurtosis Ku$_\star$ are expressed from $\omega'^{(2)}$–$\omega'^{(4)}$ with Eq. (15).

Shape	$\omega'^{(2)}$	$\omega'^{(3)}$	$\omega'^{(4)}$	k_T	$\mathrm{Sk}_\star = \mathrm{Sk}\times\sqrt{t\mathcal{U}/\mathcal{L}}$	$\mathrm{Ku}_\star = \mathrm{Ku}\times t\mathcal{U}/\mathcal{L}$
Circular	$-(\frac{2}{\mathrm{Pe}} + \frac{\mathrm{Pe}}{96})$	$\frac{\mathrm{Pe}^2}{11520}$	$\frac{41\mathrm{Pe}^3}{20643840}$	$\frac{\mathrm{Pe}^2}{192}$	$\frac{1}{10}\sqrt{3}\sqrt{\frac{\mathrm{Pe}^7}{(\mathrm{Pe}^2+192)^3}}$	$-\frac{123\mathrm{Pe}^5}{1120(\mathrm{Pe}^2+192)^2}$
Channel	$-(\frac{1}{\mathrm{Pe}} + \frac{\mathrm{Pe}}{210})$	$\frac{-\mathrm{Pe}^2}{69300}$	$\frac{\mathrm{Pe}^3}{2252250}$	$\frac{\mathrm{Pe}^2}{210}$	$-\frac{1}{22}\sqrt{\frac{21}{5}}\sqrt{\frac{Pe^7}{(Pe^2+210)^3}}$	$-\frac{84\mathrm{Pe}^5}{715(Pe^2+210)^2}$

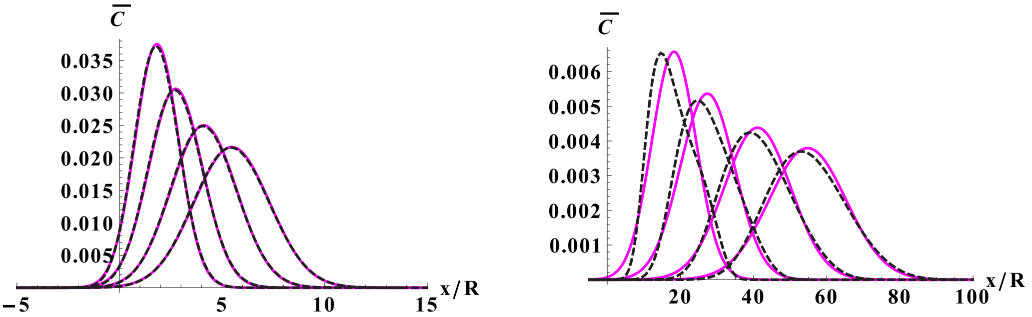

FIG. 2. This figure compares the averaged concentration profiles of solute advected by the parabolic velocity field in cylindrical capillary of $R = 10$ (l.u.) when Pe ≈ 9.5 (left diagram) and Pe ≈ 95 (right diagram). The profiles are restored (dashed-dotted line, black) from the predicted values for $\mathcal{U}$, $k_T^{(c)}$, Sk$_\star$, and Ku$_\star$ in Table II. They are compared to Gaussian distribution (solid line, magenta) where Sk$_\star$ = Ku$_\star$ = 0. The profiles are monitored at $t' = D_0/R^2 t \in [\frac{2\sqrt{3}}{9}, \frac{\sqrt{3}}{3}, \frac{\sqrt{3}}{2}, \frac{2\sqrt{3}}{3}]$.

Notice that $\mathcal{U}$ and k_T are the same for spatial and temporal dispersions but Sk$_\star$ and Ku$_\star$ [defined by replacing t by x for RTD in Eq. (15)] differ in this respect. The two dispersions were analytically and numerically illustrated [15] in a series of examples, such as the Darcy flow in heterogeneous stratified soil, the parabolic flow in stratified channel and double-porosity cylindrical capillary, the power-law fluid in cylindrical tube, and shallow flow in differently shaped pipes. In particular, the four nondimensional components $\{\gamma'^{(n)}\}$ have been reported [15] for Poiseuille flow in a capillary and straight channel [see, respectively, Eqs. (97)–(103) and (107) there]. The corresponding solutions for $\{\omega'^{(n)}\}$ and k_T, Sk$_\star$, and Ku$_\star$ from Eq. (15) are reported in Table I. Notice that in a capillary, we apply $\mathcal{L} = R$ in EMM following [15], but all our final results are reexpressed via Péclet number $\text{Pe} = 2R\mathcal{U}/D_0$, as adopted in this work. The dispersivity coefficient k_T takes the well-known Taylor-Aris values, labeled as $k_T^{(s)}$ in straight channel and $k_T^{(c)}$ in cylindrical capillary. Given $\mathcal{U}$, k_T, Sk$_\star$, and Ku$_\star$, one may visualize the profiles with the help of the entropy-maximization reconstruction procedure [16].

Figure 2 compares the reconstructed profiles in the capillary of radius $R = 10$ (grid nodes) relative to the Gaussian distribution, at Pe ≈ 9.5 and Pe ≈ 95. The reconstruction is performed from the first four moments. These and other numerical simulations apply the parameter range from Table II for molecular-diffusion value D_0 (l.u.) and mean velocity $\mathcal{U}$ (l.u.). The Gaussian distribution obeys Eq. (2) with $D = D_0(1 + k_T^{(c)})$. It has therefore the same values for the two first moments as the EMM, but zero skewness and kurtosis in the case of the spatial spreading of the Dirac plume. The difference with the Gaussian profiles is observable for Pe ≈ 95 where, according to Table II, the nonzero (physical values) are Sk$_\star \approx 1.63$ and Ku$_\star \approx -9.99$, so that the physical distribution is skewed right and slightly more flat than the normal one. The visual "asymmetric" effects are stronger at shorter time but the higher are these effects the greater is the number of moments required for the reliable reconstruction [15]. Additionally, the reconstruction procedure may manifest the presence of instabilities in sharp profiles. In this work, the numerical moments, rather than the profiles, will be compared to their physical values predicted by the EMM from Eq. (1) and reported in Table II. The comparison of the moments is much more sensitive to the quality of the numerical solutions, especially in open flow, where Sk$_\star$ and Ku$_\star$ are relatively weak and the truncation or boundary effect may compete with them.

B. Two-relaxation-time TRT-ADE scheme

The TRT schemes [28,34,35] assume the d-dimensional discrete-velocity set consisting of zero-amplitude vector $\boldsymbol{c}_0$ and $Q_m = Q - 1$ vectors $\boldsymbol{c}_q$ connecting cuboid-grid nodes $\boldsymbol{r}$. Each vector $\boldsymbol{c}_q$ has the opposite one: $\boldsymbol{c}_{\bar{q}} = -\boldsymbol{c}_q$, and the pair of

TABLE II. This table gives parameters for four numerical experiments with the parabolic profile imposed in capillary of radius $R = 5 \times 2^n$, $n = 0,1,2$. The molecular diffusion coefficient is $D_0 = c_e\Lambda^-$, $\text{Pe} = \frac{2R\mathcal{U}}{D_0}$. The mean velocity $\mathcal{U} = |U|^{\max}/2$ is set with $|U|^{\max}(n=0) = \sqrt{c_e}|_{c_e=1/30} = 2 \times 0.091287$. The Sk$_\star$ and Ku$_\star$ apply their solutions from Table I. These two coefficients are equal to zero in Gaussian distribution.

Expt.	$\text{Pe} = \frac{2R\mathcal{U}}{c_e\Lambda^-}$	$\mathcal{U}$	c_e	$(\Lambda^-)^2$	$k_T^{(c)} = \frac{\text{Pe}^2}{192}$	$\text{Sk}_\star = \text{Sk} \times \sqrt{t\mathcal{U}/R}$	$\text{Ku}_\star = \text{Ku} \times t\mathcal{U}/R$
I	2.47461	$0.091287/2^n$	$\frac{1}{3}$	$\sqrt{\frac{3}{2}}$	3.19×10^{-2}	1.48×10^{-3}	-2.6×10^{-4}
II	9.48682	$0.091287/2^n$	$\frac{1}{3}$	$\frac{1}{12}$	4.687×10^{-1}	9.62×10^{-2}	-1.06×10^{-1}
III	24.74612	$0.091287/2^n$	$\frac{1}{30}$	$\sqrt{\frac{3}{2}}$	3.19	5.72×10^{-1}	−1.58
IV	94.8682	$0.091287/2^n$	$\frac{1}{30}$	$\frac{1}{12}$	46.87	1.63	−9.99

two opposite velocities $\{\boldsymbol{c}_q,\boldsymbol{c}_{\bar{q}}\}$ is called link. Accordingly, the two populations per link $f_q(\boldsymbol{r},t)$ and $f_{\bar{q}}(\boldsymbol{r},t)$ are decomposed into their symmetric and antisymmetric components: $f_q^{\pm}=(f_q\pm f_{\bar{q}})/2$. The TRT scheme updates them with the help of the two relaxation parameters $s^{\pm}\in]0,2[$:

$$\begin{aligned} f_q(\boldsymbol{r}+\boldsymbol{c}_q,t+1) &= f_q(\boldsymbol{r},t)+g_q^{+}+g_q^{-},\\ g_q^{\pm} &= -s^{\pm}(f_q^{\pm}-e_q^{\pm}),\quad q=0,\dots,\frac{Q_m}{2},\\ f_{\bar{q}}(\boldsymbol{r}-\boldsymbol{c}_q,t+1) &= f_{\bar{q}}(\boldsymbol{r},t)+g_q^{+}-g_q^{-},\quad q=1,\dots,\frac{Q_m}{2}. \end{aligned} \tag{16}$$

The two eigenfunctions $\Lambda^{\pm}=\frac{1}{s^{\pm}}-\frac{1}{2}$ are positive. The generic equilibrium distribution $\{e_q=e_q^{+}+e_q^{-}\}$ for the modeling of the isotropic or anisotropic ADE can be found in [45] [see Eq. (26) there]. It operates with the minimal coordinate discrete-velocity sets dDQ(2D + 1), as the d2Q5 and d3Q7, and the "hydrodynamic" ones, as the d2Q9, d3Q13, d3Q15, and d3Q19. This work focuses on the linear isotropic schemes d2Q9 in 2D and d3Q15 in 3D. A special attention will be paid to their respective coordinate subsets, the d2Q5 and d3Q7. The common form for equilibrium distribution of d2Q9 (2D) and d3Q15 (3D) schemes, $\{e_q^{\pm}(\boldsymbol{r},t)\}$ is computed with the local mass value $C(\boldsymbol{r},t)=\sum_{q=0}^{Q_m}f_q$ and prescribed velocity $\boldsymbol{U}(\boldsymbol{r},t)=\{U_\alpha,\alpha=1,\dots,d\}$:

$$\begin{aligned} e_q^{+}(\boldsymbol{r},t) &= C\left[t_c^{(m)}c_e+t_c^{(u)}\bar{U}^2+\frac{1}{2}\left(U_\alpha^2-\bar{U}^2\right)\right],\\ e_q^{-} &= t_c^{(a)}CU_\alpha c_{q\alpha},\quad \text{if } c_{q\alpha}\neq 0,\quad c_{q\alpha}c_{q\beta}|_{\alpha\neq\beta}=0 \end{aligned} \tag{17a}$$

$$\begin{aligned} e_q^{+}(\boldsymbol{r},t) &= C\left(t_d^{(m)}c_e+t_d^{(u)}\bar{U}^2+\frac{1}{N_d}\sum_{\alpha\neq\beta}U_\alpha U_\beta c_{q\alpha}c_{q\beta}\right),\\ e_q^{-} &= t_d^{(a)}C\boldsymbol{U}\cdot\boldsymbol{c}_q,\quad \text{if } c_{q\alpha}c_{q\beta}|_{\alpha\neq\beta}\neq 0 \end{aligned} \tag{17b}$$

$$\begin{aligned} e_0^{+}(\boldsymbol{r},t) &= C(\boldsymbol{r},t)-2\sum_{q=1}^{\frac{Q_m}{2}}e_q^{+}(\boldsymbol{r},t),\quad e_0^{-}=0,\\ \text{with }\ \bar{U}^2 &= \frac{U^2}{d},\quad U^2=\sum_{\alpha=1}^{d}U_\alpha^2. \end{aligned} \tag{17c}$$

In these relations, Eq. (17a) applies on the subset of $2d$ "coordinate" discrete velocities, with $2d=4$ in d2Q9 and $2d=6$ in d3Q15, Eq. (17b) operates on the $N_d=4$ "diagonal" links in d2Q9 and 8 "diagonal" links in d3Q15; the last equation for immobile population assures local mass conservation by the TRT operator (16). The three independent, non-negative, isotropic weight families $t_q^{(\cdot)}=\{t_q^{(m)},t_q^{(a)},t_q^{(u)}\}$ obey the same constraint: $\sum_{q=1}^{Q_m}t_q^{(\cdot)}c_{q\alpha}c_{q\beta}=\delta_{\alpha\beta}$, that is the coordinate $t_c^{(\cdot)}$ and the diagonal $t_d^{(\cdot)}$ weight values are related as

$$\begin{aligned} t_d^{(\cdot)} &= \frac{1-2t_c^{(\cdot)}}{N_d},\quad t_c^{(\cdot)}\in\left[0,\frac{1}{2}\right],\\ \text{with }\ N_d &= \sum_{q=1}^{Q_m}c_{q\alpha}^2c_{q\beta}^2,\quad \alpha\neq\beta,\\ N_d &= 4\ (\text{d2Q9}),\quad N_d=8\ (\text{d3Q15}). \end{aligned} \tag{18}$$

Minimal schemes. The coordinate schemes dDQ(2D + 1) lack the diagonal links, Eq. (17b) vanishes in them whereas Eq. (17a) reads as

$$\begin{aligned} &\text{d1Q3,d2Q5,d3Q7}:t_c^{(\cdot)}=\tfrac{1}{2},\quad t_d^{(\cdot)}=0,\\ &e_q^{+}=\tfrac{1}{2}C(c_e+U_\alpha^2c_{q\alpha}^2),\quad e_q^{-}=\tfrac{1}{2}CU_\alpha c_{q\alpha},\quad \text{if } c_{q\alpha}\neq 0,\quad q=1,\dots,Q_m=2d. \end{aligned} \tag{19}$$

In the absence of external mass source, the exact mass-conservation equation of the TRT scheme (16) reads as

$$\sum_{q=0}^{Q_m}g_q^{+}(\boldsymbol{r},t)=0,\quad \forall\,\boldsymbol{r},\quad \forall\,t. \tag{20}$$

We will not apply any mass source but the prescribed local mass-source quantity $S(\boldsymbol{r},t)$ can be readily included, e.g., by adding its distribution $S_q(\boldsymbol{r},t)/s^{+}$ to e_q^{+} for $q\neq 0$, and $[S(\boldsymbol{r},t)-\sum_{q=1}^{Q_m}S_q]/s^{+}$ to $e_0(\boldsymbol{r},t)$, resulting in $\sum_{q=0}^{Q_m}g_q^{+}(\boldsymbol{r},t)=S(\boldsymbol{r},t)$ in Eq. (20). In this way, the truncation [35] and recurrence equations based bulk and boundary analysis [42] will keep their form, automatically providing the spatial and temporal corrections due to the source distribution, similar to flow schemes [52–54]. The macroscopic concentration value should be redefined: $C(\boldsymbol{r},t)\to C(\boldsymbol{r},t)+S(\boldsymbol{r},t)/2$, in order to properly parametrize the solution by the nondimensional numbers of the problem [42].

Second-order-accurate approximation. In this work, we limit ourselves to either constant velocity $\boldsymbol{U}=U_x=\mathcal{U}$ or the streamwise-invariant parabolic profiles $U_x(y)$ and $U_x(r)$ in straight channel and cylindrical capillary, respectively. The Chapman-Enskog expansion [34,45] and the recurrence-equations-based analysis [35,41] show that the quadratic velocity terms $U_\alpha U_\beta$ in Eq. (17) are sufficient to remove the entire second-order numerical-diffusion tensor in streamwise-invariant flows, at least. We further confirm this result by numerical computation in cylindrical capillary. The second-order-accurate approximation of Eq. (20) fits Eq. (1) with the molecular diffusion coefficient $D_0=c_e\Lambda^{-}$ (in lattice units). A comparison with the analytical or physical results requires to set the same Péclet numbers. Thereby, whereas $\Lambda^{-}=\frac{1}{s^{-}}-\frac{1}{2}$ determines D_0, the $\Lambda^{+}=\frac{1}{s^{+}}-\frac{1}{2}$, and hence their product $\Lambda=\Lambda^{-}\Lambda^{+}$, is free tunable. When Λ is fixed, the two relaxation rates are linked through simple relation: $s^{+}=\frac{2(2-s^{-})}{2-s^{-}+4s^{-}\Lambda}$.

Stability. The diffusion-coefficient scale parameter $c_e\in]0,c_e^{(\max)}]$ can be freely selected inside its stability interval [35,43], with $c_e^{(\max)}=\frac{1}{d}$ in minimal models, $c_e^{(\max)}=\frac{1}{4t_c^{(m)}}$ in d2Q9, and $c_e^{(\max)}=\frac{1}{1+4t_c^{(m)}}$ in d3Q15. Therefore, the diagonal mass weight allows to increase $c_e^{(\max)}$ and reach large diffusion coefficients with relatively small and more accurate Λ^-; this property is important in highly nonlinear ADE macroscopic flow and transport problems, e.g., [55]. In d-dimensional *constant* velocity field U, the square of velocity amplitude $U^2 = \sum_{\alpha=1}^{d} U_\alpha^2$ is restricted in d2Q5 and d3Q7 to the simple stability condition [35,43]: $U^2 \leqslant \min\{1 - dc_e, \frac{d}{d-1}c_e\}$. The first condition is enforced by "diffusion-dominant" stability branch, where $U^2 \leqslant 1 - dc_e$ guarantees the positivity of the immobile weight e_0/C. The condition $e_0/C > 0$ is also necessary in the d3Q15 where the "diffusion branch" then dictates: $U^2 \leqslant \min\{1 - c_e, 3(1 - c_e/c_e^{(\max)})/(1 + 4t_c^{(u)})\}$ when $t_c^{(u)} = \frac{1}{2}$; when $t_c^{(u)} \neq \frac{1}{2}$, the d3Q15 has the additional stability constraint $U^2 \leqslant 6t_c^{(m)}c_e/(1 - 2t_c^{(u)})$. This last condition noticeably restricts the efficiency of the model at high Pe when $c_e \to 0$; thereby, we adopt $t_c^{(u)} = \frac{1}{2}$ in d2Q9 and d3Q15. In d2Q9, $e_0/C > 0$ is not necessary and the "diffusion branch" imposes $U^2 \leqslant \min\{1 - c_e, 1 - 4t_c^{(m)}c_e/(2t_c^{(u)}), \quad t_c^{(u)} \neq 0\}$. The necessary "advection-dominant" stability branch [43] of the minimal sets is $U^2 \leqslant \frac{d}{d-1}c_e$. It is too restrictive when $c_e \to 0$ and it can be in principle relaxed in d2Q9 and d3Q15 schemes thanks to the (mixed) anti-numerical-diffusion terms $U_\alpha U_\beta$, $\alpha \neq \beta$ in Eq. (17b). However, this stability bound effectively vanishes only for several (optimal) combinations of Λ and weights, typically, when $\Lambda = \frac{1}{4}$ and $t_c^{(a)} = t_c^{(m)} = \frac{1}{4}$, $\forall\ t_c^{(u)}$ in d2Q9 and $t_c^{(a)} = t_c^{(m)} = \frac{1}{4}$, $t_c^{(u)} = \frac{1}{2}$ in d3Q15 [in more detail, see [35]: Eqs. (3.19) and (3.20) and Eqs. (3.23) and (3.24) for (anisotropic) factor $a_\alpha = 0$ and isotropic diffusion tensor, and Eq. (3.7) for optimal weights].

The OTRT subclass. The case $\Lambda = \frac{1}{4}$, where the arithmetical-mean value of two relaxation rates is equal to one, that is $s^+ = 2 - s^-$, is referred to as the "optimal subclass" OTRT due to its distinguished stability properties [43]. The key point is that, except for $\Lambda = \frac{1}{4}$, the effective stable velocity amplitude depends on Λ^- [43,44]. By respecting necessary stability conditions, the $\Lambda = \frac{1}{4}$ should allow to reach any Pe by decreasing Λ^-. The necessary and sufficient stability criteria, in parameter space $\{c_e, \Lambda^-, \Lambda, \max[U(y)]\}$ of the d2Q5, are examined [41] for maximum velocity amplitude in straight Poiseuille flow. The results [41] confirm the theoretical predictions for $\Lambda = \frac{1}{4}$ and demonstrate that the smaller Λ values ($\Lambda = \frac{1}{6}$ and, especially, $\Lambda = \frac{1}{12}$) affect the stable velocity amplitude noticeably as c_e or Λ^- reduce to 0. In work [12], Pe is adjusted with c_e while mean velocity amplitude and $\Lambda^- = 0.0625$ are fixed [we note that the convergence towards the Taylor regime may improve when Λ^- increases, whereas c_e can be decreased by respecting $|U|^{\max}(c_e)$ OTRT stability line [43]]. The effective stable parameter space of the full stencils is only partly examined numerically [41].

Fourth-order-accurate approximation. The exact form of the nonequilibrium post-collision component $g_q^\pm$ in Eq. (16) is provided by *the recurrence equations* [35,41,42] [we signalize a typo in [35], Eq. (2.2), where $(\Lambda^\pm - \frac{1}{4})$ should be replaced by $(\Lambda - \frac{1}{4})$]:

$$g_q^\pm(\boldsymbol{r},t) = \big[\bar{\Delta}_t e_q^\pm + \bar{\Delta}_q e_q^\mp - \Lambda^\mp\big(\bar{\Delta}_q^2 - \bar{\Delta}_t^2\big)e_q^\pm + \big(\Lambda - \tfrac{1}{4}\big)\big(\bar{\Delta}_q^2 - \bar{\Delta}_t^2\big)g_q^\pm - \tfrac{1}{2}\bar{\Delta}_t^2 g_q^\pm - (\Lambda^\pm + \Lambda^\mp)\bar{\Delta}_t g_q^\pm\big](\boldsymbol{r},t),$$
$$q = 0, \ldots Q_m, \quad \Lambda = \Lambda^-\Lambda^+. \tag{21}$$

They are expressed via the temporal and spatial central-difference operators. In time, $\bar{\Delta}_t\psi(\boldsymbol{r},t) = \frac{1}{2}[\psi(\boldsymbol{r},t+1) - \psi(\boldsymbol{r},t-1)]$ and $\bar{\Delta}_t^2\psi(\boldsymbol{r},t) = \psi(\boldsymbol{r},t+1) - 2\psi(\boldsymbol{r},t) + \psi(\boldsymbol{r},t-1)$. In space, the central differences apply link wisely: $\bar{\Delta}_q\psi(\boldsymbol{r},t) = \frac{1}{2}[\psi(\boldsymbol{r}+\boldsymbol{c}_q,t) - \psi(\boldsymbol{r}-\boldsymbol{c}_q,t)]$ and $\bar{\Delta}_q^2\psi(\boldsymbol{r},t) = \psi(\boldsymbol{r}+\boldsymbol{c}_q,t) - 2\psi(\boldsymbol{r},t) + \psi(\boldsymbol{r}-\boldsymbol{c}_q,t)$, $\forall\ \psi = \{e_q^\pm, g_q^\pm\}$. The mass-conservation equation (20) becomes [35,41]

$$\left[\bar{\Delta}_t\sum_{q=0}^{Q_m} e_q^+ + \sum_{q=1}^{Q_m}\bar{\Delta}_q e_q^-\right](\boldsymbol{r},t) = \left[\Lambda^-\left(\sum_{q=1}^{Q_m}\bar{\Delta}_q^2 e_q^+ - \sum_{q=0}^{Q_m}\bar{\Delta}_t^2 e_q^+\right) - \left(\Lambda - \frac{1}{4}\right)\sum_{q=1}^{Q_m}\bar{\Delta}_q^2 g_q^+\right](\boldsymbol{r},t). \tag{22}$$

Equations (21) and (22) are exact for the TRT scheme (16) with any equilibrium $\{e_q^\pm\}$ provided that (i) the two relaxation functions are space-time independent and (ii) all populations in grid node $\boldsymbol{r}$ are issued from the propagation step, i.e., $\boldsymbol{r}$ is a *bulk node*. In Appendix A, we resume the fourth-order-accurate approximation [35,41] of Eq. (22) in the form $\partial_t C(\boldsymbol{r},t) = [R_1 + R_2 + R_3 + R_4]C(\boldsymbol{r},t)$, as given by Eq. (A1). This approximation assumes any mass-conserving equilibrium distribution $e_q^\pm = E_q^\pm C$, $\sum_{q=0}^{Q_m} E_q^+ = 1$, linear with respect to the concentration distribution $C(\boldsymbol{r},t)$ (it is equal to local mass for homogeneous soil but differs from it in heterogeneous soil porosity [15]). The first- and second-, third-, and then fourth-order terms are specified by Eqs. (A3), (A4), and (A6), respectively. In them, all differential operators are expressed via the two families of the even-order and odd-order operators (A2): $[S_{2k}]C = [\sum_{q=1}^{Q_m}\partial_q^{2k}E_q^+]C$ and $[S_{2k-1}]C = [\sum_{q=1}^{Q_m}\partial_q^{2k-1}E_q^-]C$: they apply the directional derivatives $\partial_q = (\nabla\cdot\boldsymbol{c}_q)$ to symmetric or antisymmetric equilibrium factors $E_q^\pm(\boldsymbol{r},t)$. The presented fourth-order approximation is valid from one to three dimensions; its truncation coefficients are all specified by relaxation eigenfunctions, via Λ^- and Λ. The pure-diffusion fourth-order equation is given by Eqs. (A7) and (A8). The apparent fourth-order equations will be exemplified for channel and cylindrical capillary. The derivation [35,41] of the fourth-order approximation is exemplified in Appendix B for OTRT subclass. The distinguished properties of the OTRT subclass are all due to the vanishing of the last term in Eq. (22).

Extensions. Our truncation approach readily extends to source terms and nonlinear equilibrium functions because Eqs. 21 and (22) remain valid for them (see examples in [54]). In case of the discontinuous collision components, the bulk equations are linked through implicit interface conditions [28], as demonstrated for steady-state problems [28,29,54] and transient analysis in heterogeneous soil [15].

The most-accurate relaxation rates. It is well understood that the free collision parameter Λ controls the truncation [35,41], boundary, and interface accuracy [28,29,32,47], on top of stability [35,43–45]. The two particular values, such as $\Lambda = \frac{1}{12}$ and $\frac{1}{6}$, provide, respectively, the third- and fourth-order accuracy at steady state by vanishing the coefficients of the relevant spatial truncation corrections (A5) and (A8). In addition, one should fix $\Lambda^- = \sqrt{\frac{1}{12}}$ to vanish the third- and fourth-order truncation coefficients completely in transition. This explains our particular interest for this choice in Table II. However, the third- and fourth-order corrections cannot vanish simultaneously, except for some particular c_e and U parameter choices [15,35]. Thereby, we focus on the interval $\Lambda \in [\frac{1}{12},\frac{1}{4}]$.

Hydrodynamic weights. The usually used "hydrodynamic" mass weight which satisfies the second constraint $S_d(t_q^{(\cdot)}) = \sum_{q:\alpha\neq\beta} t_q^{(\cdot)} c_{q\alpha}^2 c_{q\beta}^2 = \frac{1}{3}$ [with $S_d(t_q^{(\cdot)}) = t_d^{(\cdot)} \sum_{q:\alpha\neq\beta} c_{q\alpha}^2 c_{q\beta}^2 = 1 - 2t_c^{(m)}$ and $t_c^{(m)} = \frac{1}{3}$ in d2Q9 and d3Q15] is not the most stable [35,43,44], but it maintains the isotropy of the fourth-order linear diffusion form, as shown for d2Q9 in details [35] [Eq. (5.8) there], and discussed in this work for d3Q15. Since the second-order numerical diffusion of the scheme is dominated by its numerical dispersion as Pe increases [41], the third- and fourth-order truncation terms related to the anti-numerical-diffusion correction $U_\alpha U_\beta$ in Eq. (17) are believed to be not relevant for this study, except perhaps in plug flow (see also [36,56,57] for similar terms). The isotropy of these terms can be explored on the supplied truncation form. As has been said, we operate them in all analytical and numerical results with the coordinate stencil $t_c^{(u)} = \frac{1}{2}$, for its better stability in d3Q15, rather then with its "hydrodynamic" choice (adopted in flow models) provided in work [43]. In turn, the "hydrodynamic" velocity weight $t_c^{(a)} = \frac{1}{3}$ assures the isotropy of the third-order linear advection correction in d2Q9 model [Eqs. (5.12)–(5.14) in [35]], but this property is irrelevant for the coordinate-axis-aligned, streamwise-invariant velocity profile examined here.

Finite differences. When $\Lambda = \frac{1}{4}$, the last term vanishes in Eq. (22) and, despite the explicit marching in time, the apparent OTRT time scheme matches the discretization of the *three-level time difference* [35]. In this case, the exact mass-conservation equation is similar to leap-frog central-convective Du Fort–Frankel–diffusion (LFCCDF) scheme [58], which combines the leap-frog difference (LF) for the time term, here $\bar{\Delta}_t \sum_{q=0}^{Q_m} e_q^+ = \bar{\Delta}_t C = \frac{1}{2}[C(\boldsymbol{r},t+1) - C(\boldsymbol{r},t-1)]$, the central difference (CC) for the convective term, here: $\sum_{q=1}^{Q_m} \bar{\Delta}_q e_q^- = \bar{\nabla} \cdot \boldsymbol{U} C$, and the Du Fort–Frankel–type (DF) three-time-level diffusion term [59], like $D_0^{fd} \Delta^2 C \approx \frac{D_0^{fd}}{\delta_x^2}[C(x+\delta_x,t) - C(x,t+\delta_t) - C(x,t-\delta_t) + C(x-\delta_x,t)]$ in 1D. In OTRT, the three-time-level diffusion term takes the form $\Lambda^-[c_e \Delta^2 C(\boldsymbol{r},t) - \bar{\Delta}_t^2 C(\boldsymbol{r},t)]$; it produces the DF form with $D_0^{fd} = \frac{\Lambda^-}{d}\frac{\delta_x^2}{\delta_t}$ on the coordinate stencil in stability limit $c_e = \frac{1}{d}$ where $e_0 = 0$ (in 1D, the d1Q3 with $c_e = 1$ reduces to d1Q2 which is intensively compared with the finite-difference schemes [60–62]). In OTRT, both coefficients c_e and Λ^- can be adjusted under Pe constraint. In particular, $\Lambda^- = \Lambda^+ = \frac{1}{2}$ reduces the OTRT to the particular BGK model ($\tau = 1$), which is well known to be equivalent with the forward-time central differences (FTCS) scheme [63], using $\bar{\Delta}_t C + \frac{1}{2}\bar{\Delta}_t^2 C = C(t+1) - C(t)$ in Eq. (22). Further details on this issue and the mapping of the isotropic and anisotropic equilibrium weights, and anti-numerical-diffusion equilibrium term, to finite-difference spatial stencils and Lax-Wendroff (modified) MFTCS scheme [63] can be found in [35]; their stability criteria are compared [43] for the OTRT and FTCS-MFTCS on the minimal stencils. It follows that all present derivations can be readily extended to the LFCCDF and FTCS-MFTCS schemes at the same Péclet and in a cuboid grid.

C. Physical, truncation, and numerical moments

We will construct bulk predictions for the coefficients of dispersivity $k_T^{(\mathrm{tr})}$, skewness $\mathrm{Sk}_\star^{(\mathrm{tr})}$, and kurtosis $\mathrm{Ku}_\star^{(\mathrm{tr})}$ given by Eq. (15). They will be derived from the fourth-order-accurate ADE of the TRT scheme. Although the truncation coefficients in Eqs. (A4)–(A6) are all set by the relaxation functions Λ^- and Λ, their high-order differential operators depend on c_e and weights, altogether making the fourth-order-accurate equations be fixed by Pe, Λ, and weights only at steady state. Thereby, it should be expected that, for fixed diffusion value $D_0 = c_e \Lambda^-$ and Pe, the numerical distributions and their transport characteristics depend on the individual values c_e and Λ^-. The derived solutions $k_T^{(\mathrm{tr})}$, $\mathrm{Sk}_\star^{(\mathrm{tr})}$, and $\mathrm{Ku}_\star^{(\mathrm{tr})}$ will be compared to their reference (physical) solutions from Table I. Their relative differences are measured as follows:

$$\mathrm{err}_D^{(\mathrm{tr})} = \frac{1 + k_T^{(\mathrm{tr})}}{1 + k_T} - 1, \quad \mathrm{err}(\mathrm{Sk}) = \frac{\mathrm{Sk}_\star^{(\mathrm{tr})}}{\mathrm{Sk}_\star} - 1,$$

$$\mathrm{err}(\mathrm{Ku}) = \frac{\mathrm{Ku}_\star^{(\mathrm{tr})}}{\mathrm{Ku}_\star} - 1. \tag{23}$$

In simulations, we compute $\bar{C}(x,t) = \langle C(\boldsymbol{r},t)\rangle$ via the arithmetical averaging of the grid-node solution over the cross section normal to the x axis. The apparent velocity $\mathcal{U}^{(\mathrm{num})}$ is extracted from the first raw moment and then it is employed in the computation of the central spatial moments $\mu_n^\star(t)$. The $\omega^{(2)}$–$\omega^{(4)}$ are derived with the help of Eqs. (9) from the set $\{\mu_n^\star(t)\}$ separated by the time interval δ_t:

$$\begin{aligned}
\mathcal{U}^{(\mathrm{num})} &= \frac{\mu_1(t+\delta_t) - \mu_1(t)}{\delta_t},\\
D^{(\mathrm{num})} &= -\omega^{(2,\mathrm{num})} = \frac{\mu_2^\star(t+\delta_t) - \mu_2^\star(t)}{2\delta_t},\\
\omega^{(3,\mathrm{num})} &= \frac{\mu_3^\star(t+\delta_t) - \mu_3^\star(t)}{6\delta_t},\\
\omega^{(4,\mathrm{num})} &= -\frac{\mu_4'(t+\delta_t) - \mu_4'(t)}{24\delta_t},\\
\mu_4'(t) &= \mu_4^\star(t) - 12(\omega^{(2,\mathrm{num})})^2 t^2.
\end{aligned} \tag{24}$$

When the Taylor regime is reached, these values become time independent and the numerical values of the coefficients $k_T^{(\mathrm{num})}$, $\mathrm{Sk}_\star^{(\mathrm{num})}$, and $\mathrm{Ku}_\star^{(\mathrm{num})}$ are computed with Eqs. (11) from Eq. (24).

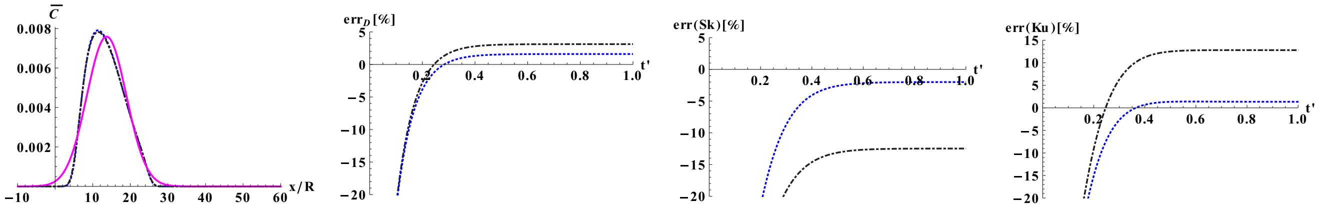

FIG. 3. The first diagram displays together two distribution profiles computed by the d3Q15 BB with $\Lambda = \frac{1}{4}$ (black, dotted-dashed line) and $\Lambda = \frac{1}{12}$ (blue, dotted line) in the same simulations as in Fig. 2 but at earlier time $t' = \frac{\sqrt{3}}{6}$. The d3Q15 BB is applied with $t_c^{(a)} = t_c^{(u)} = \frac{1}{2}$, $t_c^{(m)} = \frac{1}{3}$, $\Lambda = \frac{1}{4}$, Pe ≈ 95. The Gaussian distribution ($k_T = k_T^{(c)}$, $\text{Sk}_\star = \text{Ku}_\star = 0$) is plotted by solid line (magenta). Three next diagrams plot the relative differences of the numerical dispersion, skewness, and kurtosis with respect to their reference values from Table I, with $\Lambda = \frac{1}{4}$ (black, dotted-dashed line) and $\Lambda = \frac{1}{12}$ (blue, dotted line).

Their relative differences with predictions in Table I are measured as given in Eq. (23). In 3D we will apply the d3Q15 scheme combined with the bounce-back rule on impermeable walls, referred to as d3Q15 BB. The first diagram in Fig. 3 shows that the numerical profiles in cylindrical capillary are nearly the same for $\Lambda = \frac{1}{12}$ and $\frac{1}{4}$, even at the relatively early time t. At the same time, the three last diagrams in Fig. 2 show that the corresponding values of err_D, err(Sk), and err(Ku), computed with Eqs. (23) for $k_T^{(\text{num})}$, $\text{Sk}_\star^{(\text{num})}$, and $\text{Ku}_\star^{(\text{num})}$, noticeably differ for the two Λ values. This illustrates the premise that the profiles alone are not sufficient to characterize the numerical accuracy and parameter dependency.

D. Boundary-layer effects

The validation of the truncation analysis requires the consideration of the distinct additional error sources, namely, summation, discretization, and boundary-layer components in the obtained numerical values. The two first effects are studied in this work. The principal boundary-layer effects of the bounce-back rule were recently quantified for channel [50] and extended for cylindrical capillary in the conjoined investigation [51]. These results are briefly resumed in this section.

In straight channel, the specular-forward nonlocal reflection (SNL hereafter), involved to compute incoming populations in boundary nodes along the flat impermeable wall, presents an ideal no-flux mass-conserving boundary rule, free from the spurious effects for any equilibrium weights [47,50]. The bounce-back reflection (BB hereafter) and SNL coincide in straight channel for minimal schemes. Otherwise, on the diagonal weight stencil, the bounce back constrains to zero not only the normal but also the tangential advection-diffusion flux [47]. This artifact modifies the advective velocity, diffusion, and dispersion coefficients, depending on the diagonal-weight values. Due to this reason, the SNL is mainly employed in this work to verify truncation analysis in straight channel. These results are compared [51] with the bounce-back simulations, with the purpose to validate and reduce boundary-layer effects.

The situation in cylindrical capillary is similar: it is found [51] that only the d3Q7 BB scheme produces the prescribed velocity $\mathcal{U}$ and diffusion coefficient D_0 correctly. However, the d3Q7 lacks the isotropic fourth-order accurate diffusion form, required for the truncation estimate (see below), while the SNL does not apply well in the staircase discretization of the cylindrical pipe. Because of this, we apply the d3Q15 BB scheme with full (free) mass and velocity stencil, but account for boundary-layer diffusion and advection effects.

Pure diffusion. In the absence of the boundary effects in straight channel and cylindrical pipe, the apparent diffusion coefficient $D^{(\text{num})}$ in Eq. (24), derived from the second moment in pure diffusion simulations, is equal to the imposed molecular diffusion value D_0. In particular, that agreement is assured either by the SNL in straight channel (for any equilibrium weights) or by the d3Q7 BB scheme in cylindrical capillary otherwise. Using the bounce-back rule, $D^{(\text{num})} = D_0$ only on the coordinate mass-weight stencil $t_c^{(m)} = \frac{1}{2}$; a retardation of the spreading takes place with the d2Q9 and d3Q15 BB schemes due to the diminution of the effective diffusion coefficient when $t_c^{(m)} \neq \frac{1}{2}$. This effect will be quantified via $\text{err}_D^{(bb)}$ (with $k_T = 0$ in pure diffusion and plug flow):

$$\begin{aligned} t_c^{(m)} &= \frac{1}{2}, \quad t_d^{(m)} = 0 : D^{(\text{num})} \equiv D_0 \ \text{ if } \ \boldsymbol{U} = 0, \\ t_c^{(m)} &\neq \frac{1}{2}, \quad t_d^{(m)} \neq 0 : \text{err}_D^{(bb)}\big(t_c^{(m)}, \Lambda, \mathcal{L}\big) \\ &= \frac{D^{(\text{num})}(\boldsymbol{U} = 0) - D_0}{D}, \\ D &= D_0(1 + k_T). \end{aligned} \tag{25}$$

The functional dependency $\text{err}_D^{(bb)}(t_c^{(m)}, \Lambda, \mathcal{L})$ is provided by the exact solution [50] in straight channel and approximate solution [51] in cylindrical capillary. The $\text{err}_D^{(bb)}$ linearly depends on $t_d^{(m)}$, but its dependency on Λ is nonlinear. When $\Lambda = \frac{1}{4}$, it takes a simple form in straight channel: $\text{err}_D^{(bb)}(\Lambda = \frac{1}{4}) = -\frac{1 - 2t_c^{(m)}}{H}$. Since $\text{err}_D^{(bb)}$ is independent of the velocity amplitude, it can be measured in a pure-diffusion simulation at fixed Λ. This strategy is adopted in this work for the cylindrical capillary. Once measured in a given discretization, the relative correction (25) (linear with $t_d^{(m)}$) is accounted in entire dispersion error [see Eq. (27)].

Velocity. Similarly, in the absence of the boundary effects in straight channel and cylindrical capillary, the apparent velocity $\mathcal{U}^{(\text{num})}$, derived from the first moment in Eq. (24), is equal to $\mathcal{U}^{(\text{sum})}$, which is the *arithmetical mean value of the grid-velocity values per cross section*. Again, that is assured either by the SNL in straight channel for any weights or by the d3Q7 BB scheme in cylindrical capillary. Using the bounce-back rule, $\mathcal{U}^{(\text{num})} = \mathcal{U}^{(\text{sum})}$ only on the coordinate velocity-weight stencil $t_c^{(a)} = \frac{1}{2}$. Otherwise, the deviation $\mathrm{err}_U^{(bb)}(t_c^{(a)},\Lambda,\mathcal{L})\mathcal{U}$ from $\mathcal{U}^{(\mathrm{sum})}$ takes place with the d2Q9 and d3Q15BB schemes:

$$t_c^{(a)} = \frac{1}{2},\quad t_d^{(a)} = 0:\ \mathcal{U}^{(\mathrm{num})} \equiv \mathcal{U}^{(\mathrm{sum})},$$
$$t_c^{(a)} \neq \frac{1}{2},\quad t_d^{(a)} \neq 0:\ \mathrm{err}_U^{(bb)}(t_c^{(a)},\Lambda,\mathcal{L}) = \frac{\mathcal{U}^{(\mathrm{num})} - \mathcal{U}^{(\mathrm{sum})}}{\mathcal{U}}. \tag{26}$$

The $\mathrm{err}_U^{(bb)}$ is linear proportional to $t_d^{(a)}$ but it is independent of the velocity amplitude and D_0. The two functional dependencies $\mathrm{err}_U^{(bb)}(t_c^{(a)},\Lambda,\mathcal{L})$ *in plug flow* and $\mathrm{err}_D(t_c^{(m)},\Lambda,\mathcal{L})$ in pure diffusion are identical by exchanging $t_c^{(a)}$ and $t_c^{(m)}$, with $\mathrm{err}_U^{(bb)}(\Lambda = \frac{1}{4}) = -\frac{1-2t_c^{(a)}}{H}$ in straight channel. Similarly with the pure diffusion correction, the dependency $\mathrm{err}_U^{(bb)}(\Lambda)$ can be measured in a given geometry prior to a series of computations with different Pe, $\mathcal{U}$, and D_0.

Dispersion. The bounce-back no-flux rule not only decreases the averaged velocity value when $t_d^{(a)} \neq 0$, but it also modifies the prescribed velocity profile. This boundary-layer velocity correction is superposed with the advective profile and the transverse velocity gradient creates the associated dispersion correction, say $\mathrm{err}_D^{(bb,U)}D$, to Taylor dispersion $k_T D_0$. In order to verify the truncation analysis in cylindrical capillary, $\mathrm{err}_D^{(bb,U)}(t_c^{(a)},\Lambda,\mathcal{L})$ will be accounted in numerical values $D^{(\mathrm{num})}$ in its approximate form [51]. Altogether, the relative correction err_D of the measured dispersion value $D^{(\mathrm{num})}$ in Eq. (24) to its Taylor value $D_0(1+k_T)$ is predicted as

$$\mathrm{err}_D = \frac{D^{(\mathrm{num})}}{D_0(1+k_T)} - 1 \approx \mathrm{err}_D^{(\mathrm{bulk})} + \mathrm{err}_D^{(bb)} + \mathrm{err}_D^{(bb,U)},$$
$$\mathrm{err}_D^{(\mathrm{bulk})} = \mathrm{err}_D^{(\mathrm{tr})} + \mathrm{err}_D^{(\mathrm{sum})}. \tag{27}$$

The truncation ($\mathrm{err}_D^{(\mathrm{tr})}$) and discretization ($\mathrm{err}_D^{(\mathrm{sum})}$) components are due to the bulk contributions, whereas the $\mathrm{err}_D^{(bb)}$ and $\mathrm{err}_D^{(bb,U)}$ are bounce-back diffusion and dispersion corrections, respectively. While the $\mathrm{err}_D^{(bb)}$ vanishes on the coordinate mass weight, the $\mathrm{err}_U^{(bb)}$ and $\mathrm{err}_D^{(bb,U)}$ both vanish on the coordinate velocity weight. It follows that in cylindrical capillary, the spurious boundary-layer effects all vanish only with the d3Q7 BB scheme.

III. STRAIGHT CHANNEL: DISPERSION, SKEWNESS, AND KURTOSIS

Section III A formulates the fourth-order-accurate apparent transport equation of the d2Q9 TRT scheme; Sec. III B derives the expression for $\mathrm{Ku}_\star^{(\mathrm{tr})}$ in pure diffusion simulations and provides the optimal solution for two relaxation functions $\Lambda^\pm$ which assures its zero value; Sec. III C extends the EMM approach to the fourth-order equation in a straight channel; Sec. III D derives $k_T^{(\mathrm{tr})}$, $\mathrm{Sk}_\star^{(\mathrm{tr})}$, and $\mathrm{Ku}_\star^{(\mathrm{tr})}$ in plug flow and provides the optimal solutions $\Lambda^\pm$ to assure their reference Gaussian zero values, then numerically validates the truncation estimate with the help of the specular-forward reflection and illustrates impact of the bounce-back diffusion boundary layer [50] due to the rotated mass weight; Sec. III E provides similar results for Poiseuille profile, takes into account the discretization effect, establishes an asymptotic behavior of the truncation corrections with the mesh resolution and Pe. Unlike in plug flow, the truncation corrections to three transport coefficients will depend on the equilibrium weights, unless for one specific Λ value. The numerical validation (Sec. III F) applies the specular-forward reflection in full weight space. The effects of the bounce-back rule for these simulations are addressed in joined work [51] where the double-Λ scheme makes the first four moments quasi-identical for both specular-forward and bounce-back reflections. The parameter guidelines and comparison with the MFTCS scheme [63] are summarized in Sec. III G.

A. Fourth-order-accurate advection-diffusion equation

We apply the d2Q9 TRT-ADE scheme (17) with the plug or parabolic advective profile $\boldsymbol{U} = U_x(y)$. In straight channel, the fourth-order pure-diffusion equation (A7) takes the form $\partial_t C = (\Lambda^-[S_2] + c_{4,1}[S_2^2] + c_{4,3}[S_4])C$, with

$$[S_2]C = c_e\big(\partial_x^2 C + \partial_y^2 C\big),\quad \big[S_2^2\big]C = c_e^2\big(\partial_x^2 C + \partial_y^2 C\big)^2,$$
$$[S_4]C = c_e\big[\partial_x^4 C + 6S_d\big(t_q^{(m)}\big)\partial_x^2\partial_y^2 C + \partial_y^4 C\big],$$
$$S_d\big(t_q^{(m)}\big) = \sum_{q:\alpha\neq\beta} t_q^{(m)} c_{q\alpha}^2 c_{q\beta}^2,$$
$$[S_4]C = c_e\big(\partial_x^2 C + \partial_y^2 C\big)^2,\quad \text{if } S_d\big(t_q^{(m)}\big) = \frac{1}{3}. \tag{28}$$

By dropping first U_x^2, U_x^3, and U_x^4 terms in third- and fourth-order corrections [they come from the anti-numerical-diffusion correction in Eq. (17)], the fourth-order-accurate equation given by Eqs. (A1)–(A6) takes the following form with the help of Eq. (28):

$$\begin{aligned}
\partial_t C + U_x(y)\partial_x C = {}& D_0\big(\partial_x^2 C + \partial_y^2 C\big) + A_1 U_x(y)\partial_x\partial_y^2 C \\
&+ A_2 U_x(y)\partial_x^3 C + A_3\partial_x^4 C \\
&+ A_4\partial_x^2\partial_y^2 C + A_0\partial_y^4 C,
\end{aligned}$$
$$D_0 = c_e\Lambda^-,\quad A_0 = A_3 = c_{4,1}c_e^2 + c_{4,3}c_e,$$
$$A_2 = c_{3,1}c_e - c_{3,2},$$
$$A_1 = c_{3,1}c_e - 3c_{3,2}S_d\big(t_q^{(a)}\big),$$
$$A_4 = 2c_{4,1}c_e^2 + 6c_{4,3}c_e S_d\big(t_q^{(m)}\big),$$
$$S_d(t_q^{(\cdot)}) = \sum_{q:\alpha\neq\beta} t_q^{(\cdot)} c_{q\alpha}^2 c_{q\beta}^2. \tag{29}$$

This tells us that the fourth-order diffusion form is isotropic only for hydrodynamic mass weight. The coefficients $c_{3,1}$, $c_{3,2}$, and $c_{4,1}$–$c_{4,4}$ are given by Eqs. (A4) and (A6), respectively. They are problem and weight independent, but they depend upon the two relaxation functions, via Λ^- and Λ. At the same time, the coefficients A_1 and A_4 are weight dependent via $c_{3,2}S_d(t_q^{(a)})$ and $c_{4,3}S_d(t_q^{(m)})$, respectively: the two functions vanish on the minimal stencil $t_c^{(a)} = t_c^{(m)} = \frac{1}{2}$. The two coefficients $c_{3,2}(\Lambda) = \Lambda - \frac{1}{12}$ and $c_{4,3} = \Lambda^-(\Lambda - \frac{1}{6})$ play then a special role because, for $\Lambda = \frac{1}{12}$ and $\frac{1}{6}$, they allow to vanish the principal dependency of the truncation corrections over the velocity weight $\{t_q^{(a)}\}$ and the mass weight

$\{t_q^{(m)}\}$, respectively. These two solutions are also known as the "optimal advection" and "optimal diffusion" solutions [35]: they vanish respectively the entire truncation coefficients of the third- and fourth-order corrections at the steady state. The U_x^2, U_x^3, and U_x^4 truncation terms can be restored by adding correction $B(U_x)$ to the right-hand side in Eq. (29):

$$\begin{aligned} B(U_x) &= (B_1 + B_2)U_x^2(y)\partial_x^4 C + (B_3 + B_4)U_x^2(y)\partial_x^2\partial_y^2 C \\ &\quad + B_5 U_x^3(y)\partial_x^3 C + B_6 U_x^4(y)\partial_x^4 C, \\ t_c^{(u)} &= \tfrac{1}{2} : B_1 = B_3 = c_{4,2}c_e, \quad B_2 = -c_{4,4}, \\ B_4 &= 3B_2 S_d(t_q^{(a)}), \quad B_5 = c_{3,2}, \quad B_6 = c_{4,4}. \end{aligned} \tag{30}$$

Note that the term of B_4 may make the truncation results slightly dependent on $\{t_q^{(a)}\}$ for $\Lambda = \frac{1}{12}$. According to the analysis [41], as Pe increases, the numerical dispersion dominates numerical diffusion. In other words, within the intermediate and high Pe range, the presence of U_x^2 (anti-numerical-diffusion) terms in Eq. (17) does not impact accuracy much. Thereby, we do not expect the terms (30) to be relevant in our study, except in plug flow where there is no numerical diffusion, in agreement with the numerical simulations below.

B. Pure diffusion: Truncation prediction for kurtosis

Theoretical prediction. When the velocity is set equal to zero, Eq. (17) becomes $e_q^+ = c_e t_q^{(m)} C$, $e_q^- \equiv 0$, $q = 1,\dots,Q_m$, $e_0 = C(1 - c_e \sum_{q=1}^{Q_m} t_q^{(m)})$, and the fourth-order-accurate pure-diffusion equation (29) reads in one dimension [see Eq. (A7) for general form]

$$\begin{aligned} \partial_t C &= D_0 \partial_x^2 C + A_3 \partial_x^4 C, \\ A_3(c_e,\Lambda^-,\Lambda) &= c_{4,1}c_e^2 + c_{4,3}c_e \\ &= c_e\Lambda^-\left(\Lambda - \tfrac{1}{6}\right) - c_e^2\Lambda^-\left[(\Lambda^-)^2 + \Lambda - \tfrac{1}{4}\right]. \end{aligned} \tag{31}$$

This equation is independent of the equilibrium weights. Notice that A_3 is not set by $D_0 = c_e\Lambda^-$ and Λ, meaning that the numerical results are expected to differ for any two different choices $\{c_e,\Lambda^-\}$ with the same D_0 because of the (transient) truncation term of $c_e^2\Lambda^-$. This correction is especially significant as $\Lambda^- \gg 1$, i.e., for very large diffusion coefficients, where $|A_3|$ increases as $c_e^2(\Lambda^-)^3$. In the absence of the truncation correction ($A_3 = 0$), one expects the initial Dirac δ function to spread with the Gaussian distribution where $\mathrm{Ku}(t) = 0$, $\mathrm{Ku}_\star \equiv 0$. However, by substituting the solution in the form $C(x,t) = \exp[i(\gamma x - \omega t)]$ into Eq. (31), its characteristic relation reads as $\omega = -i(\gamma^2 D_0 - A_3\gamma^4)$. It fits the fourth-order accurate "*s* expansion" in Eq. (5): $\omega = -i[\omega^{(2)}(i\gamma)^2 + \omega^{(4)}(i\gamma)^4]$, with

$$\omega^{(2)} = -D_0, \quad \omega^{(4)} = -A_3. \tag{32}$$

In pure diffusion, according to Eq. (11), we define the apparent solution of the scheme $\mathrm{Ku}_\star^{(\mathrm{tr})}$ as [cf. Eq. (15)]

$$\begin{aligned} \mathrm{Ku}_\star^{(\mathrm{tr})} &= \mathrm{Ku}(t)t = -\frac{6\omega^{(4)}}{(\omega^{(2)})^2} = \frac{6A_3}{D_0^2}, \\ \mathrm{Ku}_\star^{(\mathrm{tr})} &= 0 \quad \text{if} \quad \Lambda = \frac{1}{6}, \quad (\Lambda^-)^2 = \frac{1}{12}. \end{aligned} \tag{33}$$

It follows that the truncation correction creates nonzero numerical kurtosis, except for the "optimal diffusion" choice (A8): $\Lambda = \frac{1}{6}$, $(\Lambda^-)^2 = \frac{1}{12}$ where $A_3 = 0$. This constrains D_0 to the interval $]0,\sqrt{\frac{1}{12}}c_e]$, with $c_e \in]0,c_e^{(0)}(t_c^{(m)})]$. Since A_3 is mass weight independent, $\mathrm{Ku}_\star^{(\mathrm{tr})}$ is $\{t_q^{(m)}\}$ independent. Furthermore, $\mathrm{Ku}_\star^{(\mathrm{tr})}$ is independent of the space resolution and it is set by c_e, Λ^-, and Λ. The first diagram in Fig. 4 plots the predicted solution (33) for $\mathrm{Ku}_\star^{(\mathrm{tr})}$ versus Λ with four different parameter sets, where $\mathrm{Ku}_\star^{(\mathrm{tr})} = 0$ for $\Lambda = \frac{1}{6}$ with (a) and (c) configurations. This diagram illustrates that although the diffusion coefficients are equal, e.g., (a) $\{c_e,\Lambda^-\} = \{\frac{1}{3},\frac{1}{2}\sqrt{\frac{1}{3}}\}$ and (d) $\{c_e,\Lambda^-\} = \{\frac{1}{6},\sqrt{\frac{1}{3}}\}$, their apparent kurtosis coefficients $\mathrm{Ku}_\star$ differ.

Numerical validation. The second and third diagrams in Fig. 4 verify the validity of Eq. (33) in the pure-diffusion numerical simulations for the spreading of the Dirac plume with two parameter sets (a) and (d). The simulations are run in a channel of $H = \{2,4,8,20,40\}$ with the d2Q9 SNL scheme. The $D^{(\mathrm{num})}$ and $\mathrm{Ku}_\star^{(\mathrm{num})} = \mathrm{Ku}^{(\mathrm{num})}(t)t$ [Eqs. (11)] are computed with Eq. (24) and respectively compared with the D_0 and $\mathrm{Ku}_\star^{(\mathrm{tr})}$. In agreement with the expectations and results [41], $D^{(\mathrm{num})} \equiv D_0$ for any value assigned to the mass weight. Furthermore, we observe that $\mathrm{Ku}_\star^{(\mathrm{num})}$ reproduces $\mathrm{Ku}_\star^{(\mathrm{tr})}$ exactly, or quasi-exactly with the relative difference being less than 10^{-7} (which is, typically, the order of our post-processing procedure). The

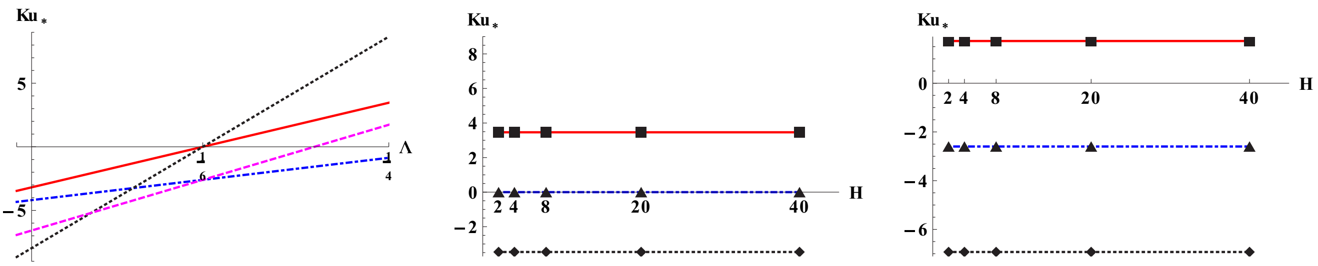

FIG. 4. Pure diffusion in straight channel. First diagram plots predicted solution (33) for $\mathrm{Ku}_\star = \mathrm{Ku}(t)t = \frac{6A_3}{D_0^2}$ versus Λ with four parameter sets $\{c_e,(\Lambda^-)^2\}$: (i) $\{\frac{1}{3},\frac{1}{12}\}$ (solid line, red), (ii) $\{\frac{1}{3},\frac{1}{3}\}$ (dotted-dashed line, blue), (iii) $\{\frac{1}{6},\frac{1}{12}\}$ (dotted line, black), and (iv) $\{\frac{1}{6},\frac{1}{3}\}$ (dashed line, magenta). This prediction is $\{t_q^{(m)}\}$ and H independent. In two next diagrams, the horizontal lines plot this prediction in cases (a) and (d) where $D_0 = \frac{1}{3}\sqrt{\frac{1}{12}}$, when $\Lambda = \{\frac{1}{12},\frac{1}{6},\frac{1}{4}\}$ [dotted line (black), dotted-dashed line (blue), solid line (red)], and compare it with the numerical results ("filled" symbols). The predicted solution is quasi-exact.

numerical results confirm that $\mathrm{Ku}_\star^{(\mathrm{num})}$ is $\{t_q^{(m)}-\}$ independent and H independent.

Summary. The apparent truncation solution for the kurtosis coefficient $\mathrm{Ku}_\star^{(\mathrm{tr})}$ in the pure-diffusion simulations is given by Eq. (33). Numerical computations with the d2Q9 SNL scheme confirm this result quasi-exactly. In a channel, the $\mathrm{Ku}_\star^{(\mathrm{tr})}$ is H and mass weight independent. The "optimal diffusion" choice $\Lambda = \frac{1}{6}$, $(\Lambda^-)^2 = \frac{1}{12}$ is the most accurate and it provides the expected pure-diffusion Gaussian solution.

Extension to the bounce-back rule. The numerical study [51] shows that replacing the specular reflection by the bounce-back rule, $D^{(\mathrm{num})}$ and $\mathrm{Ku}_\star^{(\mathrm{num})}$ are modified when the diagonal mass-weight value $t_d^{(m)}$ is different from zero. The boundary-layer diffusion correction [50] $[\mathrm{err}_D^{(bb)}(t_c^{(m)},\Lambda,\mathcal{L})$ in Eq. (25)] is then extended [51] to the fourth order providing the boundary-layer correction in kurtosis. This joined result shows that the bounce-back correction in the kurtosis remains *asymptotically constant* with the space resolution on the flat wall when $t_d^{(m)} \neq 0$. This suggests that the numerical measurements of kurtosis in the pure-diffusion simulations are especially sensitive to the effective tangential constraint of the Neumann flux schemes. However, this diffusion-coefficient dependency is expected to be negligible at high Pe range.

C. Extended method of moments

In this section, the EMM is generalized to derive the apparent solutions of the TRT scheme for k_T, $\mathrm{Sk}_\star$, and $\mathrm{Ku}_\star$ in channel-type flow $\boldsymbol{U} = U_x(y)$. After multiplication by $\mathcal{L}/\mathcal{U}$, Eq. (29) reads as, in dimensionless variables $x' = x/\mathcal{L}$, $y' = y/\mathcal{L}$, $t' = t\mathcal{U}/\mathcal{L}$,$\mathcal{U} = \langle U_x(y)\rangle$,

$$\partial_{t'}C + \tilde{U}_x(y')\partial_{x'}C = \mathrm{Pe}^{-1}\big(\partial_{x'}^2 C + \partial_{y'}^2 C\big) + a_1\tilde{U}_x(y')\partial_{x'}\partial_{y'}^2 C + a_2\tilde{U}_x(y')\partial_{x'}^3 C + a_3\mathrm{Pe}^{-1}\partial_{x'}^4 C + a_4\mathrm{Pe}^{-1}\partial_{x'}^2\partial_{y'}^2 C + a_0\mathrm{Pe}^{-1}\partial_{y'}^4 C,$$

$$\text{with}\ \ \tilde{U}_x(y') = \frac{U_x(y)}{\mathcal{U}},\quad \mathrm{Pe} = \frac{\mathcal{U}\mathcal{L}}{D_0},\quad a_1 = \frac{A_1}{\mathcal{L}^2},\quad a_2 = \frac{A_2}{\mathcal{L}^2},\quad a_3 = \frac{A_3}{D_0\mathcal{L}^2},\quad a_4 = \frac{A_4}{D_0\mathcal{L}^2},\quad a_0 = \frac{A_0}{D_0\mathcal{L}^2}. \tag{34}$$

We look for a solution of Eq. (34) in the form (12) where $\tilde{\mathcal{P}}(\omega',\boldsymbol{r}')$ becomes x' independent:

$$C(x',y',t') = \frac{1}{2\pi}\tilde{\mathcal{P}}(\omega',y')\exp[i(\gamma' x' - \omega' t')]. \tag{35}$$

Consequently, the term of $\mathrm{Pe}^{-1}\frac{\partial\tilde{\mathcal{P}}}{\partial x'}$ in Eq. (13) vanishes. Due to our extension from the second to the fourth order in Eq. (34), $\mathcal{B}^{(n)}$ in Eq. (14) is decomposed into two components:

$$\mathcal{B}^{(n)} = \mathcal{B}_1^{(n)} + \mathcal{B}_2^{(n)}, \tag{36}$$

where $\mathcal{B}_2^{(n)}$ accounts for the fourth-order correction $a_0\mathrm{Pe}^{-1}\partial_{y'}^4 C$ in Eq. (34). The normalization convention holds:

$$\langle\mathcal{B}^{(0)}\rangle = 1,\quad \langle\mathcal{B}^{(n)}\rangle \equiv 0,\quad n \geqslant 1. \tag{37}$$

After substituting Eqs. (35) and (14) into Eq. (34) and equating the terms of the same order $(i\omega')^n$, one obtains for $\mathcal{B}_1^{(n)}(y')$ and $\mathcal{B}_2^{(n)}(y')$

$$\begin{aligned}
&\partial_{y'}^2\mathcal{B}_1^{(n)}(y') = -\mathrm{Pe}\mathcal{M}^{(n)},\quad \mathcal{M}^{(n)} = M^{(n)} - \tilde{U}_x(y')\gamma'^{(n)},\quad n \geqslant 1\\
&\partial_{y'}^2\mathcal{B}_2^{(n)}(y') = -a_0\partial_{y'}^4\mathcal{B}_1^{(n)}(y'),\quad \text{then}\ \ \mathcal{B}_2^{(n)}(y') = a_0\mathrm{Pe}\mathcal{M}^{(n)} + \mathcal{C},\quad n \geqslant 1.
\end{aligned} \tag{38}$$

The integration constant $\mathcal{C}$ is dictated by the normalization condition (37). The convective term $\tilde{U}_x(y')\partial_{x'}C$ in Eq. (34) contributes to the left-hand side of Eq. (34) $\tilde{U}_x(y')\gamma'^{(n)} + \tilde{U}_x(y')\sum_{k=1}^{n-1}\gamma'^{(k)}\mathcal{B}^{(n-k)}(y')$, and the source term $M^{(n)}$ takes the following form for the first four orders of our interest:

$$\begin{aligned}
M^{(1)} &= 1,\quad M^{(2)} = [1-\gamma'^{(1)}\tilde{U}_x(y')]\mathcal{B}^{(1)} + \mathrm{Pe}^{-1}{\gamma'^{(1)}}^2\mathcal{B}^{(0)} + a_1\gamma'^{(1)}\tilde{U}_x(y')\partial_{y'}^2\mathcal{B}_1^{(1)},\\
M^{(3)} &= [1-\tilde{U}_x(y')](\gamma'^{(1)}\mathcal{B}^{(2)} + \gamma'^{(2)}\mathcal{B}^{(1)}) + \mathrm{Pe}^{-1}\big(2\gamma'^{(1)}\gamma'^{(2)}\mathcal{B}^{(0)} + {\gamma'^{(1)}}^2\mathcal{B}^{(1)}\big) + a_1\tilde{U}_x(y')\big(\gamma'^{(1)}\partial_{y'}^2\mathcal{B}_1^{(2)} + \gamma'^{(2)}\partial_{y'}^2\mathcal{B}_1^{(1)}\big)\\
&\quad + a_2\tilde{U}_x(y'){\gamma'^{(1)}}^3\mathcal{B}^{(0)} + \mathrm{Pe}^{-1}a_4{\gamma'^{(1)}}^2\partial_{y'}^2\mathcal{B}_1^{(1)},\\
M^{(4)} &= [1-\tilde{U}_x(y')](\gamma'^{(1)}\mathcal{B}^{(3)} + \gamma'^{(2)}\mathcal{B}^{(2)} + \gamma'^{(3)}\mathcal{B}^{(1)}) + \mathrm{Pe}^{-1}\big({\gamma'^{(2)}}^2\mathcal{B}^{(0)} + 2\gamma'^{(1)}\gamma'^{(3)}\mathcal{B}^{(0)} + 2\gamma'^{(1)}\gamma'^{(2)}\mathcal{B}^{(1)} + {\gamma'^{(1)}}^2\mathcal{B}^{(2)}\big)\\
&\quad + a_1\tilde{U}_x(y')\big(\gamma'^{(3)}\partial_{y'}^2\mathcal{B}_1^{(1)} + \gamma'^{(2)}\partial_{y'}^2\mathcal{B}_1^{(2)} + \gamma'^{(1)}\partial_{y'}^2\mathcal{B}_1^{(3)}\big) + a_2\tilde{U}_x(y'){\gamma'^{(1)}}^2\big(\gamma'^{(1)}\mathcal{B}^{(1)} + 3\gamma'^{(2)}\mathcal{B}^{(0)}\big)\\
&\quad + \mathrm{Pe}^{-1}\big[a_4\gamma'^{(1)}(\gamma'^{(1)}\partial_{y'}^2\mathcal{B}_1^{(2)} + 2\gamma'^{(2)}\partial_{y'}^2\mathcal{B}_1^{(1)}) + a_3{\gamma'^{(1)}}^4\mathcal{B}^{(0)}\big].
\end{aligned} \tag{39}$$

When all truncation coefficients a_n vanish $\mathcal{B}_2^{(n)} \equiv 0\ \forall\, n$, and Eqs. (38) and (39) reduce to the previous result [15] [see Eqs. (86)–(91) there for scale factor $h(r') = 1$ in straight channel].

We apply only approximate (second-order) zero-flux condition in the form $\partial_{y'}\mathcal{B}_1^{(n)}|_{y'=\pm\frac{1}{2}} = 0$ for $n \geqslant 0$. This implies the solvability condition in Eq. (38) in the form $\langle\ \mathrm{Pe}\mathcal{M}^{(n)}\rangle = 0$

and allows to find $\gamma'^{(n)}$ sequentially, starting from $M^{(1)} = 1$ in Eqs. (39):

$$\gamma'^{(n)} = \frac{\langle M^{(n)}\rangle}{\langle \tilde{U}_x(y')\rangle}, \quad n \geqslant 1 \quad \text{with} \quad \gamma'^{(1)} = \langle \tilde{U}_x(y')\rangle^{-1} = 1. \tag{40}$$

Then, $\mathcal{B}_1^{(0)}(y') = 1$, $\mathcal{B}_2^{(0)}(y') = 0$, $\mathcal{B}^{(0)}(y') = \mathcal{B}_1^{(0)} + \mathcal{B}_2^{(0)} = 1$, and the procedure develops by sequentially employing Eq. (39) for $M^{(n)}$ and Eq. (40) for $\gamma'^{(n)}$, then solving Eq. (38) for $\mathcal{B}^{(n)}$:

$$\mathcal{B}^{(n-1)} \to M^{(n)} \to \gamma'^{(n)} \to \mathcal{M}^{(n)} \to \mathcal{B}^{(n)} \ldots .$$

Using (39), the solvability conditions in Eq. (40) give

$$\begin{aligned}
\gamma'^{(2)} &= \mathrm{Pe}^{-1} - \langle \tilde{U}_x(y')\mathcal{B}^{(1)}\rangle - a_1\mathrm{Pe}\langle \tilde{U}_x(y')\mathcal{M}^{(1)}\rangle,\\
\gamma'^{(3)} &= 2\gamma'^{(2)}\mathrm{Pe}^{-1} - \langle \tilde{U}_x(y')(\mathcal{B}^{(2)} + \gamma'^{(2)}\mathcal{B}^{(1)})\rangle - a_1\mathrm{Pe}\langle \tilde{U}_x(y')(\mathcal{M}^{(2)} + \gamma'^{(2)}\mathcal{M}^{(1)})\rangle + a_2,\\
\gamma'^{(4)} &= \left(\gamma'^{(2)^2} + 2\gamma'^{(3)}\right)\mathrm{Pe}^{-1} - \langle \tilde{U}_x(y')(\mathcal{B}^{(3)} + \gamma'^{(2)}\mathcal{B}^{(2)} + \gamma'^{(3)}\mathcal{B}^{(1)})\rangle - a_1\mathrm{Pe}[\langle \tilde{U}_x(y')(\gamma'^{(3)}\mathcal{M}^{(1)} + \gamma'^{(2)}\mathcal{M}^{(2)} + \mathcal{M}^{(3)})\rangle]\\
&\quad + a_2[\langle \tilde{U}_x(y')\mathcal{B}^{(1)}\rangle + 3\gamma'^{(2)}] + a_3\mathrm{Pe}^{-1}.
\end{aligned} \tag{41}$$

The $\tilde{U}_x^2$–$\tilde{U}_x^4$ truncation terms from Eq. (30) can be included into Eqs. (39) by adding the nondimensional correction $b(U')$ to the right-hand side in Eq. (34):

$$\begin{aligned}
b(U') &= \mathrm{Pe}^{-1}\big[(b_1 + b_2)\tilde{U}_x^2\partial_{x'}^4 C + (b_3 + b_4)\tilde{U}_x^2\partial_{x'}^2\partial_{y'}^2 C\\
&\quad + b_5\tilde{U}_x^3\partial_{x'}^3 C\big] + b_6\mathrm{Pe}^{-2}\tilde{U}_x^4\partial_{x'}^4 C,\\
b_i &= \frac{\mathcal{U}^2 B_i}{D_0\mathcal{L}^2}, \quad i = 1,2,3,4, \quad b_5 = \frac{\mathcal{U}^2 B_5}{\mathcal{L}^2}, \quad b_6 = \frac{\mathcal{U}^4 B_6}{D_0\mathcal{L}^2}.
\end{aligned} \tag{42}$$

When the set $\{\gamma'^{(n)}\}$ is computed, the set $\{\omega'^{(n)} = \frac{\omega^{(n)}}{\mathcal{U}\mathcal{L}^{(n-1)}}\}$ is derived from it with Eqs. (6). This gives us $k_T^{(\mathrm{tr})}$, $\mathrm{Sk}_\star^{(\mathrm{tr})}$, and $\mathrm{Ku}_\star^{(\mathrm{tr})}$ with Eqs. (15). It follows that $k_T^{(\mathrm{tr})}$, $\mathrm{Sk}_\star^{(\mathrm{tr})}$, and $\mathrm{Ku}_\star^{(\mathrm{tr})}$ are expected to depend on the velocity weight $\{t_q^{(a)}\}$ because of the coefficient a_1 for $\gamma'^{(2)}$ in Eq. (41). When $b(U')$ is omitted, the dependency on the velocity weight vanishes for $\Lambda = \frac{1}{12}$. The dependency on the mass weight $\{t_q^{(m)}\}$ is only expected for $\mathrm{Ku}_\star$ via a_4 in expression of $M^{(3)}$ in Eqs. (39). The constructed solution for plug and parabolic flows is presented in the two next sections.

D. Constant velocity field

Theoretical prediction. The Taylor dispersion is absent in the plug flow and, therefore, starting from the ADE, the EMM would prescribe the Gaussian solution with zero k_T, Sk, and Ku. Let us examine the truncation result for these coefficients. When $U_x = \text{const}$, then $\tilde{U}_x(y') \equiv 1$ and the correction $b(U')$ from Eq. (42) is easy to include into Eqs. (39)–(41): replace a_2 by $a_2 + b_5$ and a_3 by $a_3 + b_1 + b_2 + b_6$. Then, Eqs. (38) and (41) give

$$\begin{aligned}
&\mathcal{B}^{(n)} = \mathcal{M}^{(n)} = 0, \quad \gamma'^{(n)} = M^{(n)}, \quad \text{with } \gamma'^{(1)} = 1, \quad \gamma'^{(2)}\mathrm{Pe} = 1,\\
&\gamma'^{(3)}\mathrm{Pe}^2 = 2 + (a_2 + b_5)\mathrm{Pe}^2, \quad \gamma'^{(4)}\mathrm{Pe}^3 = 5 + [5(a_2 + b_5) + (a_3 + b_1 + b_2 + b_6)]\mathrm{Pe}^2.
\end{aligned} \tag{43}$$

When the truncation coefficients vanish, this solution reduces to the Gaussian solution [15] $\gamma'^{(n)} = \{1,\mathrm{Pe}^{-1},2\mathrm{Pe}^{-2},5\mathrm{Pe}^{-3}\}$ where $k_T = \mathrm{Sk}_\star = \mathrm{Ku}_\star = 0$. We compute $\omega'^{(n)}$ from $\gamma'^{(n)}$ with Eqs. (6), and finally $k_T^{(\mathrm{tr})}$, $\mathrm{Sk}_\star^{(\mathrm{tr})}$, and $\mathrm{Ku}_\star^{(\mathrm{tr})}$ with Eqs. (15):

$$\begin{aligned}
&\{\omega'^{(n)}\} = \left\{\frac{\omega^{(n)}}{\mathcal{U}L^{n-1}}\right\} = \{1, -\mathrm{Pe}^{-1}, -(a_2 + b_5), -(a_3 + b_1 + b_2 + b_6)\mathrm{Pe}^{-1}\}, \quad n = 1,2,3,4\\
&\mathcal{U}^{(\mathrm{num})} = \mathcal{U}, \quad k_T^{(\mathrm{tr})} = 0, \quad \mathrm{Sk}_\star^{(\mathrm{tr})} = \frac{-3(a_2 + b_5)Pe^{3/2}}{\sqrt{2}}, \quad \mathrm{Ku}_\star^{(\mathrm{tr})} = 6(a_3 + b_1 + b_2 + b_6)\mathrm{Pe}.
\end{aligned} \tag{44}$$

As could be expected, the third- and fourth-order truncation corrections do not modify either the mean velocity or the zero-valued dispersivity in plug flow. However, they prescribe nonzero values for $\mathrm{Sk}_\star^{(\mathrm{tr})}$ and $\mathrm{Ku}_\star^{(\mathrm{tr})}$. Since $\mathrm{Sk}_\star^{(\mathrm{tr})}$ and $\mathrm{Ku}_\star^{(\mathrm{tr})}$ do not depend upon a_1, a_4, and b_4, they are independent from equilibrium weights. The Gaussian solution $\mathrm{Sk}_\star^{(\mathrm{tr})} = 0$ is only assured when $a_2 = b_5 = 0$ on the "optimal-advection" solution (A5): $\Lambda^- = \Lambda^+ = \sqrt{\frac{1}{12}}$. Whereas in contrast, when the velocity is small and the b terms can be neglected, $\mathrm{Ku}_\star^{(\mathrm{tr})} \approx 0$ on the "optimal-diffusion" solution (A8) where $a_3 = 0$, similarly to the pure-diffusion solution (33). The result (44) formally applies for pure diffusion with $\mathrm{Sk}_\star^{(\mathrm{tr})} \equiv 0$, $\mathrm{Ku}(t) = \mathrm{Ku}_\star^{(\mathrm{tr})}\frac{H}{U}t^{-1} = 6a_3\mathrm{Pe}\frac{H}{U}t^{-1} = 6\frac{A_3\mathrm{Pe}}{D_0H^2}\frac{H}{U}t^{-1} = 6\frac{A_3}{D_0^2}t^{-1}$. This result coincides with Eq. (33).

Numerical validation. As has been reported [41,50], the d2Q9 SNL produces the exact solution in plug flow: $\mathcal{U}^{(\mathrm{num})} = \mathcal{U}$ and $D^{(\mathrm{num})} = D_0$. Table III shows a very good agreement between the numerical results and prediction (44) for $\mathrm{Sk}_\star$ and $\mathrm{Ku}_\star$. The computations are run with the d2Q9 SNL in straight channel of width $H = 20$, with $(\Lambda^-)^2 = \frac{1}{12}$, $c_e|_{\mathrm{Pe}\approx 9.5} = \frac{1}{3}$, and $c_e|_{\mathrm{Pe}\approx 95} = \frac{1}{30}$.

TABLE III. This table shows the relative differences of the numerical values computed with the d2Q9 SNL for $D^{(\mathrm{num})}$, $\mathrm{Sk}_\star^{(\mathrm{num})}$, and $\mathrm{Ku}_\star^{(\mathrm{num})}$ to their prediction in Eq. (44) for plug flow in straight channel.

Expt. I, Pe $\approx$ 9.5				Expt. IV, Pe $\approx$ 95			
Λ	err_D (%)	err(Sk) (%)	err(Ku) (%)	Λ	err_D (%)	err(Sk) (%)	err(Ku) (%)
$\frac{1}{12}$	1.4×10^{-7}	*Na*	1.93×10^{-3}	$\frac{1}{12}$	1.4×10^{-7}	*Na*	1.93×10^{-3}
$\frac{1}{6}$	1.4×10^{-7}	2.85×10^{-4}	3.49×10^{-1}	$\frac{1}{6}$	1.4×10^{-7}	3.41×10^{-5}	-7.04×10^{-1}
$\frac{1}{4}$	1.4×10^{-7}	-6.56×10^{-4}	-1.24×10^{-3}	$\frac{1}{4}$	1.4×10^{-7}	-4.17×10^{-4}	-3.02×10^{-2}

The EMM truncation predictions are $D^{(\mathrm{num})} = D_0$, $\mathrm{Sk}_\star^{(\mathrm{tr})}|_{\mathrm{Pe}\approx 9.5} \approx -0.18 + 2.16\Lambda$, $\mathrm{Ku}_\star^{(\mathrm{tr})}|_{\mathrm{Pe}\approx 9.5} = -6.89 + (41.7 - 3.1\Lambda)\Lambda$, and $\mathrm{Sk}_\star^{(\mathrm{tr})}|_{\mathrm{Pe}\approx 95} = -8.2454 + 98.9448\Lambda$, $\mathrm{Ku}_\star^{(\mathrm{tr})}|_{\mathrm{Pe}\approx 95} = -91.28 + (639.05 - 451.1\Lambda)\Lambda$, with $\mathrm{Sk}_\star^{(\mathrm{tr})}|_{\Lambda=\frac{1}{12}} = 0$, $\mathrm{Sk}_\star^{(\mathrm{num})}|_{\Lambda=\frac{1}{12}} = -4.24 \times 10^{-8}$ for Pe $\approx$ 9.5, and $\mathrm{Sk}_\star^{(\mathrm{num})}|_{\Lambda=\frac{1}{12}} = 1.4 \times 10^{-7}$ for Pe $\approx$ 95. In these simulations, the truncation results noticeably improve their accuracy by including truncation terms (30) because high-order numerical diffusion becomes important for them in the absence of the numerical dispersion. In agreement with Eq. (44), the numerical results confirm that the d2Q9 SNL produces weight-independent solutions for $\mathrm{Sk}_\star^{(\mathrm{num})}$ and $\mathrm{Ku}_\star^{(\mathrm{num})}$ in plug flow. These solutions are therefore the same as with the d2Q5 BB scheme.

Impact of the diffusion boundary layer. To illustrate the difference between the SNL and BB rules, Table IV reports results of similar simulations with the d2Q9 BB scheme. Namely, it displays the worst-possible scenario for diffusion boundary layer, due to the "rotated" mass weight: $\{t_c^{(m)} = 0, t_d^{(m)} = \frac{1}{4}\}$. The results confirm that $\mathrm{err}_D = \mathrm{err}_D^{(bb)}(t_c^{(m)})$ where the bounce-back correction $\mathrm{err}_D^{(bb)}(t_c^{(m)})$ is exactly specified by Eq. (19) from work [41]: it varies from $\approx 3\%$ to 5% from $\Lambda = \frac{1}{12}$ to $\frac{1}{4}$. Since $(\Lambda^-)^2 = \frac{1}{12}$, we deal with the "optimal advection" choice (A5), when $\Lambda = \frac{1}{12}\mathrm{Sk}_\star^{(\mathrm{tr})} = 0$. Using the bounce back, the numerical results give relatively small values, as $\mathrm{Sk}_\star^{(\mathrm{num})} = -1.72 \times 10^{-2}$ for Pe $\approx$ 9.5 and $\mathrm{Sk}_\star^{(\mathrm{num})} = -5.44 \times 10^{-3}$ for Pe $\approx$ 95. That means the skewness is only slightly affected by the diffusion boundary layer when $\Lambda = \frac{1}{12}$. At the same time, we observe a large discrepancy with the truncation prediction for $\mathrm{Sk}_\star^{(\mathrm{num})}$ when $\Lambda \neq \frac{1}{12}$ and, especially, for $\mathrm{Ku}_\star^{(\mathrm{num})}$, $\forall\ \Lambda$. In particular, when $\Lambda = \frac{1}{6}$, $\mathrm{Ku}_\star^{(\mathrm{tr})} = -0.02$, $\mathrm{Ku}_\star^{(\mathrm{num})} = 3.95$ for Pe $\approx$ 9.5, while $\mathrm{Ku}_\star^{(\mathrm{tr})} = 2.7$, $\mathrm{Ku}_\star^{(\mathrm{num})} = 43.15$ for Pe $\approx$ 95. Thereby, these results show that except for $\mathrm{Sk}_\star$ with $\Lambda = \frac{1}{12}$, the boundary-layer diffusion correction due to the diagonal mass weight modifies not only diffusion coefficients, but, in much larger extent, the measured skewness and kurtosis.

Summary. The numerical simulations with the d2Q9 SNL entirely confirm the EMM truncation predictions relative to the weight-independent coefficients $\mathrm{Sk}_\star$ and $\mathrm{Ku}_\star$ in plug flow. The "optimal advection" choice (A5) yields the expected physical solution $\mathrm{Sk}_\star = 0$, while $\mathrm{Ku}_\star = 0$ is approached with the "optimal diffusion" choice (A8), provided that velocity amplitude is small. Yet, the bounce back with zero-valued mass-weight value $t_c^{(a)} = 0$ ("rotated" coordinate stencil) produces relatively large numerical corrections to truncation result in both skewness and kurtosis. Finally, we note that the d2Q9 BB with the nonzero diagonal velocity weight was not considered here because of its huge retardation effect demonstrated [50] in plug flow.

E. Poiseuille profile: Predictions

In straight Poiseuille flow with mean velocity $\mathcal{U} = \langle U_x(y)\rangle$, $U'(y) = U_x(y) - \mathcal{U}$, the dimensionless dispersivity $k_T^{(s)}$ in Eq. (2) is derived with the Taylor ansatz [4]:

$$k_T^{(s)} = -\frac{\langle U'(y)\alpha(y)\rangle}{D_0^2} = \frac{\mathrm{Pe}^2}{210}, \quad \alpha(y) = \int_{-H/2}^{y}\left[\int_{-H/2}^{y} U'(y')dy'\right]dy', \quad \langle U'(y)\rangle = 0, \quad \mathrm{Pe} = \frac{\mathcal{U}H}{D_0}. \tag{45}$$

Numerically, this solution is modified by the quantity $\delta k_T^{(\mathrm{tr})}$ derived [41] with the Taylor ansatz from the third- and fourth-order truncation corrections $A_1 U_x(y)\partial_x\partial_y^2 C$ and $A_0\partial_y^4 C$. The apparent dispersivity $k_T^{(\mathrm{tr})}$ of d2Q9 scheme reads as

$$k_T^{(\mathrm{tr})} \approx k_T^{(s)} + \delta k_T^{(\mathrm{tr})}, \quad \delta k_T^{(\mathrm{tr})} = K k_T^{(1,s)}, \quad K = \left(A_1 + \frac{A_0}{D_0}\right) = \left[c_e(\Lambda^-)^2 + \Lambda - \frac{1}{6}\right] - 3S_d\left(t_q^{(a)}\right)\left(\Lambda - \frac{1}{12}\right),$$

$$k_T^{(1,s)} = \frac{\langle U'(y)U_x(y)\rangle}{D_0^2} = \frac{\langle U'^2\rangle}{D_0^2} = \frac{\mathrm{Pe}^2}{5H^2}, \quad S_d\left(t_q^{(a)}\right) = \sum_{q:\alpha\neq\beta} t_q^{(a)} c_{q\alpha}^2 c_{q\beta}^2, \tag{46}$$

$$\delta k_T^{(\mathrm{tr})}|_{c_e(\Lambda^-)^2\to 0} = 0 \text{ if } \Lambda = \frac{1-6t_c^{(a)}}{24\left(1-3t_c^{(a)}\right)} \text{ if } t_c^{(a)} \in \left[0,\frac{1}{6}\right[\text{ or } t_c^{(a)} \in \left]\frac{1}{3},\frac{1}{2}\right], \quad \text{then } \Lambda\left(t_c^{(a)} = \frac{1}{2}\right) = \frac{1}{6}. \tag{47}$$

This result further confirms that the truncation errors to the transport coefficients are not set by Pe and Λ alone. This deficiency is the most pronounced at large values of Λ^-. When Pe increases $[c_e(\Lambda^-)^2 \to 0]$, $\delta k_T^{(\mathrm{tr})}$ is set by Λ and the velocity weight $t_c^{(a)}$. The optimal parameter space where $\delta k_T^{(\mathrm{tr})}$ vanishes via $\Lambda(t_c)$ is then given by Eq. (47) [we apply here $S_d(t_q^{(a)}) = 1 - 2t_c^{(a)}$ in d2Q9

TABLE IV. This table illustrates the effect of the diffusion boundary layer due to the "rotated" mass weight: $\{t_c^{(m)},t_d^{(m)}\} = \{0,\frac{1}{4}\}$ in d2Q9 BB, to be compared with the d2Q9 SNL results in Table III. The third and eighth columns: the relative diffusion-coefficient correction err_D coincides with the predicted value [50] for $\mathrm{err}_D^{(bb)}$ [cf. Eq. (25)].

Expt. I, Pe ≈ 9.5					Expt. IV, Pe ≈ 95				
Λ	err_D (%)	$\mathrm{err}_D - \mathrm{err}_D^{(bb)}$ (%)	err(Sk) (%)	err(Ku) (%)	Λ	err_D (%)	$\mathrm{err}_D - \mathrm{err}_D^{(bb)}$ (%)	err(Sk) (%)	err(Ku) (%)
$\frac{1}{12}$	−2.89	1.53×10^{-7}	*Na*	-7.75×10^{1}	$\frac{1}{12}$	−2.89	-9.33×10^{-8}	*Na*	-7.75×10^{1}
$\frac{1}{6}$	−4.08	1.53×10^{-7}	7.	-1.83×10^{4}	$\frac{1}{6}$	−4.08	1.53×10^{-7}	6.49	1.5×10^{3}
$\frac{1}{4}$	−5.	1.09×10^{-5}	1.07×10^{1}	1.55×10^{2}	$\frac{1}{4}$	−5.	1.09×10^{-5}	8.18	1.26×10^{2}

and d3Q15]. This solution is not defined for the most interesting stability interval $t_c^{(a)} \in [\frac{1}{6},\frac{1}{3}]$ [43,44]. On the coordinate velocity stencil $t_c^{(a)} = \frac{1}{2}$, the most accurate choice is $\Lambda = \frac{1}{6}$.

Now, let us derive $\delta k_T^{(\mathrm{tr})}$, $\mathrm{Sk}_\star^{(\mathrm{tr})}$, and $\mathrm{Ku}_\star^{(\mathrm{tr})}$ with the EMM method. Solution for $\{\gamma'^{(n)}\}$ from Eq. (41) reads as (with $\mathcal{L} = H$)

$$\begin{aligned}
\gamma'^{(2)}\mathrm{Pe} &= 1 + \frac{\mathrm{Pe}^2}{210}[1 + 42(a_1 + a_0)],\\
\gamma'^{(3)}\mathrm{Pe}^2 &= 2 + \mathrm{Pe}^2\left[\frac{2}{105} + \frac{4}{5}(a_1 + a_0) + a_2\right] + \mathrm{Pe}^4\left[\frac{29}{485100} + \frac{(a_1/6) - 11a_1^2 + a_0 + 13a_1a_0 + 24a_0^2}{175}\right],\\
\gamma'^{(4)}\mathrm{Pe}^3 &= 5 + \mathrm{Pe}^2\left[\frac{1}{14} + 3(a_1 + a_0) + 5a_2 + a_3\right] + \mathrm{Pe}^4\Bigg[\frac{20 + 462a_0(4 + 93a_0 + 63a_2 - 21a_4) + 693a_2 - 231a_4}{48510}\\
&\quad + \frac{a_1}{70}(1 + 54a_0 + 56a_2 - 14a_4) - \frac{4a_1^2}{35}\Bigg] + \mathrm{Pe}^6\Bigg\{\frac{97 + 7a_0[2797 + 42120a_0(4 + 77a_0)]}{220720500}\\
&\quad + a_1\left[-\frac{139}{4504500} + \frac{2a_0(-5 + 231a_0)}{13475}\right] - {a_1}^2\left(\frac{107}{80850} + \frac{a_0}{25}\right) + \frac{{a_1}^3}{35}\Bigg\},\\
\mathrm{Pe} &= \frac{\mathcal{U}H}{D_0}.
\end{aligned} \tag{48}$$

We compute $\{\omega'^{(n)}\}$ from $\{\gamma'^{(n)}\}$ with Eqs. (6), and finally $k_T^{(\mathrm{tr})}$, $\mathrm{Sk}_\star^{(\mathrm{tr})}$, and $\mathrm{Ku}_\star^{(\mathrm{tr})}$ with Eqs. (15). Namely, $\gamma'^{(2)}$ predicts $k_T^{(\mathrm{tr})}$ with the help of Eq. (11) as

$$k_T^{(\mathrm{tr})} = \mathrm{Pe}\gamma'^{(2)} - 1 = k_T^{(s)} + \delta k_T^{(\mathrm{tr})}, \quad \delta k_T^{(\mathrm{tr})} = \frac{(a_1 + a_0)\mathrm{Pe}^2}{5} = \frac{(A_1 + \frac{A_0}{D_0})\mathrm{Pe}^2}{5H^2}. \tag{49}$$

This solution coincides with the truncation result [41] recalled by Eq. (46). Therefore, the Taylor-type analysis [41] of truncation corrections and the EMM agree for apparent correction $\delta k_T^{(\mathrm{tr})}$ to predicted coefficient $k_T^{(s)}$.

Thus, $\gamma'^{(2)}$ (and then $k_T^{(\mathrm{tr})}$) depend on $\{a_0,a_1\}$; $\gamma'^{(3)}$ (and then $\mathrm{Sk}_\star^{(\mathrm{tr})}$) depend on $\{a_0,a_1,a_2\}$; $\gamma'^{(4)}$ (and then $\mathrm{Ku}_\star^{(\mathrm{tr})}$) depend upon all truncation coefficients $a_0 - a_4$. The following observations are interesting. First, $k_T^{(\mathrm{tr})}$, $\mathrm{Sk}_\star^{(\mathrm{tr})}$, and $\mathrm{Ku}_\star^{(\mathrm{tr})}$ depend on the velocity weight $\{t_q^{(a)}\}\ \forall\ \Lambda$, except for $\Lambda = \frac{1}{12}$ where $c_{3,2} = 0$. Second, $\mathrm{Ku}_\star^{(\mathrm{tr})}$ depends on the mass weight $\{t_q^{(m)}\}$ via a_4, except for $\Lambda = \frac{1}{6}$. Third, when $\Lambda^- \to 0$, $k_T^{(\mathrm{tr})}$ dependency on c_e vanishes, and this is valid for $\mathrm{Sk}_\star^{(\mathrm{tr})}$ and $\mathrm{Ku}_\star^{(\mathrm{tr})}$ only when $\Lambda = \frac{1}{4}$. Fourth, when $c_e \to 0$, dependency on Λ^- vanishes in three transport coefficients.

Alike for k_T, expansion of err(Sk) and err(Ku) into series shows their second-order decrease with H^{-2}. In the limit $\Lambda^- \to 0$, we get

$$\begin{aligned}
\mathrm{err(Sk)}|_{\Lambda^-\to 0} \approx{}& \frac{H^{-2}}{4\mathrm{Pe}^2(210 + \mathrm{Pe}^2)}[-330c_e(-1 + 4\Lambda)(-44100 + \mathrm{Pe}^4) - 9240(-525 + 6300\Lambda + 4\mathrm{Pe}^2)\\
&+ \mathrm{Pe}^2(332640\Lambda - 307\mathrm{Pe}^2 + 3408\Lambda\mathrm{Pe}^2) - 18\mathrm{Pe}^2(-1 + 12\Lambda)t_c^{(a)}(4620 + 29\mathrm{Pe}^2)],
\end{aligned} \tag{50}$$

$$\mathrm{err(Sk)}|_{\Lambda^-\to 0,\mathrm{Pe}\to\infty} \approx \frac{H^{-2}}{4}[-307 + 330c_e(1 - 4\Lambda) + 3408\Lambda] + \frac{261H^{-2}}{2}(1 - 12\Lambda)t_c^{(a)}, \tag{51}$$

$$\mathrm{err(Sk)}|_{\Lambda^-\to 0,c_e\to 0} \approx 0 \quad \text{if} \quad \Lambda = \frac{1}{6} - \frac{87(2t_c^{(a)} - 1)}{8(261t_c^{(a)} - 142)}\ \forall\ t_c^{(a)} \in \left[0,\frac{1}{2}\right], \quad \Lambda\left(t_c^{(a)} = \frac{1}{2}\right) = \frac{1}{6}, \quad \Lambda\left(t_c^{(a)} = \frac{1}{3}\right) \approx \frac{1}{10} \tag{52}$$

and, for Ku

$$\begin{aligned}\mathrm{err(Ku)}|_{\Lambda^-\to 0} \approx{}& \frac{H^{-2}}{56\mathrm{Pe}^4(210+\mathrm{Pe}^2)}[195c_e(-1+4\Lambda)(161700+\mathrm{Pe}^4)(210+\mathrm{Pe}^2) - 441441\times 10^4(-1+6\Lambda)\\ &-280(1333+573\Lambda)\mathrm{Pe}^4 + 2(107-1398\Lambda)\mathrm{Pe}^6 + 42042000(-2+9\Lambda)\mathrm{Pe}^2]\\ &+\frac{9H^{-2}(-1+12\Lambda)t_c^{(a)}(1190+\mathrm{Pe}^2)}{(210+\mathrm{Pe}^2)} - \frac{21450H^{-2}(-1+6\Lambda)t_c^{(m)}}{\mathrm{Pe}^2},\end{aligned} \tag{53}$$

$$\mathrm{err(Ku)}|_{\Lambda^-\to 0,\mathrm{Pe}\to\infty} \approx \frac{H^{-2}}{56}[214-2796\Lambda+195c_e(-1+4\Lambda)] + 9H^{-2}(-1+12\Lambda)t_c^{(a)}, \tag{54}$$

$$\mathrm{err(Ku)}|_{\Lambda^-\to 0,c_e\to 0} \approx 0 \quad \text{if} \quad \Lambda = \frac{1}{6} - \frac{21(2t_c^{(a)}-1)}{(504t_c^{(a)}-233)}, \quad t_c^{(a)} \in \left]\frac{107}{252},\frac{1}{2}\right], \quad \text{then} \quad \Lambda\left(t_c^{(a)}=\frac{1}{2}\right) = \frac{1}{6}. \tag{55}$$

Equations (50) and (53) allow to observe easily the aforementioned properties: (i) velocity-weight dependency vanishes for $\Lambda = \frac{1}{12}$, (ii) the dependency on c_e vanishes for $\Lambda = \frac{1}{4}$, and (iii) the mass-weight dependency in err(Ku) vanishes when $\Lambda = \frac{1}{6}$. Therefore, only when Λ^- and c_e are sufficiently small, the truncation errors become controlled by Pe independently of the diffusion coefficient; $\Lambda = \frac{1}{4}$ improves for this property. Further, Eqs. (51) and (54) show that in the limit $\mathrm{Pe}\to\infty$, err(Sk) and err(Ku) become asymptotically Pe independent, and the err(Ku) dependency on $t_c^{(m)}$ vanishes. The asymptotic relations (51) and (54) can be used for the parameter optimization at sufficiently small Λ^-. We exemplify two solutions for $\Lambda(t_c^{(a)})$ given by Eqs. (52) and (55) where err(Sk) and err(Ku), respectively, vanish in the limit $\Lambda^-\to 0$, $c_e\to 0$. Unlike for k_T and Ku, $\Lambda(t_c^{(a)})$ in Eq. (52) is defined for any weight value and $\Lambda(t_c^{(a)}=\frac{1}{3})\approx 10^{-1}$. The err(Ku) vanishes with $\Lambda(t_c^{(a)})$ in Eq. (55) only in very narrow weight interval, when $t_c^{(a)}\approx\frac{1}{2}$. Remarkably, the optimal solution $\Lambda = \frac{1}{6}$ is valid on the coordinate stencil $t_c^{(a)} = \frac{1}{2}$ for all three transport coefficients [cf. Eqs. (47), (52), and (55)]. This choice provides the most accurate solutions for the three transport coefficients in the limit of high Pe with the d2Q5 and d3Q7 schemes.

Figure 5 illustrates the relative differences err(Sk) and err(Ku) in Eq. (23). They are estimated on the predicted solution (48) for $\mathrm{Sk}_\star^{(\mathrm{tr})}$ and $\mathrm{Ku}_\star^{(\mathrm{tr})}$ in the limit $c_e\to 0$. The predictions are displayed versus Pe for $H = 20$ (the two first diagrams in row) and versus H for $\mathrm{Pe} = 10^2$ (the two last diagrams in row). The two weight families are addressed for the "coordinate" $t_c^{(a)} = t_c^{(m)} = \frac{1}{2}$ in the top row and for the "hydrodynamic" $t_c^{(a)} = t_c^{(m)} = \frac{1}{3}$ in the bottom row. Since $\mathrm{Sk}_\star^{(\mathrm{tr})}$ is mass weight independent, the difference for err(Sk) at the top and bottom rows is uniquely due to the velocity weight $t_c^{(a)}$; when $\Lambda = \frac{1}{12}$, the err(Sk) is the same for $t_c^{(a)} = \frac{1}{2}$ (top) and $t_c^{(a)} = \frac{1}{3}$ (bottom). The results show that, alike the dispersion correction err_D, the err(Sk) and err(Ku) both become Pe independent as $\mathrm{Pe} \geqslant {\approx}10^2$ (two first diagrams in row). Even with the relatively fine resolution of $H = 20$, err(Sk) still noticeably depends on Λ. A very rapid increase of the amplitude in err(Sk) and err(Ku) occurs when Pe decreases to zero. Notice, on the one hand, the assumption $c_e\to 0$ does not apply in this limit. On the other hand, a large increase in err(Sk) and err(Ku) for small Pe will be detected systematically because the reference values are very small. The two last diagrams in Fig. 5 allow for examination of the resolution dependency in err(Sk) and err(Ku) at $\mathrm{Pe} = 10^2$ (and, hence, for higher Pe). These predictions tell us that the coordinate velocity weight $t_c^{(a)} = \frac{1}{2}$ (the top row) gains one order magnitude in accuracy on coarse grids against the "hydrodynamic" weight $t_c^{(a)} = \frac{1}{3}$ (bottom row) when $\Lambda \in [\frac{1}{6},\frac{1}{4}]$. The "optimal diffusion" choice $\Lambda = \frac{1}{6}$ is clearly the most accurate when $t_c^{(a)} = \frac{1}{2}$ for all H, alike err_D with Eq. (46). The $\Lambda = \frac{1}{12}$ is the most accurate for skewness and kurtosis on the hydrodynamic stencil (bottom row), especially, when H is small, but err(Ku) remains negative in the whole interval $\Lambda \in [\frac{1}{12},\frac{1}{4}]$. These observations agree with the predicted solution for err(Sk): $\Lambda(t_c^{(a)} = \frac{1}{3}) \approx \frac{1}{10}$ in Eqs. (52), and with Eq. (55), because there is no positive root for $\mathrm{err(Ku)} = 0$ with $t_c^{(a)} = \frac{1}{3}$. The optimal numerical choice might be also guided by isotropy and stability arguments, which are more favorable for the diagonal velocity stencil on the one hand, and for $\Lambda = \frac{1}{4}$ on the other [35,43,44]. However, this combination requires finer grids to achieve the same level of accuracy as with $\Lambda = \frac{1}{6}$ and $t_c^{(a)} = \frac{1}{2}$, or with $\Lambda = \frac{1}{12}$ and $t_c^{(a)} = \frac{1}{3}$, unless the summation effect further modifies these predictions.

Summation effect. It has been recognized [41] that the exact (or quasi-exact) agreement for $k_T^{(\mathrm{tr})}$ with the numerical measurements requires to account for the summation errors. Principally, starting from the first moment, $\mathcal{U}$ should be replaced in the predicted moments by $\mathcal{U}^{(\mathrm{sum})}$:

$$\mathcal{U}^{(\mathrm{sum})} = \frac{1}{H}\sum_{i=1}^{H} U_x(y_i) = \mathcal{U}\left(1+\frac{1}{2H^2}\right). \tag{56}$$

We find that the EMM is able to account for the summation errors *automatically*. This is achieved by replacing $\mathcal{U}$ via $\mathcal{U}^{(\mathrm{sum})}$ for all terms in Eq. (34), meaning that $\tilde{U}_x(y')$ is set equal to $U_x(y)/\mathcal{U}^{(\mathrm{sum})}$ and $\mathrm{Pe}\to\mathrm{Pe}^{(\mathrm{sum})} = \frac{\mathcal{U}^{(\mathrm{sum})}H}{D_0}$. Accordingly, the averaged values are all computed with the summation of the grid values, namely, for $\langle M^{(n)}\rangle$ in Eq. (40). Such summation procedure modifies $k_T^{(\mathrm{tr})}$ from Eq. (49) to $k_T^{(\mathrm{tr,sum})}$:

$$\begin{aligned}k_T^{(\mathrm{tr,sum})} &= \gamma'^{(2)(\mathrm{sum})}\mathrm{Pe}^{(\mathrm{sum})} - 1\\ &= \left(\frac{H^2}{42}+\frac{1}{28}+A_1+\frac{A_0}{D_0}\right)k_T^{(1,\mathrm{sum})},\end{aligned}$$

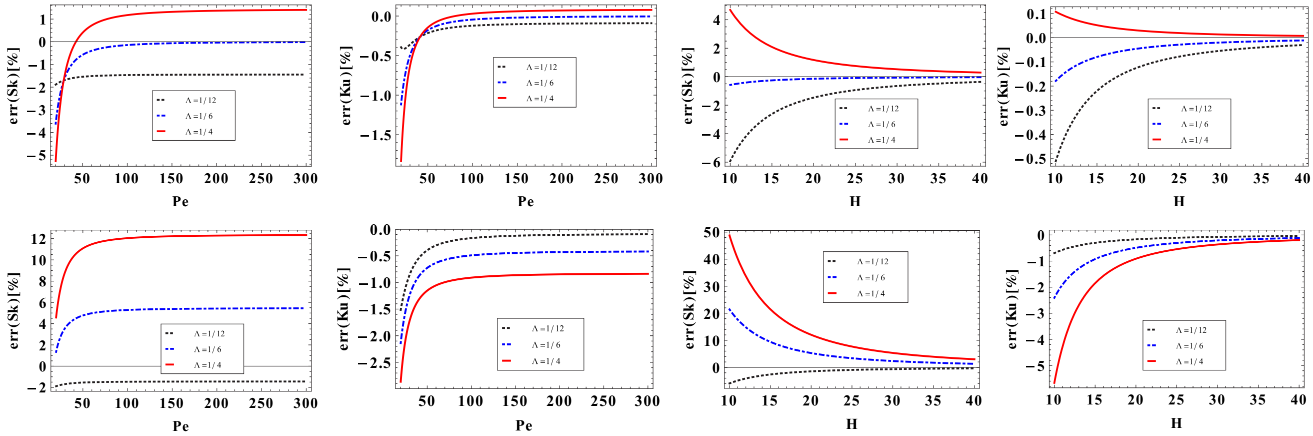

FIG. 5. Poiseuille flow in straight channel by d2Q9 scheme. This figure displays the predicted differences in Eq. (23) for truncation result $\mathrm{Sk}_\star^{(\mathrm{tr})}$ and $\mathrm{Ku}_\star^{(\mathrm{tr})}$ relative to the physical values $\mathrm{Sk}_\star$ and $\mathrm{Ku}_\star$ from Table I. This prediction is derived with Eqs. (48) and it is plotted in the limit $c_e \to 0$ for $\Lambda = \{\frac{1}{12}, \frac{1}{6}, \frac{1}{4}\}$ [dotted line (black), dotted-dashed line (blue), solid line (red)]. Top row: $t_c^{(a)} = t_c^{(m)} = \frac{1}{2}$. Bottom row: $t_c^{(a)} = t_c^{(m)} = \frac{1}{3}$. The two first diagrams are plotted for $H = 20$, when $\mathrm{Pe} \in [20, 3 \times 10^2]$. The two last diagrams are displayed for $\mathrm{Pe} = 10^2$, when $H \in [10,40]$.

$$\mathrm{Pe}^{(\mathrm{sum})} = \mathrm{Pe}\left(1 + \frac{1}{2H^2}\right),$$

$$k_T^{(1,\mathrm{sum})} = \frac{\mathrm{Pe}^2}{5H^2}\left(1 - \frac{5}{H^2} + \frac{4}{H^4}\right),$$

$$k_T^{(1,\mathrm{sum})}|_{H\to\infty} = \frac{\mathrm{Pe}^2}{5H^2}, \quad k_T^{(\mathrm{tr},\mathrm{sum})}|_{H\to\infty} \to k_T^{(s)} = \frac{\mathrm{Pe}^2}{210}. \tag{57}$$

This result coincides with the truncation-summation estimate [41] [see Eqs. (72)–(76) there] if we write $k_T^{(\mathrm{tr},\mathrm{sum})}$ as

$$k_T^{(\mathrm{tr},\mathrm{sum})} = k_T^{(s)} + \delta k_T^{(\mathrm{tr},\mathrm{sum})},$$

$$\delta k_T^{(\mathrm{tr},\mathrm{sum})} = K^{\mathrm{sum}} k_T^{(1,\mathrm{sum})} + \frac{(20 - 21H^2)\mathrm{Pe}^2}{210H^6},$$

$$K^{\mathrm{sum}} = \left(A_1 + \frac{A_0}{D_0} - \frac{1}{12}\right)$$

$$= c_e(\Lambda^-)^2 + \Lambda - \frac{1}{4} - 3\left(1 - 2t_c^{(a)}\right)\left(\Lambda - \frac{1}{12}\right). \tag{58}$$

Therefore, the bulk dispersion error in Eq. (27) reads as

$$\mathrm{err}_D^{(\mathrm{bulk})} = \mathrm{err}_D^{(\mathrm{tr})} + \mathrm{err}_D^{(\mathrm{sum})} = \frac{\delta k_T^{(\mathrm{tr},\mathrm{sum})}}{1 + k_T^{(s)}}. \tag{59}$$

Notice that as Pe increases, $\mathrm{err}_D^{(\mathrm{bulk})} \approx \delta k_T^{(\mathrm{tr},\mathrm{sum})}/k_T^{(s)}$ becomes Pe independent and, because of the summation shift of K^{sum} by $-\frac{1}{12}$, the most accurate choice $K^{\mathrm{sum}} = 0$ is achieved when $\Lambda = t_c^{(a)}/[4(3t_c^{(a)} - 1)]$ with $t_c^{(a)} \in [0, \frac{1}{3}[$. This gives $\Lambda = \frac{1}{4}$ on the coordinate stencil $t_c^{(a)} = \frac{1}{2}$ [and not $\Lambda = \frac{1}{6}$ as predicted by result (46)]; further details on the optimal parameter choice where $K^{\mathrm{sum}} = 0$ can be found in [41].

Further remark. The EMM may incorporate Eq. (42) by adding $b(U')$ to the right-hand side of Eq. (34) and then applying the procedure (39). The $k_T^{(\mathrm{tr})}$ in Eq. (49) remains independent of the coefficients b_1–b_6. At the same time, $\mathrm{Sk}_\star^{(\mathrm{tr})}$ depends on $\{b_3, b_4, b_5\}$ and $\mathrm{Ku}_\star^{(\mathrm{tr})}$ depends upon all coefficients b_1–b_6. Because of b_4 [and then B_4 in Eq. (30)], the numerical dependency on the velocity weight $\{t_q^{(a)}\}$ may not vanish exactly for $\Lambda = \frac{1}{12}$. However, the effects presented by the higher-order velocity corrections are found negligible in the simulations below.

F. Poiseuille profile: Numerical validation

We study the evolution of the initial Dirac delta function $C(x,y) = \delta(x - x_0)$ in Poiseuille profile $U_x(y)$ imposed in straight channel of $H = 20$. The d2Q9 TRT model (17) is combined with the specular-forward boundary reflection (SNL) for no-flux condition at the horizontal boundaries. We first measure the apparent velocity $\mathcal{U}^{(\mathrm{num})}$ with Eq. (24). In agreement with the results [41,50], $\mathcal{U}^{(\mathrm{num})} = \mathcal{U}^{(\mathrm{sum})}$ with $\mathcal{U}^{(\mathrm{sum})}$ given by Eq. (56). Therefore, the boundary-layer velocity correction $\mathrm{err}_U^{(bb)}$ from Eq. (26) is absent from these computations. The error estimate for $k_T^{(\mathrm{num})}$, $\mathrm{Sk}_\star^{(\mathrm{num})}$, and $\mathrm{Ku}_\star^{(\mathrm{num})}$ is computed with Eq. (23) relative to their prediction in Table I. This error estimate is compared with the predicted result (23) for $k_T^{(\mathrm{tr})}$, $\mathrm{Sk}_\star^{(\mathrm{tr})}$, and $\mathrm{Ku}_\star^{(\mathrm{tr})}$. Note: All predicted values are computed by replacing Eqs. (48) with their *summation* counterparts, using Eq. (57) for $k_T^{(\mathrm{tr},\mathrm{sum})}$. Figures 6–9 display the numerical results (symbols) obtained with the d2Q9 SNL for $\mathrm{Pe} \approx \{6.3, 9.5, 95, 95\}$, respectively. The two (limit) velocity-weight values $t_c^{(a)} = \frac{1}{2}$ and $t_c^{(a)} = 0$ are displayed together. The two first diagrams in row show err_D and err(Sk). The two last diagrams show err(Ku) for $t_c^{(m)} = \frac{1}{2}$ and $t_c^{(m)} = 0$. Figure 6 displays results for the three parameter sets $\{c_e, \Lambda^-, \mathcal{U}\}$ at fixed $\mathrm{Pe} \approx 6.3$, when $\Lambda \in [\frac{1}{12}, \frac{1}{4}]$. The numerical parameters for $\mathrm{Pe} \approx 9.5$ (Expt. II) and $\mathrm{Pe} \approx 95$ (Expt. IV) are given in Table II for $n = 2$. The results for $\mathrm{Pe} \approx 95$ in Figs. 8 and 9 differ for c_e and the velocity amplitude.

A very good agreement is demonstrated between the theoretical predictions and the numerical results. They confirm the velocity-weight independence of all truncation errors for $\Lambda \approx \frac{1}{12}$ [a very small shift from $\Lambda = \frac{1}{12}$ can be explained by the truncation term $B_4 U_x^2(y)\partial_x^2\partial_y^2 C$ in Eq. (30), which

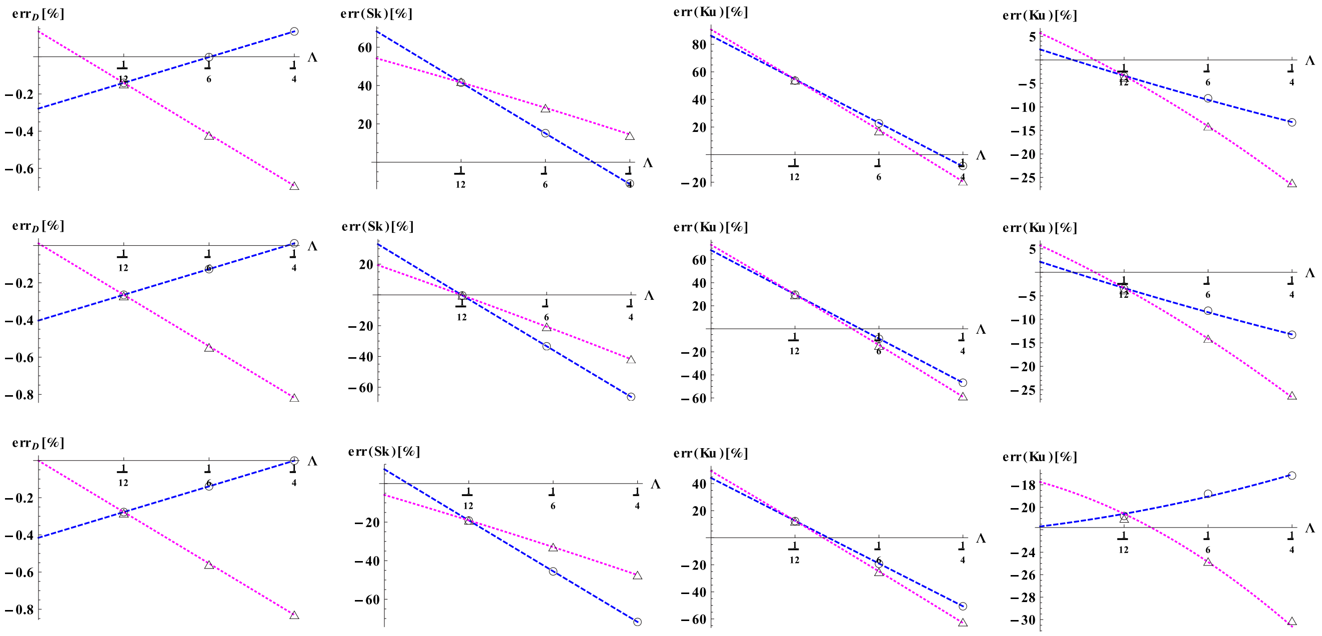

FIG. 6. Numerical results (symbols) for Poiseuille profile in channel of width $H = 20$ are compared to truncation predictions (lines) when velocity weight $t_c^{(a)} = \frac{1}{2}$ [dashed lines (blue), “circles”] and $t_c^{(a)} = 0$ [dotted line (magenta), “triangles”]. The err$_D$ and err(Sk) in two first columns are independent of the mass weight $\{t_q^{(m)}\}$. The err(Ku) is plotted for $t_c^{(m)} = \frac{1}{2}$ (in the third column) and $t_c^{(m)} = 0$ (in the fourth column). The d2Q9 SNL is applied for Pe $\approx$ 6.3 with the three parameter sets: top: $(\Lambda^-)^2 = \frac{1}{3}$, $c_e = \frac{1}{4}$; middle: $(\Lambda^-)^2 = \frac{1}{3}$, $c_e = \frac{1}{40}$; bottom: $(\Lambda^-)^2 = \frac{1}{300}$, $c_e = \frac{1}{4}$. The velocity is reduced by a factor of 10 from top diagram to middle and bottom diagrams.

is neglected in these predictions]. Also, in agreement with the predictions, $k_T^{(\mathrm{num})}$ and $\mathrm{Sk}_\star^{(\mathrm{num})}$ are both mass weight independent, whereas $\mathrm{Ku}_\star^{(\mathrm{num})}$ depends on it. As expected, this dependency is very significant when Pe is small in Figs. 6 and 7, but it almost vanishes when Pe is sufficiently large (the two last diagrams almost coincide in Fig. 8). Let us discuss now these results more in detail.

Dispersion correction err$_D$. Applying the d2Q9 SNL or d2Q5 BB, the $k_T^{(\mathrm{tr,sum})}$ predicted by Eq. (59) is found to be exact [41] for any parameters c_e and Λ^- in the three following families of schemes: (i) the d2Q5, ∀ Λ; (ii) the d2Q9, with $t_c^{(a)} = \frac{1}{2}$, ∀ Λ, and (iii) the d2Q9 with $\Lambda = \frac{1}{4}$, $\forall\, t_c^{(a)} \in [0,\frac{1}{2}]$. In d2Q5, $\Lambda = \frac{1}{4}$ becomes the most accurate choice where $K^{\mathrm{sum}} \approx 0$ as $c_e(\Lambda^-)^2 \to 0$. We confirm conclusions of [41] which are observable in the first diagrams in Figs. 6–8. Namely, as Pe increases, Fig. 8 confirms that err$_D \approx 0$ for $\Lambda = \frac{1}{4}$ in d2Q5 (see results for $t_c^{(a)} = \frac{1}{2}$). Furthermore, this happens even when Pe $\approx$ 6.3 for sufficiently small $c_e(\Lambda^-)^2$ [see Fig. 6, middle and bottom rows]. Additionally, the results in Fig. 6 show that the variation of the truncation dispersion correction with c_e and Λ^- (from the top to the bottom row) is relatively small even at small Pe number, and it practically vanishes as $c_e^2\Lambda^- \to 0$ in Eq. (59). The stable parameter choices for high Pe are examined in [41]; they agree with the von Neumann necessary conditions [43] for $|U|^{\max}(c_e)$, and clearly confirm the superiority of $\Lambda = \frac{1}{4}$ over $\Lambda = \frac{1}{6}$ and $\frac{1}{12}$, both for stability and reliability of the necessary estimate [43,44] for stable velocity amplitude.

Skewness and kurtosis. In contrast with the truncation dispersion, the err(Sk) and err(Ku) noticeably differ in three parameter sets $\{c_e,\Lambda^-,\mathcal{U}\}$ at fixed Pe $\approx$ 6.3 in Fig. 6. As one example, by reducing the velocity and c_e by factor of 10, err(Sk) varies from [20,80]% to [−80,10]% for the two respective choices: $\{(\Lambda^-)^2,c_e\} = \{\frac{1}{3},\frac{1}{4}\}$ and $\{(\Lambda^-)^2,c_e\} = \{\frac{1}{3}\times 10^{-2},\frac{1}{4}\}$, when $t_c^{(a)} = \frac{1}{2}$. Besides, when Pe is small, the reference values $\mathrm{Sk}_\star$ and $\mathrm{Ku}_\star$ tend to zero then err(Sk) and err(Ku) become very significant, in agreement with the very abrupt behavior, in the limit Pe → 0, of err(Sk) and err(Ku) in Fig. 5. Usually, a considerably larger variation with Λ happens for $t_c^{(a)} = 0$. This disparity in errors at small Pe is due to the truncation coefficients dependency on $c_e(\Lambda^-)^2$. Figures 8 and 9

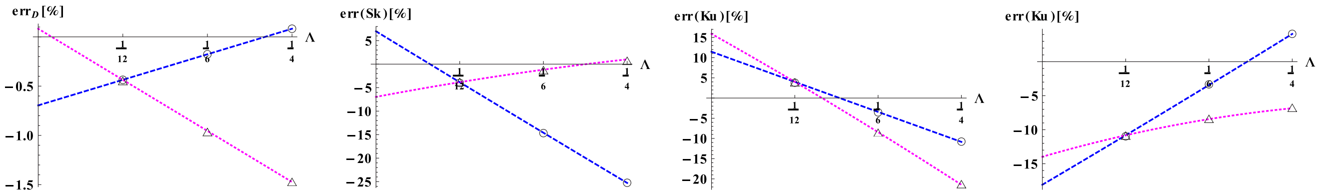

FIG. 7. Expt II. Similarly as in Fig. 6 but for Pe $\approx$ 9.5 modeled with $\Lambda^- = \sqrt{\frac{1}{12}}$, $c_e = \frac{1}{3}$.

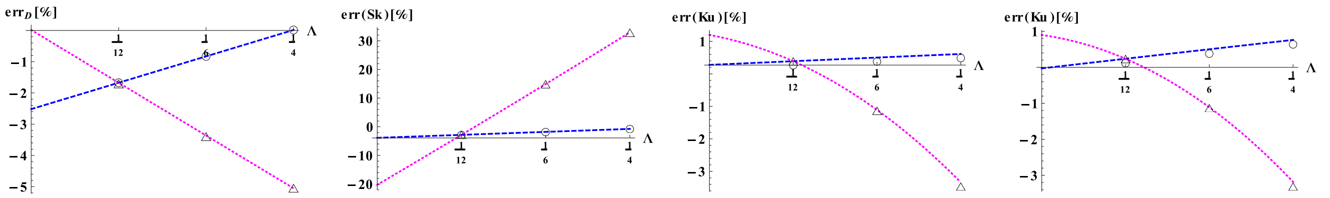

FIG. 8. Expt. IV. Similarly as in Figs. 6 and 7 but for Pe ≈ 95 modeled with $\Lambda^- = \sqrt{\frac{1}{12}}$, $c_e = \frac{1}{30}$.

confirm that such a dependency of err(Sk) and err(Ku) over Λ^- (almost) disappears as Pe increases. Further, Figs. 8 and 9 confirm that |err(Ku)| decreases by one order of magnitude for Pe ≈ 95 against Pe ≈ 9.5 in Fig. 7. This is also true for |err(Sk)| with $t_c^{(a)} = \frac{1}{2}$, whereas the "rotated" velocity stencil $t_c^{(a)} = 0$ displays a (relatively) large variation in err(Sk) with Λ for small and intermediate (and hence, high) Pe, in agreement with the predictions for $t_c^{(a)} = \frac{1}{2}$ and $t_c^{(a)} = \frac{1}{3}$ in the two first diagrams in Fig. 5.

G. Poiseuille profile: Summary

The apparent solutions for dispersion, skewness, and kurtosis are derived with the help of the EMM approach. Their coefficients $k_T^{(\mathrm{tr})}$, $\mathrm{Sk}_\star^{(\mathrm{tr})}$, and $\mathrm{Ku}_\star^{(\mathrm{tr})}$ are computed with Eqs. (15) using the obtained solution given by Eqs. (48). Replacing $\mathcal{U}$ by $\mathcal{U}^{(\mathrm{sum})}$ in Eqs. (48), and computing all averaged values via summation, the EMM properly accounts for the summation errors due to the discrete integration of moments. The EMM results for $k_T^{(\mathrm{tr})}$ then coincide with the analysis in [41] developed by applying the Taylor argument to truncation terms. The constructed relative corrections in dispersion, skewness, and kurtosis are predicted to behave with second-order accuracy. They are validated in the whole parameter space with the d2Q9 SNL scheme. We expect them to be helpful for the free-parameter optimization in three groups: $\{c_e, \Lambda^-, \mathcal{U}\}$ at fixed Pe, $\{t_q^{(m)}, t_q^{(a)}\}$, and Λ.

In agreement with our predictions, the numerical values of dispersion and skewness depend on the velocity-weight value $t_c^{(a)}$, while the kurtosis depends on both velocity- and mass-weight values. Concerning the first parameter group $\{c_e, \Lambda^-, \mathcal{U}\}$, the accuracy of all transport coefficients strongly depends on Λ^- at small Pe where $\mathrm{Sk}_\star$ and $\mathrm{Ku}_\star$ may obtain huge relative truncation errors. However, since these transport coefficients are small within this range, the truncation errors do not modify the profiles noticeably (this is demonstrated in [51] still for larger relative boundary-layer diffusion errors at small Pe). Further, the truncation result dependency on c_e and Λ^- almost vanishes when Pe ⩾ ≈10^2, and the dependency of err(Sk) and err(Ku) on c_e vanishes when $\Lambda = \frac{1}{4}$ in the limit of high Pe.

Concerning the weights and Λ, we notice that the d2Q5, or at least the coordinate velocity stencil $t_c^{(a)} = \frac{1}{2}$, produces relatively small dependency upon Λ for all transport coefficients at any Péclet number. The d2Q5 model with $\Lambda = \frac{1}{4}$ then presents a very stable, efficient, and sufficiently accurate choice, although $\Lambda = \frac{1}{6}$ is the most accurate for all three transport coefficients with the minimal schemes (without summation effect). Further, $\Lambda = \frac{1}{12}$ makes all truncation results velocity weight independent. The results of the diagonal stencils are very sensitive to the individual choice of Λ on coarse grids. The hydrodynamic weights in combination with $\Lambda = \frac{1}{12}$ present another interesting choice for the isotropy of the high-order corrections and improved accuracy, but this combination is generally less stable than the d2Q5 with $\Lambda = \frac{1}{4}$ (see [41,44]) and produces nonzero asymptotic errors in all three transport coefficients.

Finally, we also computed solutions with the (modified) MFTCS Lax-Wendroff scheme [63], where the second-order numerical diffusion is suppressed similar to Eq. (17), e.g., by adding U_x^2 correction to modeled diffusion coefficient D_{xx} in one-dimensional velocity profile. The periodic conditions were applied on the flat walls because, due to symmetry, they produce the same solutions in straight channel as the specular-forward reflection. We find the same steady-state solutions for $k_T^{(\mathrm{num})}$, $\mathrm{Sk}_\star$, and $\mathrm{Ku}_\star$ with the MFTCS scheme and OTRT-BGK scheme ($\Lambda^\pm = \frac{1}{2}$, $t_c^{(u)} = \frac{1}{2}$) on the coordinate and diagonal stencils. Their transport coefficients are related via $\boldsymbol{U}^{fd} = \boldsymbol{U}\frac{\delta_x}{\delta_t}$ and $D_0^{fd} = \frac{1}{2}c_e\frac{\delta_x^2}{\delta_t}$. Due to the freedom in the selection of c_e in OTRT($\Lambda^\pm = \frac{1}{2}$), and δ_t in MFTCS, the two schemes operate with equivalent stability conditions [43]. Otherwise, based on the stability criteria [43] the underlying time step of the OTRT becomes more advantageous against the MFTCS in advection-dominant regime when $\Lambda^- < \frac{1}{2}$. In diffusion-dominant zone, reversely, $\Lambda^- > \frac{1}{2}$ is more advantageous.

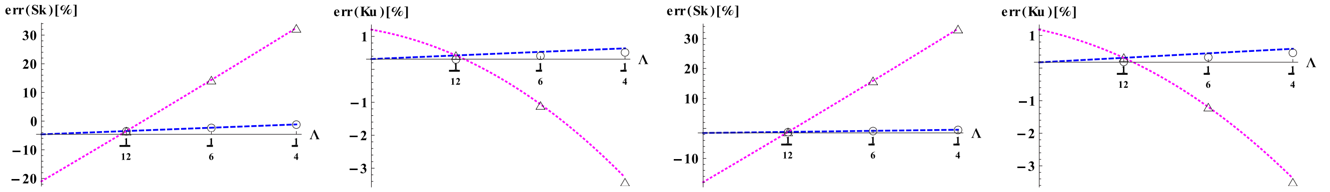

FIG. 9. Expt. IV. Similarly as the second and third diagrams in Fig. 8 but with $\Lambda^- = \sqrt{\frac{1}{3}}$, $c_e = \frac{1}{60}$ in the two first diagrams, and $\Lambda^- = \frac{1}{8} \times \sqrt{\frac{1}{3}}$, $c_e = \frac{2}{15}$ in the two last diagrams.

IV. CYLINDRICAL CAPILLARY

Section IV A recalls the derivation of the Taylor longitudinal dispersion coefficient k_T for parabolic profile prescribed in a cylindrical capillary; Sec. IV B formulates the corresponding fourth-order accurate equation of the d3Q15 TRT scheme and derives the truncation coefficient $k_T^{(\mathrm{tr})}$ following [41]; Sec. IV C produces the closed-form truncation estimates for $k_T^{(\mathrm{tr})}$, $\mathrm{Sk}_\star^{(\mathrm{tr})}$, and $\mathrm{Ku}_\star^{(\mathrm{tr})}$ using the EMM approach, discusses their behavior with Pe, and compares the optimal parameter combinations with the channel strategies; Sec. IV D numerically addresses the effective velocity, diffusion, numerical diffusion, dispersion, skewness, and kurtosis, where the boundary-layer diffusion, due to the isotropic mass weight $t_c^{(m)}=\frac{1}{3}$, and boundary-layer dispersion, due to the diagonal velocity weight $t_d^{(a)}\in]0,\frac{1}{4}]$, is subtracted from the numerical values. A comparison of the minimal and full equilibrium stencils, an extension for other duct flows and a reduction of the bounce-back effects with the double-Λ scheme, is outlined in Sec. IV E.

A. Taylor dispersion

Assume the parabolic profile $\boldsymbol{U}(x,y,z)=U_x(r)=2\mathcal{U}(1-\frac{r^2}{R^2})$ to be prescribed along the x axis in a cylindrical capillary of radius R, for $r^2=y^2+z^2\leqslant R^2$. Since the flow is invariant along the streamwise direction, the anti-numerical-diffusion correction in Eq. (17) reduces to $\frac{1}{2}t_q^{(u)}U_x^2C$ and it is sufficient to eliminate the entire second-order numerical-diffusion according to Eq. (A3) [which reads as $[S_1]C=U_x(r)\partial_xC$, $[D_2]C=c_e(\partial_x^2C+\partial_y^2C+\partial_z^2C)$]. The modeled second-order-accurate ADE for isotropic distribution $C(x,r,t)$ reads as in cylindrical coordinates (x,r)

$$\partial_tC+U_x(r)\partial_xC=c_eD_0\big(\partial_x^2C+\Delta_rC\big),$$
$$\Delta_rC(x,r)=\frac{1}{r}\partial_r(r\partial_rC(x,r)). \tag{60}$$

This equation is subject to the impermeability condition $\partial_rC|_{r=R}=0$. Following Taylor [4], $C(x,r,t)$ and $U_x(r)$ are decomposed around their cell-averaged values $\bar{C}(x,t)$ and $\mathcal{U}$, respectively:

$$C(x,r,t)=\bar{C}(x,t)+C'(x,r,t),$$
$$\bar{C}(x,t)=\langle C(x,r,t)\rangle=\frac{2\pi}{\pi R^2}\int_0^R C(x,r,t)r\,dr,$$
$$\partial_rC'|_{r=R}=0,$$
$$U_x(r)=\mathcal{U}+U'(r),\quad \mathcal{U}=\langle U_x(r)\rangle=\frac{2\pi}{\pi R^2}\int_0^R U_x(r)r\,dr. \tag{61}$$

The averaged concentration $\bar{C}(x,t)$ is expected to obey Eq. (2), that is, to propagate with the mean velocity $\mathcal{U}$ and to spread with the longitudinal dispersion coefficient $D=(1+k_T^{(c)})D_0$. Originally, $k_T^{(c)}$ is derived with the help of the Taylor ansatz [4]:

$$D_0\Delta_rC'(x,r,t)\approx U'(r)\partial_x\bar{C}(x,t),$$
$$\text{then}\quad C'(x,r,t)\approx\frac{\alpha(r)}{D_0}\partial_x\bar{C}(x,t),$$
$$\alpha(r)=\frac{\mathcal{U}}{16}\left(r^2-\frac{r^4}{2R^2}\right). \tag{62}$$

The averaged-flux component $\langle U'(r)\partial_xC'\rangle$ then modifies the molecular-diffusion flux $-D_0\partial_x\bar{C}$ by a quantity $-k_T^{(c)}D_0\partial_x\bar{C}$, with

$$k_T^{(c)}=-\frac{\langle U'(r)\alpha(r)\rangle}{D_0^2}$$
$$=-\frac{2\pi}{\pi R^2D_0^2}\int_0^R U'(r)\alpha(r)r\,dr=\frac{\mathrm{Pe}^2}{192},$$
$$\text{with } \mathrm{Pe}=\frac{2\mathcal{U}R}{D_0}. \tag{63}$$

B. Truncation prediction for numerical dispersion

In three dimensions, the fourth-order diffusion truncation correction (A7) reads as with the following component:

$$[S_4]C(x,y,z,t)=\sum_{q=1}^{Q_m}\partial_q^4e_q^+=c_e\sum_{q=1}^{Q_m}t_q^{(m)}[(\partial_xc_{qx}+\partial_yc_{qy}+\partial_zc_{qz})^4]C(x,y,z,t)$$
$$=c_e\big[\partial_x^4+\partial_y^4+\partial_z^4+6S_d\big(\partial_x^2\partial_y^2+\partial_x^2\partial_z^2+\partial_y^2\partial_z^2\big)\big]C(x,y,z,t),\quad S_d(t_q^{(m)})=\sum_{q:\alpha\neq\beta}t_q^{(m)}c_{q\alpha}^2c_{q\beta}^2,$$
$$[S_4]C(x,y,z,t)=c_e\big[\partial_x^2+\Delta_r\big]^2C(x,y,z,t),\quad\text{if}\quad S_d\big(t_q^{(m)}\big)=\frac{1}{3}. \tag{64}$$

The diffusion form $[S_4]C$ is isotropic only with the "hydrodynamic" mass weight where $S_d(t_q^{(m)})=\frac{1}{3}$. The third- and fourth-order truncation corrections given by Eqs. (A4)–(A6) then read as (dropping in them U_x^α terms for $\alpha\geqslant2$)

$$[R_3]C(x,r,t)\approx A_1U_x(r)[\partial_x\Delta_r]C+A_2U_x(r)\partial_x^3C,$$
$$[R_4]C(x,r,t)\approx A_3\partial_x^4C+A_4\partial_x^2\Delta_rC+A_0\big[\Delta_r^2\big]C,\quad\text{if}\quad S_d\big(t_q^{(m)}\big)=\tfrac{1}{3},\quad\Delta_r^2=[\Delta_r]\Delta_rC. \tag{65}$$

The fourth-order-accurate equation becomes

$$\partial_tC+U_x(r)\partial_xC=c_eD_0\big(\partial_x^2C+\Delta_rC\big)+A_1U_x(r)\partial_x\Delta_rC+A_2U_x(r)\partial_x^3C+A_3\partial_x^4C+A_4\partial_x^2\Delta_rC+A_0\Delta_r^2C,\quad\text{if}\quad S_d\big(t_q^{(m)}\big)=\tfrac{1}{3}. \tag{66}$$

The coefficients A_0–A_4 are the same as in Eq. (29).

The following derivation of the numerical dispersion from the truncation corrections follows [41]. Substitution of the Taylor ansatz (62), $A_0\Delta_r^2C$ in Eq. (66) becomes equal to $(A_0/D_0)\Delta_r U'(r)\partial_x\bar{C}$. This suggests the numerical correction to Taylor ansatz (62), as

$$D_0\Delta_r C' \approx U'(r)\partial_x\bar{C} - (A_0/D_0)\Delta_r U'(r)\partial_x\bar{C}, \quad \text{then} \;\; C'(r) = \frac{\alpha(r) - (A_0/D_0)U'(r)}{D_0}\partial_x\bar{C}. \tag{67}$$

In this relation, $\alpha(r)$ is given by Eq. (62). By averaging Eq. (60), the advective component $\langle U'(r)\partial_x C'\rangle$ then complements the Taylor dispersion form by the truncation term $(A_0/D_0^2) < U'(r)U'(r) > \partial_x^2 C$. A similar correction originates from the truncation term $A_1 U_x(r)\partial_x\Delta_r C$ by plugging Taylor ansatz (62) there. The apparent dispersivity of the scheme $k_T^{(\mathrm{tr})}$ then consists of the Taylor coefficient $k_T^{(c)}$ and the truncation correction $\delta k_T^{(\mathrm{tr})}$:

$$k_T^{(\mathrm{tr})} \approx k_T^{(c)} + \delta k_T^{(\mathrm{tr})}, \quad \delta k_T^{(\mathrm{tr})} = K k_T^{(1,c)}, \quad K = \left(A_1 + \frac{A_0}{D_0}\right) = \left[c_e(\Lambda^-)^2 + \Lambda - \frac{1}{6}\right] - 3S_d\left(t_q^{(a)}\right)\left(\Lambda - \frac{1}{12}\right),$$
$$k_T^{(1,c)} = \frac{\langle U'(r)U'(r)\rangle}{D_0^2} = \frac{2\pi}{\pi R^2 D_0^2}\int_0^R U'^2(r) r\,dr = \frac{\mathrm{Pe}^2}{12R^2}, \quad \mathrm{Pe} = \frac{2\mathcal{U}R}{D_0}. \tag{68}$$

Its relative contribution $\mathrm{err}_D^{(\mathrm{tr})}$ reads as

$$\mathrm{err}_D^{(\mathrm{tr})} = \frac{\delta k_T^{(\mathrm{tr})}}{1 + k_T^{(c)}}, \quad \mathrm{err}_D^{(\mathrm{tr})}|_{\mathrm{Pe}\to\infty} = \frac{16K}{R^2}, \quad \text{with } K|_{\mathrm{Pe}\to\infty} = \left(\Lambda - \frac{1}{6}\right) - 3S_d\left(t_q^{(a)}\right)\left(\Lambda - \frac{1}{12}\right),$$
$$t_c^{(a)} \in \left[0,\frac{1}{6}\right] \Big\| \left]\frac{1}{3},\frac{1}{2}\right] \;:\; K|_{\mathrm{Pe}\to\infty} = 0 \text{ if } \Lambda = \frac{1}{12}\frac{2 - 3S_d\left(t_q^{(a)}\right)}{1 - 3S_d\left(t_q^{(a)}\right)},$$
$$t_c^{(a)} = \frac{1}{2} \;:\; K|_{\mathrm{Pe}\to\infty} = \Lambda - \frac{1}{6}, \quad K|_{\mathrm{Pe}\to\infty} = 0 \text{ if } \Lambda = \frac{1}{6},$$
$$t_c^{(a)} = \frac{1}{3} \text{ or } \Lambda = \frac{1}{12} \;:\; K|_{\mathrm{Pe}\to\infty} = -\frac{1}{12}. \tag{69}$$

The coefficient K is the same as for straight channel in Eq. (46). However, rigorously, this result is only expected to be valid in a capillary when $S_d(t_q^{(m)}) = \frac{1}{3}$, that is, for $\{t_c^{(m)} = \frac{1}{3}, t_d^{(m)} = \frac{1}{24}\}$ in d3Q15 and $\{t_c^{(m)} = \frac{1}{6}, t_d^{(m)} = \frac{1}{12}\}$ in d3Q19, excluding the d3Q7 model. In other words, unlike in straight channel, the truncation dispersion is expected to depend on the mass weight $\{t_q^{(m)}\}$, on top of the velocity weight $\{t_q^{(a)}\}$. The notable exception happens with $\Lambda = \frac{1}{6}$ where the coefficient $c_{4,3}$ of $[S_4]C$ vanishes [see Eqs. (A6) and (A8)]. The validity of Eq. (68) for $t_c^{(m)} = \frac{1}{3}$ and $t_c^{(m)} = \frac{1}{2}$, in combination with different velocity-weight values, is examined in Sec. IV D 3. As has been suggested in [41], the parameter configuration allowing to vanish $\mathrm{err}_D^{(\mathrm{tr})}$ via $K \approx 0$, as given by second and third lines in Eq. (69), is flow and dimension independent. However, the discretization corrections further modify this *optimal-dispersion* parameter space, as predicted by Eq. (58) for channel and will be predicted by Eq. (78) for capillary.

C. Truncation dispersion, skewness, and kurtosis by the EMM

Our purpose is to construct the EMM solutions for $k_T^{(\mathrm{tr})}$, $\mathrm{Sk}_\star^{(\mathrm{tr})}$, and $\mathrm{Ku}_\star^{(\mathrm{tr})}$ from the fourth-order-accurate mass-conservation equation (66). These truncation predictions are to be compared with the EMM physical result in Table I. Since the solution constructed here should reduce to result [15] for the case of zero truncation coefficients, we adopt notations [15] in this section, with $\mathcal{L} = R$, $\mathrm{Pe}_R = \mathcal{U}R/D_0$, to be distinguished from $\mathrm{Pe} = 2\mathcal{U}R/D_0$. In dimensionless coordinates $x' = x/\mathcal{L}, r' = r/\mathcal{L}$, $t' = t\mathcal{U}/\mathcal{L}$, Eq. (66) becomes (multiplied by $\mathcal{L}/\mathcal{U}$)

$$\partial_{t'}C + \tilde{U}_x(y')\partial_{x'}C = \mathrm{Pe}_R^{-1}\left(\partial_{x'}^2 C + \Delta_{r'}C\right) + a_1\tilde{U}_x(y')\partial_{x'}\Delta_{r'}C + a_2\tilde{U}_x(y')\partial_{x'}^3 C + a_3\mathrm{Pe}_R^{-1}\partial_{x'}^4 C + a_4\mathrm{Pe}_R^{-1}\partial_{x'}^2\Delta_{r'}C + a_0\mathrm{Pe}_R^{-1}\Delta_{r'}^2 C,$$
$$\text{with } \tilde{U}_x(r') = \frac{U_x(r)}{\mathcal{U}}, \quad a_1 = \frac{A_1}{\mathcal{L}^2}, \quad a_2 = \frac{A_2}{\mathcal{L}^2}, \quad a_3 = \frac{A_3}{D_0\mathcal{L}^2}, \quad a_4 = \frac{A_4}{D_0\mathcal{L}^2}, \quad a_0 = \frac{A_0}{D_0\mathcal{L}^2}. \tag{70}$$

Similar to Eq. (35), the solution of Eq. (70) is presented as

$$C(x',r',t') = \frac{1}{2\pi}\tilde{\mathcal{P}}(\omega',r')\exp[i(\gamma' x' - \omega' t')]. \tag{71}$$

Further analysis makes use of Eqs. (14) with Eqs. (39) by sequentially replacing there y' by r', $\partial_{y'}^2 C$ by $\Delta_{r'}C$, and $\partial_{y'}^4 C$ by $\Delta_{r'}^2 C$. These equations are first solved for $\Delta_{r'}\mathcal{B}^{(n)}(r')$ and then integrated twice to obtain $\mathcal{B}^{(n)}(r')$. The averaging $\langle\psi'(r')\rangle =$

$2\int_0^1 \psi'(r')r'dr'$ is applied. When all coefficients a_n vanish, this procedure reduces to Eqs. (86)–(91) in [15] [for their scale factor $h(r') = r'$ and uniform porosity $\phi = 1$]. Solution for $\gamma'^{(2)}$ gives the numerical dispersivity $k_T^{(\mathrm{tr})}$:

$$\gamma'^{(2)}\mathrm{Pe}_R = 1 + \left(\frac{1}{48} + \frac{a_0 + a_1}{3}\right)\mathrm{Pe}_R^2, \quad \text{then}$$

$$k_T^{(\mathrm{tr})} = \mathrm{Pe}_R\gamma'^{(2)} - 1 = k_T^{(c)} + \delta k_T^{(\mathrm{tr})}, \quad k_T^{(c)} = \frac{\mathrm{Pe}^2}{192}, \quad \delta k_T^{(\mathrm{tr})} = \frac{A_1 + A_0/D_0}{12R^2}, \quad \mathrm{Pe} = 2\mathrm{Pe}_R = \frac{2\mathcal{U}R}{D_0}. \tag{72}$$

This solution coincides with the truncation result presented in Eq. (68). Further, as in straight channel, $\gamma'^{(2)}$ depends only on a_0 and a_1, $\gamma'^{(3)}$ depends, in addition, on a_3, while $\gamma'^{(4)}$ depends on all coefficients a_1–a_4. The dimensionless coefficients $\mathrm{Sk}_\star^{(\mathrm{tr})} = \mathrm{Sk}(t) \times \sqrt{tU/R}$ and $\mathrm{Ku}_\star^{(\mathrm{tr})} = \mathrm{Ku}(t) \times tU/R$ are derived with the help of Eq. (15):

$$\begin{aligned}
\mathrm{Sk}_\star^{(\mathrm{tr})} &= \frac{3\omega'^{(3)}}{\sqrt{2}\left|\omega'^{(2)}\right|^{3/2}} = \frac{A^{(\mathrm{Sk})}}{10B^{(\mathrm{tr})}}, \quad \mathrm{Ku}_\star^{(\mathrm{tr})} = -\frac{6\omega'^{(4)}}{(\omega'^{(2)})^2} = \frac{A^{(\mathrm{Ku})}}{1120B^{(\mathrm{tr})}},\\
A^{(\mathrm{Sk})} &= \sqrt{3}\sqrt{\mathrm{Pe}}[-23040a_2 + (1 + 60a_1)(1 + 16a_1 + 16a_0)\mathrm{Pe}^3],\\
A^{(\mathrm{Ku})} &= -743178240a_2 + 123863040\mathrm{Pe}(3a_2 + a_3) - 5160960a_2\mathrm{Pe}^2(1 + 16a_1 + 16a_0) + \mathrm{Pe}^4\{645120[-a_4 - 16a_4(a_1 + a_0)\\
&\quad + a_2(2 + 48a_1 + 32a_0)]\} + \mathrm{Pe}^6\big(-123 + 3776a_1 + 32\big\{102144a_1^3 + 448a_1a_0(5 + 24a_0)\\
&\quad + 224a_1^2(41 + 528a_0) - a_0[155 + 112a_0(17 + 48a_0)]\big\}\big),\\
B^{(\mathrm{tr})} &= [192 + (1 + 16a_1 + 16a_0)\mathrm{Pe}^2]^2.
\end{aligned} \tag{73}$$

When all truncation coefficients are set equal to zero, $\mathrm{Sk}_\star^{(\mathrm{tr})}$ and $\mathrm{Ku}_\star^{(\mathrm{tr})}$ reduce to their $\mathrm{Sk}_\star$ and $\mathrm{Ku}_\star$ values in Table I. The truncation corrections in k_T, $\mathrm{Sk}_\star$, and $\mathrm{Ku}_\star$ all decay with second-order accuracy [cf. Eqs. (74) and (75)], alike in straight channel. They also keep the same four principal properties: (i) $k_T^{(\mathrm{tr})}$, $\mathrm{Sk}_\star^{(\mathrm{tr})}$, and $\mathrm{Ku}_\star^{(\mathrm{tr})}$ depend on the velocity weight $\{t_q^{(a)}\}$ ∀ Λ, except for $\Lambda = \frac{1}{12}$; (ii) $\mathrm{Ku}_\star^{(\mathrm{tr})}$ depends on the mass weight $\{t_q^{(m)}\}$ via a_4, except for $\Lambda = \frac{1}{6}$. Asymptotically, when $\Lambda^- \to 0$, (iii) the dependency of $\mathrm{Sk}_\star^{(\mathrm{tr})}$ and $\mathrm{Ku}_\star^{(\mathrm{tr})}$ on c_e vanishes with $\Lambda = \frac{1}{4}$; in turn, (iv) the dependency on Λ^- vanishes in all three transport coefficients when $c_e \to 0$. For illustration, let us substitute coefficients into Eq. (73) and consider limit $\Lambda^- \to 0$. The leading R^{-2} term in err(Sk) takes the form [an expression for err(Ku) is lengthy]

$$\begin{aligned}
\mathrm{err(Sk)}|_{\Lambda^-\to 0} &= \frac{15R^{-2}(-384 + \mathrm{Pe}^3)(-1 + 4\Lambda)c_e}{\mathrm{Pe}^3} + \frac{2R^{-2}(-1 + 12\Lambda)(3648 + 13\mathrm{Pe}^2)t_c^{(a)}}{192 + \mathrm{Pe}^2}\\
&\quad + \frac{R^{-2}}{3}\left[43 - 492\Lambda - \frac{5760(1 - 12\Lambda)}{\mathrm{Pe}^3} + \frac{1152(1 - 24\Lambda)}{(192 + \mathrm{Pe}^2)}\right],
\end{aligned} \tag{74}$$

$$\mathrm{err(Sk)}|_{\Lambda^-\to 0,\mathrm{Pe}\to\infty} = \frac{R^{-2}}{3}\left[43 - 492\Lambda + 45c_e(-1 + 4\Lambda) + 78(-1 + 12\Lambda)t_c^{(a)}\right], \tag{75}$$

$$\mathrm{err(Sk)}|_{\Lambda^-\to 0,c_e\to 0} \approx 0 \quad \text{if} \quad \Lambda = \frac{1}{6} - \frac{13\big(2t_c^{(a)} - 1\big)}{4\big(78t_c^{(a)} - 41\big)} \; \forall\, t_c^{(a)} \in \left[0,\frac{1}{2}\right], \quad \Lambda\left(t_c^{(a)} = \frac{1}{2}\right) = \frac{1}{6}, \quad \Lambda\left(t_c^{(a)} = \frac{1}{3}\right) = \frac{17}{180}. \tag{76}$$

Similar to $\delta k_T^{(\mathrm{tr})}$ in Eq. (68), the most accurate asymptotic solutions, where err(Sk) = 0 or err(Ku) = 0 in the limit Pe → ∞, are achieved with the specific distinguished functions $\Lambda(t_c^{(a)})$. Like in straight channel, $\Lambda = \frac{1}{6}$ then presents the most accurate choice on the coordinate velocity stencil, both for k_T and Sk [cf. Eqs. (69), (52), and (76)]. Moreover, the two dependencies $\Lambda(t_c^{(a)})$ in Eqs. (52) and (76) are very similar between channel and capillary, with $\Lambda(t_c^{(a)} = \frac{1}{3}) \approx \frac{1}{10}$. This suggests that the hydrodynamic weight $t_c^{(a)} = \frac{1}{3}$ in combination with $\Lambda = \frac{1}{12}$ presents a sufficiently accurate alternative to the combination of the coordinate stencil $t_c^{(a)} = \frac{1}{2}$ with $\Lambda = \frac{1}{6}$ or $\Lambda = \frac{1}{4}$. But, $\Lambda = \frac{1}{12}$ is much less stable [35,41,44].

Figure 10 illustrates the predicted relative differences err(Sk) and err(Ku) from Eq. (23) in the limit $c_e \to 0$. They are displayed versus Pe ∈ [20,3 × 10²] for $R = 20$ (the two first diagrams in row), and versus R for Pe = 100 (the two last diagrams in row). The two weight families are employed: $t_c^{(a)} = \frac{1}{2}$, $t_c^{(m)} = \frac{1}{3}$ in the top row and $t_c^{(a)} = t_c^{(m)} = \frac{1}{3}$ in the bottom row. Notice, $t_c^{(m)} = \frac{1}{2}$ is not considered here because of its fourth-order anisotropy in Eqs. (64)–(66). Overall, the behavior in cylindrical capillary with Λ, velocity weight, and space resolution is very similar to the channel results in Fig. 5. Hence, the same previous conclusions hold. Namely, $k_T^{(\mathrm{tr})}$, $\mathrm{Sk}_\star^{(\mathrm{tr})}$, and $\mathrm{Ku}_\star^{(\mathrm{tr})}$ are $\{t_q^{(a)}-\}$ independent for $\Lambda = \frac{1}{12}$. On the coarse grid, the coordinate velocity weight $t_c^{(a)} = \frac{1}{2}$ produces a much smaller sensitivity on Λ. With this weight choice, $\Lambda = \frac{1}{6}$ remains the most accurate solution for sufficiently large Pe. By using the "hydrodynamic" stencil (at the bottom row), $\Lambda = \frac{1}{12}$ gains in accuracy within interval $\Lambda \in [\frac{1}{12},\frac{1}{4}]$, in agreement with Eq. (74). However, like in straight channel, the

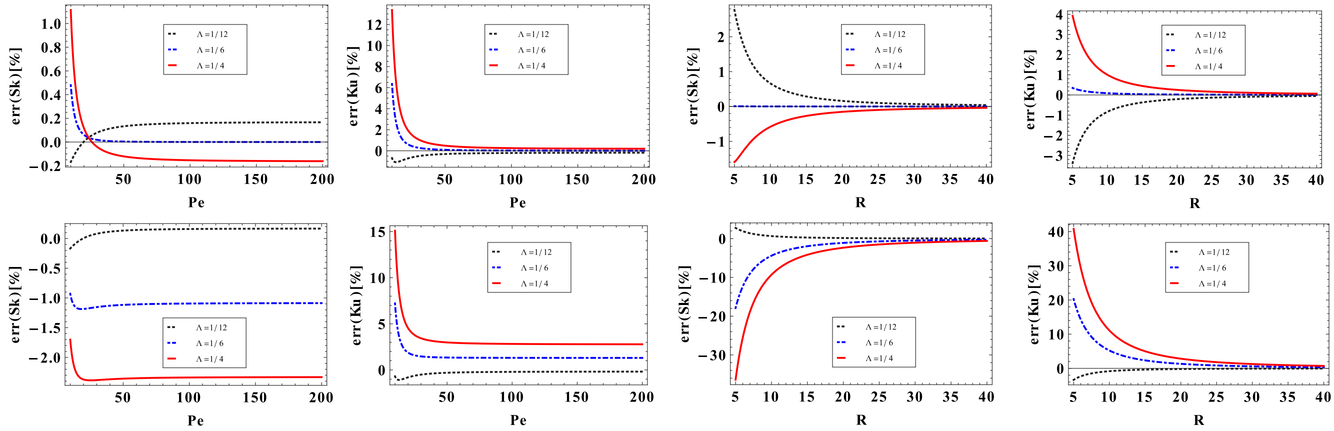

FIG. 10. Poiseuille flow in cylindrical pipe. This figure displays predicted solution (73) for truncation corrections err(Sk) and err(Ku) in the limit $c_e \to 0$ for three Λ values: $\Lambda = \frac{1}{12}$ (black, dotted line), $\Lambda = \frac{1}{6}$ (blue, dotted-dashed line), $\Lambda = \frac{1}{4}$ (red, solid line). Top row: $t_c^{(a)} = \frac{1}{2}$, $t_c^{(m)} = \frac{1}{3}$. Bottom row: $t_c^{(a)} = t_c^{(m)} = \frac{1}{3}$. The two first diagrams are plotted for $R = 20$, when $\mathrm{Pe} \in [10, 2 \times 10^2]$. The two last diagrams are plotted for $\mathrm{Pe} = 10^2$, when $R \in [5,40]$.

three coefficients have nonzero truncation corrections with this combination. When Pe increases, $\mathrm{err}_D^{(\mathrm{tr})}$, err(Sk), and err(Ku) all become asymptotically Pe independent.

D. Numerical experiments

The numerical validation with the d3Q15 BB scheme adopts the parameter range from Table II for the evolution of the Dirac δ function $C(x,t=0) = \delta(x - x_0)$ in parabolic streamwise-invariant flow $U_x(r)$. The mean-velocity magnitude $\mathcal{U}(R=5)$ is fixed by the stability line $|U|^{\max} = 2\mathcal{U} = \sqrt{c_e}$ for $c_e = \frac{1}{30}$; further, $\mathcal{U}(R)$ linearly reduces with the mesh refining. Although the condition $U^2 \leqslant c_e$ is not necessary in the presence of the U_x^2 term in Eqs. (17), the necessary condition, such as $U^2 \leqslant 3/2c_e$ in d3Q7, is in principle only sufficient for $\Lambda = \frac{1}{4}$, whereas the smaller valued Λ have a much lower velocity bound [35,44]. Besides, the condition $U^2 \leqslant c_e$ becomes necessary for all velocity sets when the $U_\alpha U_\beta$ equilibrium terms are omitted. Therefore, we will first verify the numerical-diffusion estimate in this configuration. Because of the fourth-order isotropy, the focus is on the "hydrodynamic" mass weight $t_q^{(m)} = \{\frac{1}{3}, \frac{1}{24}\}$ while the velocity weight varies, $t_c^{(a)} \in [0, \frac{1}{2}]$. It is predicted by Eqs. (25)–(27) that, while absent in d3Q7 BB, the d3Q15 BB produces diagonal weight dependent corrections to the mean velocity, diffusion, and dispersion. We will account for all these effects in order to quantify their respective roles and verify truncation predictions.

1. *Apparent velocity*

In computations, the apparent velocity $\mathcal{U}^{(\mathrm{num})}$ is extracted from the first moment with Eq. (24) and its relative correction is measured via $\mathrm{err}_U = \mathcal{U}^{(\mathrm{num})}/\mathcal{U} - 1$. The summation correction $\mathrm{err}_U^{(\mathrm{sum})}(R) = \mathcal{U}^{(\mathrm{sum})}/\mathcal{U} - 1$ is specified in Table VI: $\mathcal{U}^{(\mathrm{sum})}$ is computed as the arithmetical mean value of grid velocity values in the discretized circular pipe. It is interesting that the decay of $\mathrm{err}_U^{(\mathrm{sum})}(R)$ is not monotonous with R. Figure 11 presents results for the relative mean-velocity error $\mathrm{err}_U^{(bb)}(t_c^{(a)}, \Lambda, R) = \mathrm{err}_U - \mathrm{err}_U^{(\mathrm{sum})}(R)$ in cylindrical capillary of radius $R = \{5, 10, 20\}$ for three Λ values, versus the coordinate weight value $t_c^{(a)}$. The presented results confirm Eq. (26): that is, (i) $\mathcal{U}^{(\mathrm{num})} = \mathcal{U}^{(\mathrm{sum})}$ for $t_c^{(a)} = \frac{1}{2}$; (ii) the error amplitude $|\mathrm{err}_U^{(bb)}|$ increases with Λ; and (iii) it linearly grows with the diagonal weight $t_d^{(m)}$. We confirm that $\mathrm{err}_U^{(bb)}$ is set by Λ, $\{t_q^{(a)}\}$, and R, independently of the velocity amplitude and the other model parameters. The computations in Fig. 11 are run with the parameters of Expt. II from Table II, but $\mathrm{err}_U^{(bb)}$ is velocity and Pe independent. The work [51] compares the presented results to theoretical estimate for the $\mathrm{err}_U^{(bb)}$ constructed there.

2. *Numerical diffusion*

Prior to the validation of the numerical dispersion, we verify that the averaged second-order equation (2) is achieved with Eq. (17) without numerical diffusion. When the U_x^2 term is omitted in Eq. (17), the prescribed coefficient $D_0 = c_e\Lambda^-$ in Eq. (2) is expected to diminish by the (averaged) quantity of the numerical diffusion $-\langle U_x^2\rangle\Lambda^-$. Its relative contribution $||\mathrm{err}_D||$ reads as on the parabolic profile

$$\begin{aligned} ||\mathrm{err}_D|| &= \mathrm{err}_D|_{U_x^2\to 0} - \mathrm{err}_D \\ &\approx -\frac{\langle U_x^2\rangle}{c_e\left(1 + k_T^{(c)}\right)} = -\frac{4\mathcal{U}^2}{3c_e\left(1 + k_T^{(c)}\right)}, \\ ||\mathrm{err}_D||_{k_T^{(c)}\gg 1} &\approx -\frac{4 \times 192\mathcal{U}^2}{3c_e\mathrm{Pe}^2} = -\frac{64c_e(\Lambda^-)^2}{R^2}. \end{aligned} \quad (77)$$

Note that the numerical diffusion is negative in duct flow. Table V displays the d3Q15 BB results without and with the U_x^2 term in Eq. (17), for Expts. I and IV from Table II when $R = 5$. The two families of the equilibrium weights and the three distinguished values of Λ are examined to verify that the difference of the results $||\mathrm{err}_D^{(\mathrm{num})}||$ is mainly due to the second-order numerical diffusion. The results confirm that, although $\mathrm{err}_D^{(\mathrm{num})}|_{U_x^2\to 0}$ and $\mathrm{err}_D^{(\mathrm{num})}$ are both Λ and weight dependent through their truncation corrections, their difference $||\mathrm{err}_D^{(\mathrm{num})}||$ is independent of these parameters and it is principally set by $\{c_e, \Lambda^-, \mathcal{U}\}$. The numerical results for $||\mathrm{err}_D^{(\mathrm{num})}||$ at $R = 5$ from Table II are found in very good

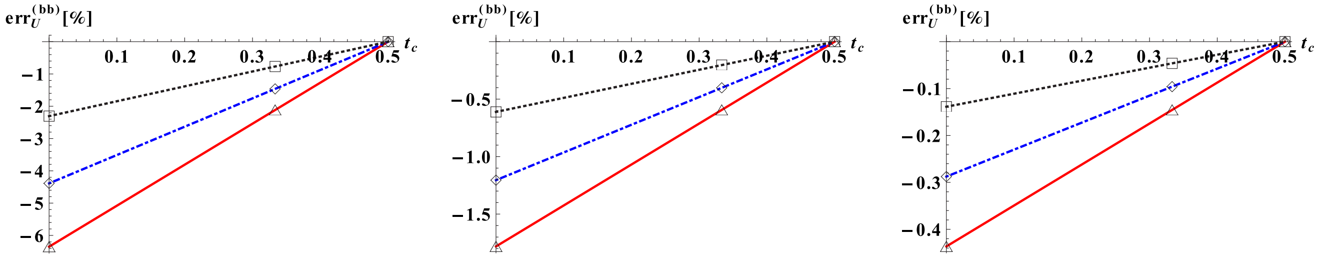

FIG. 11. This figure presents numerical results (lines with symbols) for the relative velocity error $\mathrm{err}_U(t_c^{(a)},\Lambda) - \mathrm{err}_U^{(\mathrm{sum})}$ versus $t_c^{(a)}$, $\mathrm{err}_U = \mathcal{U}^{(\mathrm{num})}/\mathcal{U} - 1$ due to the bounce-back retardation of the Poiseuille profile in cylindrical pipe on the diagonal velocity stencil $\{t_q^{(a)}\}$ for $R = \{5,10,20\}$ from the left to the right. The results are plotted for uniform distribution $\Lambda = \{\frac{1}{12},\frac{1}{6},\frac{1}{4}\}$ [dotted line (black), dotted-dashed line (blue), solid line (red)]. The theoretical prediction for $\mathrm{err}_U^{(bb)}$ is constructed in work [51].

agreement with Eq. (77). The small discrepancy between them can be attributed to discretization effects, not accounted for in Eq. (77). The results from Table II confirm that when Pe, and hence the longitudinal dispersion increases, the numerical diffusion becomes insignificant in err_D because, typically, $c_e(\Lambda^-)^2$ in Eq. (77) decreases rapidly. However, by omitting the U_x^2 term in Eq. (17) at high Pe, the model becomes less stable and it should satisfy a more restrictive stability condition [43], such as $|U|^{\max} \leqslant \sqrt{c_e}$ for any equilibrium weight stencil. Therefore, the U_x^2 term with $t_c^{(u)} = \frac{1}{2}$ is included for all computations below.

3. *Apparent dispersion*

The entire numerical correction to dispersivity $k_T^{(c)}$ is predicted by Eq. (27) as the sum of the three principal components: $\mathrm{err}_D^{(\mathrm{bulk})}$ (bulk), $\mathrm{err}_D^{(bb)}$ (boundary-layer diffusion), and $\mathrm{err}_D^{(bb,U)}$ (boundary-layer dispersion). The mass weight $t_c^{(m)} = \frac{1}{3}$ is first applied for validity of the truncation estimate. Figure 12 displays the four distinguished dispersion-correction components in Eq. (27). They are plotted versus velocity weight $t_c^{(a)}$ in four numerical experiments from Table II (one experiment per row). The numerical values $\mathrm{err}_D^{(\mathrm{num})} = D^{(\mathrm{num})}/(D_0(1+k_T^{(c)})) - 1$ and $\mathrm{err}_D^{(bb)}$ are displayed in the two first diagrams, respectively. The third diagram plots the analytical prediction $\mathrm{err}_D^{(bb,U)}$. The fourth diagram compares $\mathrm{err}_D^{(\mathrm{bulk})} = \mathrm{err}_D^{(\mathrm{num})} - \mathrm{err}_D^{(bb)} - \mathrm{err}_D^{(bb,U)}$ to its analytical prediction $\mathrm{err}_D^{(\mathrm{bulk})} = \mathrm{err}_D^{(\mathrm{tr})} + \mathrm{err}_D^{(\mathrm{sum})}$, predicted by Eqs. (69) and (78).

Summation effect. The component $\mathrm{err}_D^{(\mathrm{sum})}$ is, principally, due to the difference between $\mathcal{U}$ and $\mathcal{U}^{(\mathrm{sum})}(R)$ (specified in Table VI). The key point is that the $k_T^{(\mathrm{sum})}(R)$ in Eq. (63) is computed with $\mathcal{U}^{(\mathrm{sum})}(R)$ by employing the arithmetical averaging over the cross section:

$$\begin{aligned} k_T^{(\mathrm{sum})}(R) &= -\frac{\langle (U_x(r) - \mathcal{U}^{(\mathrm{sum})})\alpha^{(\mathrm{sum})}(r)\rangle}{D_0^2}, \\ \Delta_r\alpha^{(\mathrm{sum})}(r) &= U_x(r) - \mathcal{U}^{(\mathrm{sum})}(R), \\ \mathrm{err}_D^{(\mathrm{sum})}(R) &= \frac{1+k_T^{(\mathrm{sum})}}{1+k_T^{(c)}} - 1 = \frac{k_T^{(c)}}{1+k_T^{(c)}}\delta k_T^{(\mathrm{sum})}(R), \\ \delta k_T^{(\mathrm{sum})}(R) &= \frac{k_T^{(\mathrm{sum})}(R)}{k_T^{(c)}} - 1. \end{aligned} \tag{78}$$

The relative summation correction $\delta k_T^{(\mathrm{sum})}(R)$ is tabulated in Table VI. The correction $\mathrm{err}_D^{(\mathrm{sum})}$ accounts for the discretization effect in the predicted coefficient $k_T^{(c)}$. It is independent of model parameters and set by space resolution R. These results in Table VI illustrate that $\delta k_T^{(\mathrm{sum})}(R)$ does not decay monotonously with R. Moreover, its amplitude, e.g., $\delta k_T^{(\mathrm{sum})}(R=5) \approx 4.6\%$, is comparable with the numerical-diffusion contribution

TABLE V. This table compares the difference in relative dispersion error $||\mathrm{err}_D^{(\mathrm{num})}|| = \mathrm{err}_D^{(\mathrm{num})}|_{U_x^2\to 0} - \mathrm{err}_D^{(\mathrm{num})}$ due to the numerical diffusion with its prediction $||\mathrm{err}_D||$ in Eq. (77). The computations are run with the d3Q15 BB scheme for $R = 5$, Expts. I and IV from Table II. The data are in percents.

Expt. 1, Pe ≈ 2.5					Expt. IV, Pe ≈ 95				
$t_c^{(a)} = t_c^{(m)} = t_c^{(u)} = \frac{1}{2}$					$t_c^{(a)} = t_c^{(m)} = t_c^{(u)} = \frac{1}{2}$				
Λ	$\mathrm{err}_D^{(\mathrm{num})}\vert_{U_x^2\to 0}$	$\mathrm{err}_D^{(\mathrm{num})}$	$\vert\vert\mathrm{err}_D^{(\mathrm{num})}\vert\vert$	$\vert\vert\mathrm{err}_D\vert\vert$	Λ	$\mathrm{err}_D^{(\mathrm{num})}(U_x^2 \to 0)$	$\mathrm{err}_D^{(\mathrm{num})}$	$\vert\vert\mathrm{err}_D^{(\mathrm{num})}\vert\vert$	$\vert\vert\mathrm{err}_D\vert\vert$
$\frac{1}{12}$	−2.274	8.963×10^{-1}	−3.17	−3.23	$\frac{1}{12}$	1.775	2.458	-6.833×10^{-1}	-6.963×10^{-1}
$\frac{1}{6}$	−2.138	1.032	−3.17	−3.23	$\frac{1}{6}$	6.075	6.759	-6.833×10^{-1}	-6.963×10^{-1}
$\frac{1}{4}$	−2.003	1.167	−3.17	−3.23	$\frac{1}{4}$	10.34	11.02	-6.833×10^{-1}	-6.963×10^{-1}
$t_c^{(a)} = t_c^{(m)} = \frac{1}{3},\quad t_c^{(u)} = \frac{1}{2}$					$t_c^{(a)} = t_c^{(m)} = \frac{1}{3},\quad t_c^{(u)} = \frac{1}{2}$				
$\frac{1}{12}$	−6.013	−2.842	−3.17	−3.23	$\frac{1}{12}$	4.701	5.384	-6.833×10^{-1}	-6.963×10^{-1}
$\frac{1}{6}$	−7.139	−3.969	−3.17	−3.23	$\frac{1}{6}$	7.262	7.945	-6.833×10^{-1}	-6.963×10^{-1}
$\frac{1}{4}$	−7.984	−4.814	−3.17	−3.23	$\frac{1}{4}$	9.494	10.18	-6.833×10^{-1}	-6.963×10^{-1}

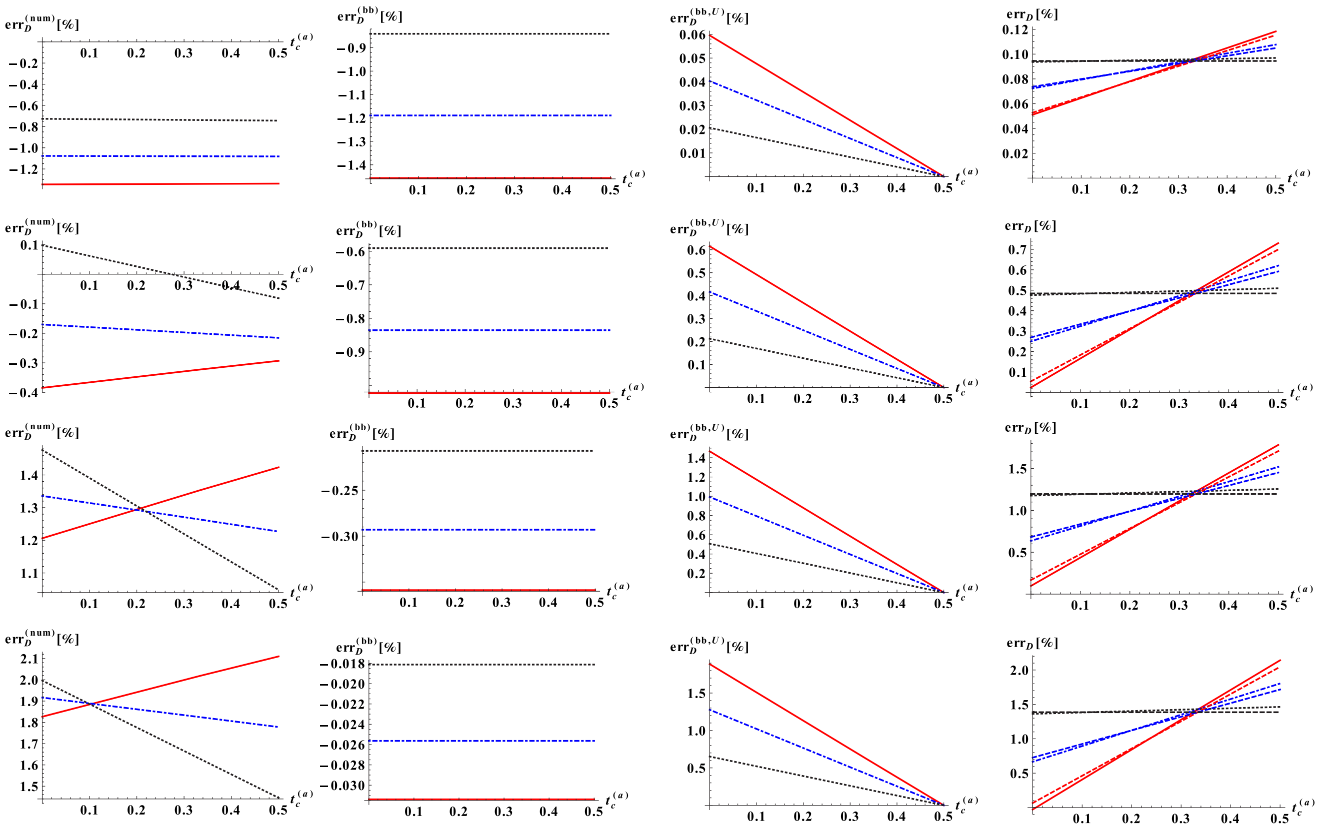

FIG. 12. This figure displays four different components (in row) of the dispersion correction in parabolic flow prescribed in cylindrical capillary of $R = 20$, in four numerical experiments Expts. I–IV (from the top to the bottom), when $\Lambda = \{\frac{1}{12}, \frac{1}{6}, \frac{1}{4}\}$ [dotted line (black), dotted-dashed line (blue), solid line (red)]. First diagram: numerical result $\mathrm{err}_D^{(\mathrm{num})} = D^{(\mathrm{num})}/[D_0(1 + k_T^{(c)})] - 1$ versus velocity weight $t_c^{(a)}$. Second diagram: numerical value of the boundary-layer diffusion correction $\mathrm{err}_D^{(bb)}$ given by Eq. (25). Third diagram: predicted [51] boundary-layer dispersion $\mathrm{err}_D^{(bb,U)}$. Fourth diagram: numerical result for $\mathrm{err}_D^{(\mathrm{bulk})} = \mathrm{err}_D^{(\mathrm{num})} - (\mathrm{err}_D^{(bb)} + \mathrm{err}_D^{(bb,U)})$ (solid lines) and prediction $\mathrm{err}_D^{(\mathrm{bulk})} = \mathrm{err}_D^{(\mathrm{tr})} + \mathrm{err}_D^{(\mathrm{sum})}$ (dashed lines) are plotted together. Further details are given in Table VII; the mass weight $t_c^{(m)} = \frac{1}{3}$ in all simulations.

at small Pe, as $||\mathrm{err}_D^{(\mathrm{num})}|| \approx -3.17\%$ in Table V for Pe ≈ 2.5, and $\mathrm{err}_D^{(\mathrm{sum})}$ exceeds the numerical diffusion at Pe ≈ 95.

Truncation effect. The truncation component $\mathrm{err}_D^{(\mathrm{tr})} = \delta k_T^{(\mathrm{tr})}/(1 + k_T^{(c)})$ in $\mathrm{err}_D^{(\mathrm{bulk})}$ is predicted by Eq. (68). In the numerical validation, $k_T^{(1,c)} = \frac{\langle U'(r)U'(r)\rangle}{D_0^2}$ is also computed via the arithmetical averaging, with $U'(r) = U_x(r) - \mathcal{U}^{(\mathrm{sum})}$, but this effect is very small compared to the principal summation error in Eq. (78). The two effects are captured automatically by the EMM when computing $\gamma'^{(2)}$ in Eq. (72) with $\mathcal{U}^{(\mathrm{sum})}$ and applying the averaging summation procedure in the discretized circular shape.

Boundary-layer diffusion effect due to mass weight $t_q^{(m)}$. When $t_c^{(m)} \neq \frac{1}{2}$, the measured diffusion coefficient differs from the imposed value D_0 by the quantity $\mathrm{err}_D^{(bb)}(t_c^{(m)}, \Lambda, R)D_0$ [cf. Eq. (25)]. The analytical estimate for $\mathrm{err}_D^{(bb)}$ in the capillary is developed in [51]. However, in order to avoid extra discretization corrections, we apply the numerical value $\mathrm{err}_D^{(bb)}(t_c^{(m)}, \Lambda, R)$. It is extracted from the pure-diffusion simulation, as $\mathrm{err}_D^{(bb)} = \frac{D^{(\mathrm{num})}(\mathbf{U}=0) - D_0}{D}$ with given R, Λ, and $t_c^{(m)}$. This result is velocity weight and velocity amplitude independent. It can be adjusted for any nonzero diagonal mass weight $t_d^{(m)}$ since it scales linearly with it. The $\mathrm{err}_D^{(bb)}$ vanishes in d3Q7.

Boundary-layer dispersion effect due to velocity weight $t_q^{(a)}$. The bounce back modifies the parabolic velocity profile in the effective advection process. This manifests in the decrease of mean velocity $\mathcal{U}$ displayed in Fig. 11. The modification results in extra numerical dispersion, due to the superposition of the parabolic and boundary-layer profiles. This deficiency

TABLE VI. This table provides in the first line the relative mean-velocity correction $\mathrm{err}_U^{(\mathrm{sum})}(R) = \mathcal{U}^{(\mathrm{sum})}/\mathcal{U} - 1$ for parabolic velocity profile in the discretized circular shape. In the second line, this table provides the corresponding values $\delta k_T^{(\mathrm{sum})}(R)$ for discrete Taylor-dispersion effect in Eq. (78). The data are in percents.

R	5	10	20	40	80	160
$\mathrm{err}_U^{(\mathrm{sum})}(\%)$	-1.6	-0.54	-0.58	5.3×10^{-2}	-8.9×10^{-3}	-3.4×10^{-2}
$\delta k_T^{(\mathrm{sum})}(\%)$	4.61	1.61	1.74	-1.63×10^{-1}	2.68×10^{-2}	1.01×10^{-1}

TABLE VII. This table provides coefficients c_1–c_4 by fitting $\mathrm{err}_D^{(\mathrm{bulk})} - \mathrm{err}_D^{(\mathrm{sum})}$ to $\mathrm{err}_D^{(\mathrm{tr})} = (c_1 + c_2 t_c^{(a)} + c_3\Lambda + c_4 t_c^{(a)}\Lambda)\frac{k_T^{(1,c)}}{1+k_T^{(c)}}$ in four experiments from Table II. The coefficients are predicted by Eq. (68). Their numerical values are built from four (arbitrarily selected) simulations, with $\{t_c^{(a)},\Lambda\} = \{(0,\frac{1}{4}),(\frac{1}{3},\frac{1}{6}),(\frac{1}{2},\frac{1}{12}),(\frac{1}{2},\frac{1}{6})\}$. The results are illustrated in Fig. 12 for $R = 20$, $t_c^{(a)} = \frac{1}{3}$.

	Expt. I				Expt. II				Expt. III				Expt. IV			
R	c_1	c_2	c_3	c_4	c_1	c_2	c_3	c_4	c_1	c_2	c_3	c_4	c_1	c_2	c_3	c_4
5	0.53	−0.49	−1.7	5.6	0.19	−0.59	−2.4	7.0	0.21	−0.61	−2.5	7.2	0.18	−0.62	−2.6	7.3
10	0.52	−0.51	−2	6.1	0.16	−0.54	−2.2	6.5	0.18	−0.55	−2.2	6.6	0.14	−0.56	−2.2	6.6
20	0.49	−0.47	−2.1	6.2	0.12	−0.48	−2.1	6.3	0.13	−0.48	−2.1	6.3	0.092	−0.48	−2.1	6.4
Theory	0.49	−0.5	−2	6	0.11	−0.5	−2	6	0.12	−0.5	−2	6	0.086	−0.5	−2	6

is accounted for in Eq. (27) and analytically estimated in [51]: this result is demonstrated in the third column diagrams in Fig. 12.

Dispersion results with $t_c^{(m)} = \frac{1}{3}$. On the whole, the numerical results and predictions agree well in Fig. 12 relative to their dependency upon Pe, $t_c^{(a)}$, and Λ. Namely, the bulk results become almost $t_c^{(a)}$ independent for $\Lambda = \frac{1}{12}$, in agreement with Eq. (72) (see the horizontal line in diagrams displayed in the last column). In these bulk results, the "hydrodynamic" choice $t_c^{(a)} = \frac{1}{3}$ is the common point for all Λ. This agrees with the predictions since $\mathrm{err}_D^{(\mathrm{tr})}$ and, hence, $\mathrm{err}_D^{(\mathrm{bulk})}$ becomes Λ independent when $t_c^{(a)} = \frac{1}{3}$ in Eq. (72). Table VII confirms the convergence with the space resolution for $\mathrm{err}_D^{(\mathrm{bulk})} - \mathrm{err}_D^{(\mathrm{sum})}$ towards $\mathrm{err}_D^{(\mathrm{tr})}$, by fitting this difference to Eq. (72). Note, however, the convergence is not monotonous. This is similar with the discretization corrections in velocity and Taylor-dispersion coefficient in Table VI.

It is interesting to examine the evolution of the different components with Pe in Fig. 12. At small Pe ≈ 2.5 (the top row), $\mathrm{err}_D^{(\mathrm{num})}$ is almost $t_c^{(a)}$ independent (first diagram). This is because $\mathrm{err}_D^{(\mathrm{num})} \approx \mathrm{err}_D^{(bb)}$ at small Pe (second diagram) and $\mathrm{err}_D^{(bb)}$ is $t_c^{(a)}$ independent. In turn, the $\mathrm{err}_D^{(bb)}$ linearly increases with the diagonal mass weight $t_d^{(m)} \in [0,\frac{1}{8}]$ [see Eq. (25)]; note, in our computations with $t_c^{(m)} = \frac{1}{3}$, the $t_d^{(m)}$ is relatively small, $t_d^{(m)} = \frac{1}{24}$. On the positive side, the $\mathrm{err}_D^{(bb)}$ decreases as Pe^{-2}. At the same time, as Pe increases, $\mathrm{err}_D^{(bb,U)}(t_c^{(a)})$ (boundary-layer dispersion) becomes asymptotically constant [cf. $\mathrm{err}_D^{(bb,U)}$ for Pe ≈ 25 (third row) and Pe ≈ 95 (fourth row)]. Asymptotically, the $\mathrm{err}_D^{(\mathrm{tr})}$ behaves similar to $\mathrm{err}_D^{(bb,U)}$ since the nondimensional truncation correction $\delta k_T^{(\mathrm{tr})}$ in Eq. (68) scales as Pe^2. Finally, since $\mathrm{err}_D^{(\mathrm{sum})} \approx \delta k_T^{(\mathrm{sum})}$ is Pe independent, the deviation of the numerical result $\mathrm{err}_D^{(\mathrm{num})}$ from the physical value becomes asymptotically constant and mainly caused by $\mathrm{err}_D^{(bb,U)}$ and $\mathrm{err}_D^{(\mathrm{sum})}$. In these simulations, $\mathrm{err}_D^{(\mathrm{num})} \in]0,2\%]$ at Pe ≈ 95 while $\delta k_T^{(\mathrm{sum})}(R = 20) = 1.74\%$ (cf. Table VI). Finally, we suggest that the relatively slight difference between the numerical result and prediction is mainly due to the $\mathrm{err}_D^{(bb,U)}$ estimate [51] which does not account for the entire discretization effect.

Dispersion results with $t_c^{(m)} = \frac{1}{2}$. Figure 13 addresses the same four numerical experiments as in Fig. 12 but applying the mass weight $t_c^{(m)} = \frac{1}{2}$. This choice is predicted to give the anisotropic fourth-order diffusion correction in Eq. (64), except for $\Lambda = \frac{1}{6}$. At the same time, numerical computations in the pure-diffusion case confirm that $D^{(\mathrm{num})}(t_c^{(m)} = \frac{1}{2}) \equiv D_0$ and, hence, $\mathrm{err}_D^{(bb)} = 0$, $\mathrm{err}_D^{(\mathrm{bulk})} = \mathrm{err}_D^{(\mathrm{num})} - \mathrm{err}_D^{(bb,U)}$. Figure 13 compares $\mathrm{err}_D^{(\mathrm{bulk})}$ to its prediction in Eq. (27). We observe that an agreement deteriorates against the case with $t_c^{(m)} = \frac{1}{3}$ in Fig. 12 (see the last column there), except for $\Lambda = \frac{1}{6}$ where prediction $\mathrm{err}_D^{(\mathrm{tr})}$ remains valid with $t_c^{(m)} = \frac{1}{2}$. When $\Lambda = \frac{1}{12}$ and $\frac{1}{4}$, the deviation from the theoretical result in Fig. 12 has a similar form in four experiments. The fitting of these numerical data to $\mathrm{err}_D^{(\mathrm{tr})}$, similar to Table VII, gives $c_3(t_c^{(m)} = \frac{1}{2}) = -2.4$ in the four experiments, against $c_3(t_c^{(m)} = \frac{1}{3}) = -2.1$ and theoretical estimate $c_3^{th} = -2$. These results suggest that the anisotropic fourth-order effect is present and observable in the apparent dispersion.

Dispersion results with d3Q7. In d3Q7, the bounce-back boundary effects vanish and it is expected that $\mathrm{err}_D = \mathrm{err}_D^{(\mathrm{bulk})}$. The results above indicate that although the truncation result given by Eq. (68) is less accurate when $t_c^{(m)} \neq \frac{1}{3}$, it provides the reasonable estimate. Moreover, Fig. 13 shows a very good agreement in all four experiments in case of $t_c^{(m)} = t_c^{(a)} = \frac{1}{2}$ for $\Lambda = \frac{1}{4}$. We confirm this observation on the independent recent results [12]. The investigation [12]

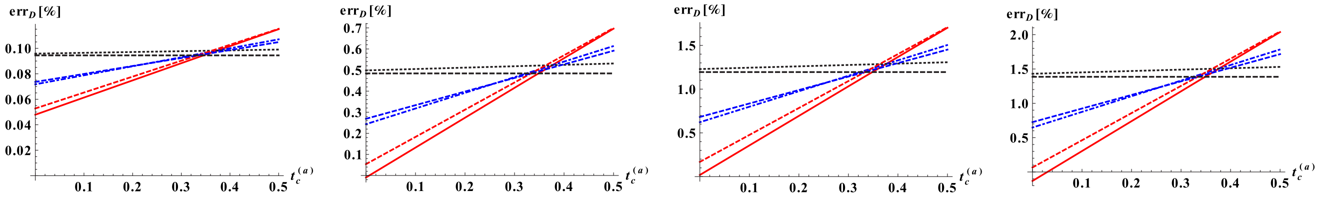

FIG. 13. This figure demonstrates the effect of the anisotropic (except for $\Lambda = \frac{1}{6}$) truncation dispersion component in numerical results, when $\Lambda = \{\frac{1}{12},\frac{1}{6},\frac{1}{4}\}$ [dotted line (black), dotted-dashed line (blue), solid line (red)]. The four diagrams are similar to the last column in Fig. 12 but the (anisotropic) coordinate mass weight $t_c^{(m)} = \frac{1}{2}$ is applied in computations.

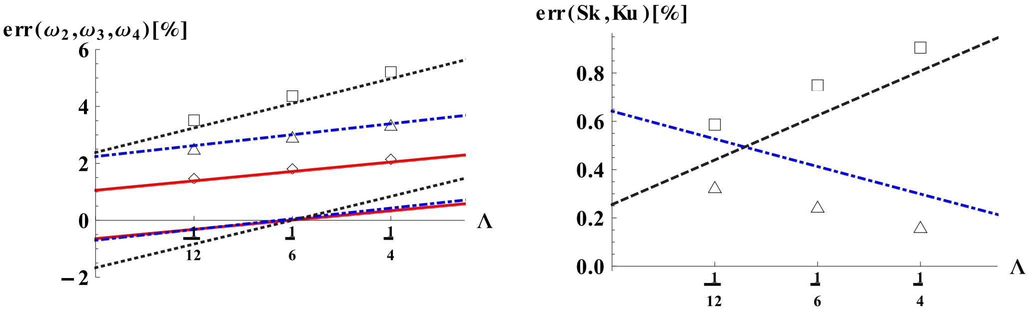

FIG. 14. Cylindrical pipe of $R=20$, Expt. IV, $t_c^{(m)}=\frac{1}{3}$, $t_c^{(a)}=\frac{1}{2}$, uniform-Λ distribution. The first diagram compares numerical results in the form of Eq. (24) (symbols) to their truncation predictions for ω_2 [solid line (red), "lozenges"], ω_3 [dashed line (blue), "triangles"], and ω_4 [dotted line (black), "square"]. The predictions are obtained with the EMM using either summation in given geometry with $\mathcal{U}\rightarrow\mathcal{U}^{(\text{sum})}$ (thick lines) or integration over the exact circular shape (the thin lines bisecting at $\Lambda=\frac{1}{6}$). The second diagram displays numerical and EMM summation results for $\text{Sk}_\star$ [dashed line (blue), "triangles"] and $\text{Ku}_\star$ [dotted line (black), "squares"].

applies the d3Q7 TRT-ADE scheme with $\Lambda=\frac{1}{4}$ in the Herschel-Buckley velocity profile prescribed in the cylindrical capillary, and reports a very good accordance between the numerical and analytical results for the Taylor-dispersion coefficients predicted there. In detail, in case of the Newtonian (parabolic profile) at $\text{Pe}=50$, where the steady-state value of the Taylor-dispersion coefficient was reached (see Fig. 8 and Table I [12], with $c_e=0.08$, $\Lambda^-=0.0625$, $\Lambda=\frac{1}{4}$, $\mathcal{U}=5\times10^{-3}$, $R=25.5$), the obtained velocity and dispersion errors are, respectively, $\text{err}_U=0.524026\%$ and $\text{err}_D\approx-1.22378\%$ (private communications). We note that $\text{err}_U\equiv\text{err}_U^{(\text{sum})}(R=25.5)$, which has been predicted for d3Q7, and our estimate (27) gives $\text{err}_D\approx-1.262\%$ [with $\text{err}_D^{(\text{tr})}\approx0.1897\%$, $\text{err}_D^{(\text{sum})}\approx-1.45175\%$, $\delta k_T^{(\text{sum})}\approx-1.5589\%$ in Eq. (78)]. This confirms that Eq. (68) works quite satisfactorily in d3Q7 with $\Lambda=\frac{1}{4}$. Again, these results clearly demonstrate that the summation component may dominate the truncation one, even for relatively large R.

4. *Skewness and kurtosis*

Our last objective is to verify the truncation prediction for $\text{Sk}_\star^{(\text{tr})}$ and $\text{Ku}_\star^{(\text{tr})}$ in Eq. (73). It is observed that the diffusion boundary-layer effect due to the isotropic mass weight $t_c^{(m)}=\frac{1}{3}$ destroys the truncation results for $\text{Sk}_\star^{(\text{tr})}$ and $\text{Ku}_\star^{(\text{tr})}$ at relatively small Pe, similarly as in Table IV for plug flow. At the same time, fine validation fails for $t_c^{(m)}=\frac{1}{2}$ because of the anisotropic effects, similar to Fig. 13 for numerical dispersion. Due to these reasons, we only present results for $\text{Pe}\approx95$ with $t_c^{(m)}=\frac{1}{3}$. In order to avoid boundary-layer velocity effect, we restrict this analysis to $t_c^{(a)}=\frac{1}{2}$ where $\mathcal{U}^{(\text{num})}=\mathcal{U}^{(\text{sum})}$. Figure 14 compares (in the first diagram) numerical solutions for $\omega^{(2,\text{num})}$, $\omega^{(3,\text{num})}$, and $\omega^{(4,\text{num})}$, computed with Eq. (24), against their symbolic solutions derived in Sec. IV C. Notice that the analysis of the set $\{\omega^{(n)}\}$ excludes their superposition effect presented in $\text{Sk}_\star$ and $\text{Ku}_\star$. The velocity amplitude is increased by the factor of 4 in Fig. 15 towards $|U|^{\max}=\sqrt{c_e}=\sqrt{\frac{1}{30}}$. The two sets of the EMM predictions are examined: either by using integration procedure with predicted velocity $\mathcal{U}$ or by using the discrete-summation procedure with the actual velocity distribution $\mathcal{U}^{(\text{num})}(t_c^{(a)}=\frac{1}{2})=\mathcal{U}^{(\text{sum})}$. We observe that the amplitude of the difference between the two average procedures is quite comparable with the truncation error. The numerical results agree very well with the summation-based EMM prediction. However, unlike for the "integration" prediction, the optimal choice $\Lambda(t_c^{(a)}=\frac{1}{2})=\frac{1}{6}$ is not the most accurate because of the summation effect; actually, the numerical and predicted (summation) errors have no optimal positive root for Λ.

The relative differences err(Sk) and err(Ku) (with respect to $\text{Sk}_\star$ and $\text{Ku}_\star$ from Table I at $\text{Pe}\approx95$) are compared for numerical results $\{\text{Sk}_\star^{(\text{num})},\text{Ku}_\star^{(\text{num})}\}$ and theoretical predictions $\{\text{Sk}_\star^{(\text{tr})},\text{Ku}_\star^{(\text{tr})}\}$ in the second diagrams in Figs. 14 and 15. They depend differently on Λ because of two distinguished values c_e. Here, the summation-based EMM estimate replaces Eq. (73). First, we note that the entire numerical and truncation corrections are relatively small for $\{\text{Sk}_\star,\text{Ku}_\star\}$ at this regime of Pe: their magnitude is less than 1% over the entire interval $\Lambda\in[\frac{1}{12},\frac{1}{4}]$. In agreement with Figs. 8 and 9 for channel

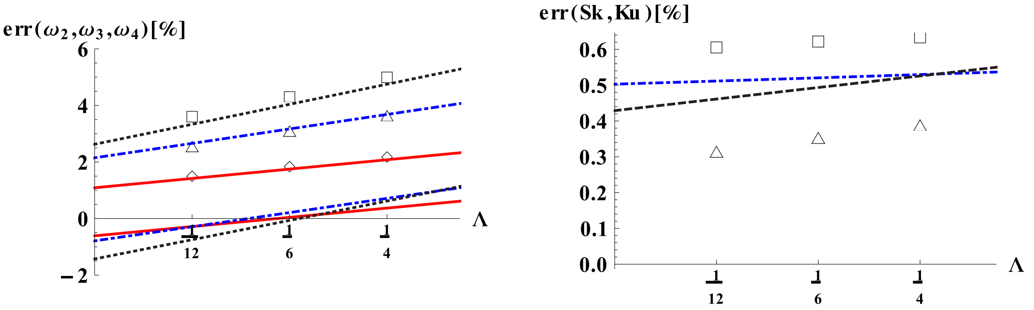

FIG. 15. Cylindrical pipe of $R=20$, Expt. IV, $t_c^{(m)}=\frac{1}{3}$, $t_c^{(a)}=\frac{1}{2}$. Similarly as in Fig. 15 but increasing $\mathcal{U}$ by factor of 4 at fixed Pe.

at the same Pe, the present simulations confirm that the coordinate velocity weight $t_c^{(a)} = \frac{1}{2}$ assures good accuracy in numerical measurements of skewness and kurtosis. The results confirm that their principal dependency on c_e, Λ^-, Λ, and weights is matched well. A very small (parallel) shift from the prediction in Figs. 14 and 15 is probably related to some further summation effect. These results confirm that the diffusion boundary-layer effect $\text{err}_D^{(bb)}$ becomes negligible for skewness and kurtosis, same way as for dispersion, already at intermediate Péclet number.

E. Summary

In this section, the effective bulk solutions for dispersion, skewness, and kurtosis were predicted by Eqs. (72) and (73) for Poiseuille flow in the cylindrical capillary. This is achieved by extending the EMM approach [15] to the three-dimensional, fourth-order-accurate equation of the TRT scheme. The EMM-based estimate of the numerical dispersion coincides with the Taylor argument based truncation result presented in Eq. (68). The isotropic mass weight, which is $t_c^{(m)} = \frac{1}{3}$ in d3Q15, is required (except for $\Lambda = \frac{1}{6}$) for the fourth-order isotropy and the rigorous validity of the truncation analysis. The truncation dispersion estimate approximately applies when $t_c^{(m)} \neq \frac{1}{3}$, and in particular for d3Q7. It can be applied for any open-tabular flow, Newtonian or non-Newtonian, by computing $k_T^{(1,c)} = \frac{\langle U'(\boldsymbol{r})U'(\boldsymbol{r})\rangle}{D_0^2}$ in Eq. (68) for the actual velocity field $U'(\boldsymbol{r}) = U_x(\boldsymbol{r}) - \mathcal{U}^{(\text{sum})}$, $\mathcal{U}^{(\text{sum})} = \langle U_x(\boldsymbol{r})\rangle$. The coefficient K in Eq. (68), and hence the functional dependency of truncation dispersion over model parameters c_e, Λ^-, Λ, and weights is flow independent. Therefore, similar conclusions as in straight channel apply for the optimal dispersion parameter choice in the cylindrical capillary. Namely, the isotropic velocity weight $t_c^{(a)} = \frac{1}{3}$ makes the truncation dispersion $\delta k_T^{(\text{tr})}$ in Eq. (68) Λ independent but nonvanishing. On the other side, when $t_c^{(a)} \in [0, \frac{1}{6}]$ or when $t_c^{(a)} \in]\frac{1}{3}, \frac{1}{2}]$, one may vanish $\delta k_T^{(\text{tr})}$ in the limit $c_e(\Lambda^-)^2 \to 0$ with the specific solution $\Lambda(t_c^{(a)})$ given by Eq. (69). When $t_c^{(a)} = \frac{1}{2}$, $\Lambda = \frac{1}{6}$ (best), but also $\Lambda = \frac{1}{4}$, support good truncation accuracy for all transport coefficients within the intermediate and high Pe range. Also, $\Lambda = \frac{1}{4}$ makes Sk and Ku independent of c_e when Λ^- decreases to zero [cf. Eq. (74)]. The $\Lambda = \frac{1}{12}$ makes the three transport coefficients velocity weight independent but has relatively poor stability even with the most stable weight stencils and the hydrodynamic weights [35,44].

It has been verified that the second-order numerical diffusion is removed in duct flow with Eq. (17). For numerical validation, the EMM predictions were all computed in a given pipe geometry, with account for actual velocity $\mathcal{U}^{(\text{sum})}(R)$. The truncation dispersion was complemented by the summation and discretization correction $k_T^{(\text{sum})}$ in Eq. (78). The boundary-layer, velocity and dispersion, bounce-back corrections both vanish for $t_c^{(a)} = \frac{1}{2}$. The boundary-layer diffusion correction vanishes for $t_c^{(m)} = \frac{1}{2}$. All bounce-back spurious effects vanish for the d3Q7 scheme, and this property is suggested [51] to be valid in grid-aligned ducts of different cross section. Otherwise, the bulk dispersion estimate should be summed with the boundary-layer diffusion and dispersion corrections. In this work, the numerical estimate for the boundary-layer diffusion and analytical estimate [51] for boundary-layer dispersion have been employed. The boundary-layer diffusion has strong effect in dispersion, skewness, and kurtosis at small Pe, but it becomes insignificant as Pe increases. In turn, the relative contribution of the truncation and boundary-layer dispersion is asymptotically constant. The double-Λ TRT scheme [51] allows to restore correct velocity and to (almost) vanish boundary-layer dispersion, for any velocity weight and without any modification of the bounce-back rule. It will allow [51] us to extend numerical validation of $\text{Sk}_\star$ and $\text{Ku}_\star$ truncation analysis in a capillary for $t_c^{(a)} \neq \frac{1}{2}$ and smaller Pe.

V. CONCLUDING REMARKS

A mathematical algorithm for the prediction of the second-, third-, and fourth-order moments of the solute distribution has been proposed. We start with the fourth-order-accurate truncation form of the modeled advection-diffusion equation and apply the idea of the extended method of moments (EMM) [15]. The analytical procedure was worked out for pure diffusion, plug and parabolic flows in straight channel, and extended for parabolic profile in cylindrical capillary. The closed-form results were derived for the apparent coefficients of the Taylor dispersivity k_T, skewness $\text{Sk}_\star$, and kurtosis $\text{Ku}_\star$ in the full parameter space of the given numerical scheme. Further, the summation effect in the effective velocity and transport coefficients due to the collocated grid and the staircase approximation of the shaped boundary was accounted by performing all average EMM operators over the discretized cross section. This procedure readily extends to other (Newtonian or non-Newtonian) advective profiles in pipes of general cross section [14]. We believe that the duct geometry is sufficient to determine the principal dependency of the numerical moments upon the adjustable parameters, Péclet number, and mesh resolution. Being exemplified with the two-relaxation-times TRT-ADE scheme, where the generic form of the truncation corrections has been derived [35,41], our approach readily applies for any other numerical scheme providing its truncation terms are specified. In particular, we believe that after constraining the procedure and results to $\Lambda = \frac{1}{4}$, the fourth-order-accurate approximation and the bulk EMM predictions apply for the LFCCDF finite-difference schemes [58], and perhaps, also for their finite-volume or finite-elements counterparts on regular grid.

It has been established that the relative truncation effect diminishes with the second-order accuracy in all three coefficients. Their role in k_T, $\text{Sk}_\star$, and $\text{Ku}_\star$ becomes Pe independent as Pe increases: the results demonstrated in this work for $\text{Pe} \approx 10^2$ apply for higher Pe. In the limit $\Lambda^- \to 0$, $\text{Sk}_\star$ and $\text{Ku}_\star$ become independent of the diffusion coefficient with $\Lambda = \frac{1}{4}$, in relation to the advanced stability of this choice [35,43,44]. The closed-form result for the truncation correction $\delta k_T^{(\text{tr})}$ to the Taylor-dispersivity coefficient k_T in straight channel and cylindrical capillary confirms the suggestion in [41] that its principal dependency upon the equilibrium and relaxation parameters [given by function K in Eqs. (46) and (68)] is flow and dimension independent. Formally, this truncation result requires the hydrodynamic mass weight in cylindrical capillary for the isotropy of the fourth-order diffusion form. However, we have shown that it describes rather accurately the numerical dispersion of the coordinate mass-weight stencil and can be readily extended for the estimation of the truncation and discretization corrections in dispersion measurements [12] in Herschel-Bulkley capillary profile, operated with the d3Q7 TRT bounce-back scheme at $\Lambda = \frac{1}{4}$. We confirm that the combination of the coordinate velocity weight with $\Lambda = \frac{1}{4}$ is quite suitable in straight channel and cylindrical capillary, and it is supported by reliable stability criteria [41,43]; however, the most accurate choice on the coordinate velocity stencil for k_T, $\mathrm{Sk}_\star$, and $\mathrm{Ku}_\star$ is $\Lambda = \frac{1}{6}$. On the other hand, the hydrodynamic velocity weight releases $\delta k_T^{(\mathrm{tr})}$ from the Λ dependency; however, this property does not extend to the skewness and kurtosis. In turn, $\Lambda = \frac{1}{12}$ makes the three transport coefficients velocity weight independent and avoids their very strong increase (on coarse mesh) with the diagonal weight value. Yet, the choice $\Lambda = \frac{1}{12}$ has poor stability properties at high Pe [44]. The mass-weight stencil can be prescribed independently of the velocity weight, but Ku depends on it except with the "optimal diffusion" choice $\Lambda = \frac{1}{6}$; this dependency is, however, weak at high Pe and vanishes asymptotically. At small Pe, the apparent coefficients are not set by Pe, Λ, and weights because, in addition, they noticeably depend on two individual parameters c_e and Λ^-, at fixed molecular-diffusion coefficient $D_0 = c_e\Lambda^-$. However, since the physical values of the high-order moments are small, even the relatively significant truncation corrections do not impact noticeably the distribution profiles within small Pe range.

In straight channel, a quasi-exact validation of the truncation predictions through first four numerical moments becomes possible thanks to the specular-forward reflection on solid walls. However, in the advection-diffusion spread through the open-tubular conduit, the nonequilibrium boundary layers of the bounce-back no-flux rule affect the two primary characteristics of the averaged solute distribution, its diffusion coefficient and mean-velocity, in proportion to the diagonal mass and velocity weight, respectively. Consequently, the numerical values of the transport coefficients are especially affected by the velocity weight at intermediate and high Pe, while at small Pe, they become very sensitive to the mass-weight choice, on top of the truncation dependency. We emphasize that only the d3Q7 scheme is free from these spurious boundary effects in grid-aligned conduits. In order to verify the dispersion truncation prediction in cylindrical capillary in full weight space, the boundary-layer diffusion and dispersion were subtracted from the numerical results. The relative boundary-layer diffusion component was extracted from the independent pure-diffusion simulation in a given geometry; the symbolic estimate [51] was called as boundary-layer dispersion. Because of the spurious bounce-back effects, we could verify the truncation predictions for skewness and kurtosis in cylindrical capillary only for the coordinate velocity weight and relatively high Pe. The double-Λ scheme, developed in the conjoined work [51], allows to preserve the advection profile in duct flow and to further extend the Pe range and weight interval of the numerical assessment.

This work was restricted to isotropic advection-diffusion equation. The TRT-ADE schemes [29,34,35] create the anisotropy with the help of the anisotropic full-weight mass stencil. This feature allows the TRT-ADE to operate with the anisotropy-independent relaxation rates and to fix Λ for the sake of accuracy or stability [35,45]. Since the truncation coefficients are expressed via the relaxation rates alone, we expect their preselected optimal solutions to be valid in anisotropic TRT-ADE schemes for the same purpose. This also concerns the TRT-ADE schemes [15,29] for heterogeneous porous soil; in these schemes, while Λ^- varies with the heterogeneity, the Λ remains free. However, future work is required to estimate impact of the implicit or explicit interface conditions on the Taylor dispersion and the high-order moments. Further, the MRT-ADE schemes with the multiple-relaxation-times operators [34,37,49,64,65] for isotropic-diffusion inherit the present results by reducing their free relaxation rates to the TRT configuration. We note that the exact von Neumann stability analysis [45] shows that their additional degrees of freedom only marginally enlarge the stable isotropic-diffusion parameter space, but they may degrade it drastically for an improper choice. Moreover, their necessary stability conditions are expected to be sufficient mostly only for $\Lambda = \frac{1}{4}$, thus reducing the MRT to TRT. On the other hand, the anisotropic relaxation approaches [29,34,49] operate with the disparate Λ combinations and can hardly improve for stability or accuracy with their help [29,45].

Finally, although only illustrated on spatial dispersion, our methodology also applies for the resident time distributions of a tracer because the two systems of moments, spatial and temporal, are easily interconnected [15]. When comparing the numerical results to experimental data, one has to bear in mind three possible pitfalls, namely, numerical error, deficiency of the model, and experimental noise. This work suggests that the optimized TRT scheme is a suitable candidate for predictions of the dispersion and higher-order moments at intermediate and high Pe range and, therefore, it allows for experimental model refinement and assessment of the accuracy of the measurements.

ACKNOWLEDGMENT

The author is grateful to G. Silva and A. Vikhansky for critical reading of the manuscript, and thanks ANR for funding the project LaboCothep through Grant No. ANR-12-MONU0011.

APPENDIX A: SUMMARY ON TRUNCATION ANALYSIS

1. Fourth-order-accurate advection-diffusion equation: Generic form

We assume linear equilibrium distribution with respect to the local mass value $C(\boldsymbol{r},t)$: $e_q^{\pm} = E_q^{\pm}C$, $\sum_{q=0}^{Q_m} E_q^+ = 1$, $E_q^+ = E_q^+(c_e,\boldsymbol{U})$, and $E_q^- = E_q^-(\boldsymbol{U})$, $q = 0,\ldots,Q_m$. The distribution $\{E_q^+\}$ can be either isotropic or anisotropic [35] and, in particular, given by Eq. (17) for modeling of the isotropic ADE. The exact form of the mass-conservation equation of the TRT scheme is given by Eq. (22). Its fourth-order-accurate d-dimensional approximation is derived [35,41] in the form

$$\partial_t C(\boldsymbol{r},t) = [R_1 + R_2 + R_3 + R_4]C(\boldsymbol{r},t). \tag{A1}$$

In this relation, the four operators $[R_k]C$ are expressed via the two families of the differential operators $[S_{2k}]C$ and $[S_{2k-1}]C$:

$$[S_{2k}]C = \left[\sum_{q=1}^{Q_m} \partial_q^{2k} E_q^+\right]C, \quad [S_{2k-1}]C = \left[\sum_{q=1}^{Q_m} \partial_q^{2k-1} E_q^-\right]C, \quad \text{with } \partial_q = (\boldsymbol{\nabla}\cdot\boldsymbol{c}_q) = \sum_{\alpha=1}^{d} \partial_\alpha c_{q\alpha}, \quad k = 1,2. \tag{A2}$$

Hereby, $\partial_q^n C$ denotes the nth-order directional derivative; $[S_k^n]C$ means that the operator S_k applies n times to $C(\boldsymbol{r},t)$. At the second order, Eq. (A1) reads as

$$[R_1]C = -[S_1]C, \quad [S_1]C = \nabla\cdot\boldsymbol{U}C, \quad [R_2]C = \Lambda^-[D_2]C, \quad [D_2]C = [S_2]C - [S_1^2]C. \tag{A3}$$

The third-order truncation correction $[R_3]C$ reads as

$$[R_3]C = c_{3,1}[S_1D_2]C + c_{3,2}\big[S_1^3 - S_3\big]C, \quad c_{3,1}(\Lambda^-,\Lambda) = 2(\Lambda^-)^2 + \Lambda - \frac{1}{4}, \quad c_{3,2}(\Lambda) = \Lambda - \frac{1}{12}, \tag{A4}$$

$$c_{3,1} = 0, \quad c_{3,2} = 0 \ \text{ if } \ (\Lambda^-)^2 = \Lambda = \frac{1}{12}, \quad \text{ or } \ \Lambda^- = \Lambda^+ = \sqrt{\frac{1}{12}}. \tag{A5}$$

Thus, the most accurate advection scheme where the entire third-order truncation correction vanishes is presented by the single-relaxation-time combination (A5). The fourth-order truncation term $[R_4]C$ reads as [we signalize a typo in Eq. (2.10) from [35] for $c_{4,4}$]

$$\begin{aligned}
[R_4]C &= c_{4,1}\big[D_2^2\big]C + c_{4,2}\big[S_1^2D_2\big]C + c_{4,3}[S_4 - S_1S_3]C + c_{4,4}\big[S_1^4 - S_1S_3\big]C,\\
c_{4,1}(\Lambda^-,\Lambda) &= -\Lambda^-\left[(\Lambda^-)^2 + \Lambda - \frac{1}{4}\right], \quad c_{4,2}(\Lambda^-,\Lambda) = \Lambda^-\left[4(\Lambda^-)^2 + \Lambda - \frac{3}{4} + \frac{\Lambda(4\Lambda-1)}{4(\Lambda^-)^2}\right],\\
c_{4,3}(\Lambda^-,\Lambda) &= \Lambda^-\left(\Lambda - \frac{1}{6}\right), \quad c_{4,4}(\Lambda^-,\Lambda) = \frac{\Lambda^-}{4}\left[8\Lambda - 1 + \frac{\Lambda(4\Lambda-1)}{(\Lambda^-)^2}\right].
\end{aligned} \tag{A6}$$

In the pure-diffusion case, the odd-order operators vanish and the modeled fourth-order-accurate equation reads as

$$\partial_t C = \Lambda^-[S_2]C + [R_4]C, \quad \text{with } [R_4]C = c_{4,1}\big[S_2^2\big]C + c_{4,3}[S_4]C, \tag{A7}$$

$$c_{4,1} = 0, \quad c_{4,3} = 0 \ \text{ if } \ \Lambda = \tfrac{1}{6}, \quad (\Lambda^-)^2 = \tfrac{1}{12}. \tag{A8}$$

Hence, the most accurate pure-diffusion scheme is presented by the two-relaxation-times TRT combination (A8). There exist the intrinsic relations [35] between the truncation corrections and advanced stability revealed in [44].

APPENDIX B: DETAILED DERIVATION OF TRUNCATION CORRECTIONS FOR $\Lambda = \frac{1}{4}$

When $\Lambda = \frac{1}{4}$, Eq. (22) takes the form of the finite-difference scheme:

$$\Lambda = \Lambda^-\Lambda^+ = \frac{1}{4} : \bar{\Delta}_t C + \Lambda^-\bar{\Delta}_t^2 C = -\sum_{q=1}^{Q_m}\bar{\Delta}_q e_q^- + \Lambda^-\sum_{q=1}^{Q_m}\bar{\Delta}_q^2 e_q^+. \tag{B1}$$

Let us illustrate the procedure [35,41] for generic derivation of Eqs. (A1)–(A6) in case of the channel advective flow $\boldsymbol{U} = U_x(y)$ and the d2Q5 scheme with $\Lambda = \frac{1}{4}$. In channel flow, the d2Q5 scheme (19) reads as $e_q^+(\boldsymbol{r},t) = \frac{1}{2}(c_e + U_x^2 c_{qx}^2)C(\boldsymbol{r},t)$ and $e_q^- = \frac{1}{2}U_x(y)C(\boldsymbol{r},t)c_{qx}$. Assume that scale parameter c_e is space and time independent. We make use of the following auxiliary functions applied to grid solution $C(\boldsymbol{r},t)$ within the d2Q5 scheme:

$$\begin{aligned}
&\bar{\Delta}_t C = \partial_t C + \frac{1}{6}\partial_t^3 C, \quad \bar{\Delta}_t^2 C = \partial_t^2 C + \frac{1}{12}\partial_t^4 C,\\
&\sum_{q=1}^{Q_m}\bar{\Delta}_q e_q^- = U_x(y)\bar{\Delta}_x C \approx U_x(y)\left(\partial_x C + \frac{1}{6}\partial_x^3 C\right),\\
&\Lambda^-\sum_{q=1}^{Q_m}\bar{\Delta}_q^2 e_q^+ = \Lambda^-\left(\sum_{q=1}^{Q_m}\partial_q^2 e_q^+ + \frac{1}{12}\sum_{q=1}^{Q_m}\partial_q^4 e_q^+\right), \quad \text{with}\\
&\sum_{q=1}^{Q_m}\partial_q^2 e_q^+ = c_e\Delta^2 C + U_x^2\partial_x^2 C, \quad \partial_q^2 = (\partial_x c_{qx} + \partial_y c_{qy})^2, \quad \Delta^2 C = \big[\partial_x^2 + \partial_y^2\big]C,\\
&\sum_{q=1}^{Q_m}\partial_q^4 e_q^+ = c_e\Delta^4 C + U_x^2\partial_x^4 C, \quad \partial_q^4 = (\partial_x c_{qx} + \partial_y c_{qy})^4, \quad \Delta^4 C = \big[\partial_x^4 + \partial_y^4\big]C.
\end{aligned} \tag{B2}$$

With their help, the fourth-order-accurate spatial component in the right-hand side of Eq. (B1), $[R^{(S)}]C$ reads as

$$[R^{(S)}]C = -\sum_{q=1}^{Q_m}\bar{\Delta}_q e_q^- + \Lambda^-\sum_{q=1}^{Q_m}\bar{\Delta}_q^2 e_q^+ = \sum_{i=1}^{4}\big[R_i^{(S)}\big]C, \quad \text{with } \big[R_1^{(S)}\big]C = -U_x(y)\partial_x C,$$

$$\big[R_2^{(S)}\big]C = \Lambda^-\big(c_e\Delta^2 C + U_x^2\partial_x^2 C\big), \quad \big[R_3^{(S)}\big]C = -\frac{1}{6}U_x(y)\partial_x^3 C, \quad \big[R_4^{(S)}\big]C = \frac{\Lambda^-}{12}\big(c_e\Delta^4 C + U_x^2\partial_x^4 C\big). \tag{B3}$$

In what follows, we express all time derivatives $\partial_t^k C$ via the spatial derivatives, with the help of the previous order approximation of Eq. (B1). The $[\partial_t^k C]^{(n)}$ then denotes the nth-order component. The sequential approximations read as, with the help of Eqs. (B3),

$$\text{order } 1: \partial_t C = [R_1]C, \quad [R_1]C = \big[R_1^{(S)}\big]C = -U_x(y)\partial_x C;$$

$$\text{order } 2: \partial_t C = [R_1]C + [R_2]C, \quad [R_2]C = \big[R_2^{(S)}\big]C - \big[\Lambda^-\partial_t^2 C\big]^{(2)} \text{ with } \partial_t^2 C = U_x^2\partial_x^2 C, \quad \text{then } [R_2]C = c_e\Lambda^-\Delta^2 C;$$

$$\text{order } 3: \partial_t C = [R_1 + R_2 + R_3]C, \quad [R_3]C = \big[R_3^{(S)}\big]C - \Lambda^-\big[\partial_t^2 C\big]^{(3)} - \frac{1}{6}\big[\partial_t^3 C\big]^{(3)}, \quad \text{with}$$

$$\big[\partial_t^2 C\big]^{(3)} = [(R_1 + R_2)^2]^{(3)}C = [2R_1R_2]C, \quad \big[\partial_t^3 C\big]^{(3)} = \frac{1}{6}U_x^3\partial_x^3 C, \quad \text{then}$$

$$[R_3]C = -\frac{1}{6}U_x(y)\partial_x^3 C + 2(\Lambda^-)^2 c_e U_x(y)\partial_x(\Delta^2 C) + \frac{1}{6}U_x^3\partial_x^3 C;$$

$$\text{order } 4: \partial_t C = [R_1 + R_2 + R_3 + R_4]C \text{ where } [R_4]C = \big[R_4^{(S)}\big]C - \Lambda^-[\partial_t^2 C]^{(4)} - \frac{1}{6}\big[\partial_t^3 C\big]^{(4)} - \frac{\Lambda^-}{12}[\partial_t^4 C]^{(4)}, \quad \text{with}$$

$$\big[\partial_t^2 C\big]^{(4)} = \big[R_2^2 + 2R_1R_3\big]C = c_e^2(\Lambda^-)^2[\Delta^2]^2 C - 2U_x(y)\partial_x\bigg[-\frac{1}{6}U_x(y)\partial_x^3 C + 2(\Lambda^-)^2 U_x(y)\partial_x(c_e\Delta^2 C) + \frac{1}{6}U_x^3\partial_x^3 C\bigg],$$

$$\big[\partial_t^3 C\big]^{(4)} = 3\big[R_1^2 R_2\big]C = 3c_e\Lambda^- U_x^2\partial_x^2\Delta^2 C, \quad \big[\partial_t^4 C\big]^{(4)} = U_x^4\partial_x^4 C, \quad \text{then}$$

$$\begin{aligned}[R_4]C = {}& \frac{\Lambda^-}{12}c_e\Delta^4 C - \Lambda^- c_e^2(\Lambda^-)^2[\Delta^2]^2 C + U_x^2\bigg[\frac{\Lambda^-}{12}\partial_x^4 C - \frac{\Lambda^-}{3}\partial_x^4 C + 4\Lambda^-(\Lambda^-)^2 c_e\partial_x\Delta^2 C - \frac{1}{2}c_e\Lambda^-\partial_x^2\Delta^2 C\bigg] \\ & + U_x^4\bigg(-\frac{\Lambda^-}{12}\partial_x^4 C + \frac{\Lambda^-}{3}\partial_x^4 C\bigg).\end{aligned} \tag{B4}$$

Thus, Eqs. (B4) give the third-order ($[R_3]C$) and fourth-order accurate ($[R_4]C$) truncation forms

$$\begin{aligned}[R_3]C &= A_1 U_x(y)\partial_x\partial_y^2 C + A_2 U_x(y)\partial_x^3 C + B_5 U_x^3(y)\partial_x^3 C, \\ [R_4]C &= A_3\partial_x^4 C + A_4\partial_x^2\partial_y^2 C + A_0\partial_y^4 C + (B_1 + B_2)U_x^2\partial_x^4 C + (B_1 + B_4)U_x^2\partial_x^2\partial_y^2 C + B_6 U_x^4\partial_x^4 C, \\ & A_1 = 2(\Lambda^-)^2 c_e, \quad A_2 = 2(\Lambda^-)^2 c_e - \frac{1}{6}, \quad A_0 = A_3 = -\Lambda^-[(\Lambda^-)^2]c_e^2 + \frac{1}{12}c_e\Lambda^-, \quad A_4 = -2(\Lambda^-)^3 c_e^2, \\ & B_1 = \Lambda^-\bigg[4(\Lambda^-)^2 - \frac{1}{2}\bigg]c_e, \quad B_2 = -\frac{\Lambda^-}{4}, \quad B_4 = 0, \quad B_5 = \frac{1}{6}, \quad B_6 = \frac{\Lambda^-}{4}.\end{aligned} \tag{B5}$$

On the other side, the coefficients (A4)–(A6) become for $\Lambda = \frac{1}{4}$

$$c_{3,1} = 2(\Lambda^-)^2, \quad c_{3,2} = \frac{1}{6}, \quad c_{4,1} = -(\Lambda^-)^3, \quad c_{4,2} = \Lambda^-\bigg[4(\Lambda^-)^2 - \frac{1}{2}\bigg], \quad c_{4,3} = \frac{1}{12}\Lambda^-, \quad c_{4,4} = \frac{\Lambda^-}{4}. \tag{B6}$$

The terms of $c_{3,2}S_d(t_q^{(a)})$ and $c_{4,3}S_d(t_q^{(m)})$ in Eq. (29) vanish in d2Q5 scheme, and Eqs. (29) and (30) read as

$$\begin{aligned}& \Lambda = \frac{1}{4}, t_c^{(\cdot)} = \frac{1}{2}: \\ & A_1 = 2(\Lambda^-)^2 c_e, \quad A_2 = 2(\Lambda^-)^2 c_e - \frac{1}{6}, \quad A_0 = A_3 = -\Lambda^-[(\Lambda^-)^2]c_e^2 + \frac{1}{12}c_e\Lambda^-, \quad A_4 = -2\Lambda^-[(\Lambda^-)^2]c_e^2, \\ & B_1 = \Lambda^-\bigg[4(\Lambda^-)^2 - \frac{1}{2}\bigg]c_e, \quad B_2 = -\frac{\Lambda^-}{4}, \quad B_4 = 0, \quad B_5 = \frac{1}{6}, \quad B_6 = c_{4,4} = \frac{\Lambda^-}{4}.\end{aligned} \tag{B7}$$

This solution coincides with Eq. (B5).

[1] F. J. Pettijohn, P. E. Potter, and R. Siever, *Sand and Sandstone* (Springer, New York, 1972).

[2] U. Scheven and P. N. Sen, Spatial and Temporal Coarse Graining for Dispersion in Randomly Packed Spheres, Phys. Rev. Lett. **89**, 254501 (2002).

[3] U. Scheven, D. Verganelakis, R. Harris, M. Johns, and L. Gladden, Quantitative nuclear magnetic resonance measurements of preasymptotic dispersion in flow through porous media, Phys. Fluids **17**, 117107 (2005).

[4] G. I. Taylor, Dispersion of soluble matter in solvent flowing slowly through a tube, Proc. R. Soc. Lond, Ser. A **219**, 186 (1953).

[5] R. Aris, On the dispersion of a solute in a fluid flowing through a tube, Proc. R. Soc. London, Ser. A **235**, 67 (1956).

[6] E. S. Pearson, Note on tests for normality, Biometrika **22**, 423 (1931).

[7] P. V. Danckwerts, Continuous flow systems, Chem. Eng. Sci. **2**, 1 (1953).

[8] J. Mitchell, A. J. Sederman, E. J. Fordham, M. L. Johns, and L. F. Gladden, A rapid measurement of flow propagators in porous rocks, J. Magn. Reson. **191**, 267 (2008).

[9] H. Brenner, Dispersion resulting from flow through spatially periodic porous media, Philos. Trans. R. Soc., A **297**, 81 (1980).

[10] G. Q. Chen and Z. Wu, Taylor dispersion in a packed tube, Commun. Nonlinear Sci. Numer. Simul. **14**, 2215 (2009).

[11] G. Q. Chen and Z. Wu, Taylor dispersion in a two-zone packed tube, Int. J. Heat Mass Transfer **55**, 43 (2012).

[12] G. Batôt, L. Talon, Y. Peysson, M. Fleury, and D. Bauer, Analytical and numerical investigation of the advective and dispersive transport in Herschel-Bulkley fluids by means of a Lattice-Boltzmann Two-Relaxation-Time scheme, Chem. Eng. Science. **141**, 271 (2016).

[13] J. Salles, J.-F. Thovert, R. Delannay, L. Prevors, J.-L. Auriault, and P. M. Adler, Taylor dispersion in porous media. Determination of the dispersion tensor, Phys. Fluids A **5**, 2348 (1993).

[14] M. Callewaert, W. De Malsche, H. Ottevaere, H. Thienpont, and G. Desmet, Assessment and numerical search for minimal TaylorAris dispersion in micro-machined channels of nearly rectangular cross-section, J. Chromatogr. A **1368**, 70 (2014).

[15] A. Vikhansky and I. Ginzburg, Taylor dispersion in heterogeneous porous media: Extended method of moments, theory, and modeling with two-relaxation-times lattice Boltzmann scheme, Phys. Fluids **26**, 022104 (2014).

[16] K. Bandyopadhyay, A. K. Bhattacharya, P. Biswas, and A. Drabold, Maximum entropy and the problem of moments: A stable algorithm, Phys. Rev. E. **71**, 057701 (2004).

[17] A. Cali, S. Succi, A. Cancelliere, R. Benzi, and M. Gramignani, Diffusion and hydrodynamic dispersion with the lattice Boltzmann method, Phys. Rev. A **45**, 5771 (1992).

[18] E. G. Flekkoy, U. Oxaal, J. Feder, and T. Jossang, Hydrodynamic Dispersion at Stagnation Points: Simulations and Experiments, Phys. Rev. Lett. **77**, 4170 (1995).

[19] D. R. Noble, Lattice Boltzmann Study of the Interstitial Hydrodynamics and Dispersion in Steady State Inertial Flows in Large Randomly Packed Beds, Ph.D. thesis, University of Illinois Urbana-Champaign, 1996.

[20] H. W. Stockman, R. J. Glass, C. Cooper, and H. Rajaram, Accuracy and computational efficiency in 3D dispersion via lattice-Boltzmann: Models for dispersion in rough fractures and double-diffusive fingering, Int. J. Mod. Phys. C **9**, 1545 (1998).

[21] G. Drazer and J. Koplik, Tracer dispersion in two dimensional rough fractures, Phys. Rev. E. **63**, 056104 (2001).

[22] R. Kumar, S. S. Nivarthi, H. Ted. Davis, D. M. Kroll, and R. S. Maier, Application of the LB method to study flow and dispersion in channels with and without expansion and contraction geometry, Int. J. Numer. Methods Fluids **31**, 801 (1999).

[23] J. Yang, J. Crawshaw, and E. S. Boek, Quantitative determination of molecular propagator distributions for solute transport in homogeneous and heterogeneous porous media using lattice Boltzmann simulations, Water Resour. Res. **49**, 8531 (2013).

[24] V. Pot, H. Hammou, N. Elyeznasmi, and I. Ginzburg, Role of soil heterogeneities onto pesticide fate: a pore-scale study with lattice Boltzmann, in *Proceedings of the 1st International Conference and Exploratory Workshop on Soil Architecture and Physicochemical Functions "Cesar"* (Research Centre Foulum, Tjele, 2010).

[25] A. Genty and V. Pot, Numerical calculation of effective diffusion in unsaturated porous media by the TRT lattice Boltzmann method, Transp. Porous Med. **105**, 391 (2014).

[26] L. E. Vogel, D. Makowski, P. Garnier, L. Vieublé-Gonod, Y. Coquet, X. Raynaud, N. Nunan, C. Chenu, R. Falconer, and V. Pot, Modeling the effect of soil meso- and macropores topology on the biodegradation of a soluble carbon substrate, Adv. Water Resour. **83**, 123 (2015).

[27] M. K. Misztal, A. H. Garcia, R. Matin, D. Müter, D. Jha, H. O. Srensen, and J. Mathiesen, Simulating anomalous dispersion in porous media using the unstructured lattice Boltzmann method, Front. Phys., doi:10.3389/fphy.2015.00050 (2015).

[28] I. Ginzburg, Lattice Boltzmann modeling with discontinuous collision components. Hydrodynamic and advection-diffusion equations, J. Stat. Phys. **126**, 157 (2007).

[29] I. Ginzburg and D. d'Humières, Lattice Boltzmann and analytical modeling of flow processes in anisotropic and heterogeneous stratified aquifers, Adv. Water Resour. **30**, 2202 (2007).

[30] H. Yoshida, T. Kobayashi, H. Hayashi, T. Kinjo, H. Washizu, and K. Fukuzawa, Boundary condition at a two-phase interface in the lattice Boltzmann method for the convection-diffusion equation, Phys. Rev. E. **90**, 013303 (2014).

[31] L. Li, R. Mei, and J. F. Klausner, Conjugate heat and mass transfer in the lattice Boltzmann equation method, Phys. Rev. E. **89**, 043308 (2014).

[32] C. Demuth, S. Mishra, M. A. Mendes, S. Ray, and D. Trimis, Application and accuracy issues of lattice Boltzmann method for solving elliptic PDEs commonly encountered in heat transfer and fluid flow problems, Int. J. Thermal Sci. **100**, 185 (2016).

[33] Z. Hu, J. Huang, and W. Yong, Lattice Boltzmann method for convection-diffusion equations with general interfacial conditions, Phys. Rev. E **93**, 043320 (2016).

[34] I. Ginzburg, Equilibrium-type and link-type lattice Boltzmann models for generic advection and anisotropic-dispersion equation, Adv. Water Resour. **28**, 1171 (2005).

[35] I. Ginzburg, Truncation errors, exact and heuristic stability analysis of two-relaxation-times lattice Boltzmann schemes for anisotropic advection-diffusion equation, Commun. Comput. Phys. **11**, 1439 (2012).

[36] R. G. M. Van der Sman, Galilean invariant lattice Boltzmann scheme for natural convection on square and rectangular lattices, Phys. Rev. E. **74**, 026705 (2006).
[37] F. Dubois and P. Lallemand, Towards higher order lattice Boltzmann schemes, J. Stat. Mech. (2009) P06006.
[38] Y. Qian, D. d'Humières, and P. Lallemand, Lattice BGK models for Navier-Stokes equation, Europhys. Lett. **17**, 479 (1992).
[39] Y.-H. Qian and Ye Zhou, Higher-order dynamics in lattice-based models using the Chapman-Enskog method, Phys. Rev. E **61**, 2103 (2000).
[40] Y. Dong, J. Zhang, and G. Yan, A higher-order moment method of the lattice Boltzmann model for the conservation law equation, Appl. Math. Model. **34**, 481 (2010).
[41] I. Ginzburg and L. Roux, Truncation effect on Taylor-Aris dispersion in lattice Boltzmann schemes: accuracy towards stability, J. Comput. Phys. **299**, 974 (2015).
[42] D. d'Humières and I. Ginzburg, Viscosity independent numerical errors for Lattice Boltzmann models: from recurrence equations to "magic" collision numbers, Comput. Math. Appl. **58**, 823 (2009).
[43] I. Ginzburg, D. d'Humières, and A. Kuzmin, Optimal stability of advection-diffusion lattice Boltzmann models with two relaxation times for positive/negative equilibrium, J. Stat. Phys. **139**, 1090 (2010).
[44] A. Kuzmin, I. Ginzburg, and A. A. Mohamad, A role of the kinetic parameter on the stability of two-relaxation-times advection-diffusion lattice Boltzmann scheme, Comput. Math. Appl. **61**, 3417 (2011).
[45] I. Ginzburg, Multiple anisotropic collisions for advection-diffusion lattice Boltzmann schemes, Adv. Water Resour. **51**, 381 (2013).
[46] R. Huang and H. Wu, A modified multiple-relaxation-time lattice Boltzmann model for convection-diffusion equation, J. Comput. Phys. **274**, 50 (2014).
[47] I. Ginzburg, Generic boundary conditions for lattice Boltzmann models and their application to advection and anisotropic-dispersion equations, Adv. Water Resour. **28**, 1196 (2005).
[48] X. Zhang, J. W. Crawford, A. G. Bengough, and I. M. Young, On boundary conditions in the lattice Boltzmann model for advection and anisotropic dispersion equation, Adv. Water Resour. **25**, 601 (2002).
[49] H. Yoshida and M. Nagaoka, Multiple-relaxation-time lattice Boltzmann model for the convection and anisotropic diffusion equation, J. Comput. Phys. **229**, 7774 (2010).
[50] I. Ginzburg, L. Roux, and G. Silva, Local boundary reflections in lattice Boltzmann schemes: spurious boundary layers and their impact on the velocity, diffusion and dispersion, C. R. Mec. **343**, 518 (2015).
[51] I. Ginzburg, Prediction of the moments in advection-diffusion lattice Boltzmann method. II. Attenuation of the boundary layers via double-Λ bounce-back flux scheme, Phys. Rev. E **95**, 013305 (2017).
[52] I. Ginzburg, F. Verhaeghe, and D. d'Humières, Two-relaxation-time Lattice Boltzmann scheme: About parametrization, velocity, pressure and mixed boundary conditions, Commun. Comput. Phys. **3**, 427 (2008).
[53] S. Khirevich, I. Ginzburg, and U. Tallarek, Coarse- and fine-grid numerical behavior of MRT/TRT lattice-Boltzmann schemes in regular and random sphere packings, J. Comput. Phys. **281**, 708 (2014).
[54] I. Ginzburg, G. Silva, and L. Talon, Analysis and improvement of Brinkman lattice Boltzmann schemes: Bulk, boundary, interface. Similarity and distinctness with finite-elements in heterogeneous porous media, Phys. Rev. E. **91**, 023307 (2015).
[55] H. Hammou, I. Ginzburg, and M. Boulerhcha, Two-relaxation-times lattice Boltzmann schemes for solute transport in unsaturated water flow, with a focus on stability, Adv. Water. Resour. **34**, 779 (2011).
[56] G. Silva and V. Semio, Truncation errors and the rotational invariance of the the three-dimensional lattice models in the lattice Boltzmann method, J. Comput. Phys. **269**, 259 (2014).
[57] Y. Kuwata and K. Suga, Anomaly of the lattice Boltzmann methods in three-dimensional cylindrical flows, J. Comput. Phys. **280**, 563 (2015).
[58] Y. K. Kwok and K. K. Tam Stability analysis of three-level difference schemes for initial-boundary problems for multidimensional convective-diffusion equations, Commun. Numer. Methods Eng. **9**, 595 (1993).
[59] E. C. Du Fort and S. P. Frankel, Stability conditions in the numerical treatment of parabolic differential equations, Math. Tables and Other Aids to Computation **7**, 135 (1953).
[60] M. G. Ancona, Fully-Lagrangian and Lattice-Boltzmann Methods for solving systems of conservation equations, J. Comput. Phys. **115**, 107 (1994).
[61] S. Suga, An accurate multilevel finite difference scheme for 1D diffusion equation derived from the lattice Boltzmann method, J. Stat. Phys. **140**, 494 (2010).
[62] S. Dellascherie, Construction and analysis of lattice Boltzmann methods applied to a 1D convection-diffusion equation, Acta Appl. Math. **131**, 69 (2014).
[63] A. C. Hindmarsch, P. M. Grescho, and D. F. Griffiths, The stability of explicit time-integration for certain finite difference approximation of the multi-dimensional advection-diffusion equation, Int. J. Numer. Methods Fluids **4**, 853 (1984).
[64] Z. Chai, C. Huang, B. Shi, and Z. Guo, A comparative study on the lattice Boltzmann models for predicting effective diffusivity of porous media, Int. J. Heat Mass Transfer. **98**, 687 (2016).
[65] S. Cui, N. Hong, B. Shi, and Z. Chai, Discrete effect on the halfway bounce-back boundary condition of multiple-relaxation-time lattice Boltzmann model for convection-diffusion equations, Phys. Rev. E **93**, 043311 (2016).